Fall 11-26-2012

J Psi Measurement in Au+Au Collisions at sqrt (sNN) = 39 and 62.4 GeV

Abhisek Sen
Georgia State University

J/ψ MEASUREMENT IN AU+AU COLLISIONS AT $\sqrt{s_{NN}} = 39$ AND 62.4 GEV

by

ABHISEK SEN

Under the Direction of Prof. Xiaochun He

ABSTRACT

J/ψ production is considered a very important probes for studying the properties of quark gluon plasma (QGP). At the PHENIX experiment at Brookhaven National Laboratory, a large suppression of J/ψ production in Au+Au collisions at 200 GeV center of mass energy as compared to the binary collision scaled p+p collisions was observed. The level of suppression is similar to that observed at other energies at CERN's SPS and LHC experiments. This work addresses the PHENIX J/ψ measurements at $\sqrt{s_{NN}} = 39$ and 62.4 GeV Au+Au collisions. These allow for the energy dependent J/ψ suppression measurements in order to disentangle the important contributing factors of J/ψ production. J/ψ results over a wide range of center of mass energies (39-200 GeV) from PHENIX are discussed, in addition to a comprehensive comparison with other experiments.

INDEX WORDS: Quark gluon plasma, J/ψ, Heavy ion, Au+Au

J/ψ MEASUREMENT IN AU+AU COLLISIONS AT $\sqrt{s_{NN}} = 39$ AND 62.4 GEV

by

ABHISEK SEN

A Dissertation Submitted in Partial Fulfillment of the Requirements for the Degree of

Doctor of Philosophy

in the College of Arts and Sciences

Georgia State University

2012

J/ψ MEASUREMENT IN AU+AU COLLISIONS AT $\sqrt{s_{NN}} = 39$ AND 62.4 GEV

by

ABHISEK SEN

Committee Chair:	Dr. Xiaochun He
Committee:	Dr. Murad Sarsour
	Dr. Steven T. Manson
	Dr. Misty Bentz

Electronic Version Approved:

Office of Graduate Studies

College of Arts and Sciences

Georgia State University

December 2012

DEDICATION

To my dad.

His guidance, support and inspiration are the foundation of my accomplishment.

ACKNOWLEDGEMENTS

Writing of this dissertation has been one the most significant academic challenges I ever faced. Without the support, patience and guidance from the following people the work would not have been completed. So, I would like to take the opportunity to thank all those who made this possible.

First of all, I am indebted to my advisor Prof. Xiaochun He, an exceptional mentor. Working with you was filled with fun and excitement. You have oriented and supported me with promptness and care, and have always been patient and encouraging in times of new ideas and difficulties. You always backed me when I needed, even helped me in my very earlier days in US which made me feel a friend, which I appreciate from my heart.

Thanks to Laura Patel, for being my lab-mate, english mentor and a very good friend when I needed one. You kept the lab environment fun-filled, pleasant and productive.

Furthermore, I like to thank the whole GSU group and I had pleasure working with you. Special thanks to Dr. Murad Sarsour, Dr. Jun Ying, Dr. Liang Xue, Carola Butler, Kanishka Dayananda, Christopher Oakley, Xiaohong Zhang, David Camp, Maggie Jezghani, Matthew Haddad and Hari Guragain. Thanks for your support and encouragement.

In addition, as a part of PHENIX collaboration, I have been privileged to get to know and collaborate with great many people in the last several years. This work would not have been possible without help from Jamie Nagle, Mike Leitch, Hugo Pereira, Cesar Da Silva, Matthew Wysocki, Tony Frawley and Marzia Rosati. Thanks for the encouraging discussions and teaching me a great deal of physics as well as technical groundwork.

Finally, I would like to thank my family for all their support and encouraging my education. My mom, dad, younger brother and my cousins, I would not be where I am without all of you.

TABLE OF CONTENTS

LIST OF TABLES

LIST OF FIGURES

LIST OF ABBREVIATIONS

- BNL - Brookhaven National Laboratory

- RHIC - Relativistic Heavy Ion Collider

- PHENIX - Pioneering High Energy Nuclear Interaction eXperiment

- STAR - Solenoidal Tracker at RHIC

- QGP - Quark Gluon Plasma

- CNM - Cold Nuclear Matter

- HNM - Hot Nuclear Matter

- CERN - European Organization for Nuclear Research

- LHC - Large Hadron Collider

- CMS - Compact Muon Solenoid

- ALICE - A Large Ion Collider Experiment

- FNAL - Fermi National Accelerator Laboratory

- MB - Minimum Bias

- GSU - Georgia State University

CHAPTER 1

INTRODUCTION

The Relativistic Heavy Ion Collider (RHIC) is located at the Brookhaven National Laboratory (BNL) on Long Island near New York city, USA. The main goal for the experimental programs at RHIC is to study matter in extreme conditions and understand the properties of the Quark Gluon Plasma (QGP), a deconfined state of nuclear matter at very high temperature and high baryon density [1]. It is thought that the universe was created from a "Big Bang" and was initially in a QGP state (just after the creation) [2]. Then the universe expanded and the energy density decreased which lead to the transition to ordinary (confined) matter. In experiments performed at BNL, RHIC collides different particle species traveling at very close to the speed of light. In 2005, four experiments at RHIC jointly published articles summarizing the key measurements at RHIC and announcing the discovery of a state of matter similar to QGP produced at heavy ion collisions [1]. Such a medium, where the relevant degrees of freedom over nuclear volumes, are expected to be those of quarks and gluons and the predictions of Quantum Chromodynamics (QCD), a fundamental theory which describes the role of quarks and gluons in nuclear matter, can be explored. Results indicate that the matter created at RHIC reflects properties of a perfect fluid, analogous to a strongly coupled plasma state, sometimes referred as *strongly coupled quark gluon plasma*, or sQGP.

1.1 Standard Model

The primary objective for nuclear and particle physics research is to study the fundamental forces and their symmetries and to be able to understand elementary particles in nature. Matter has a hierarchy of constituents: macroscopic matter consists of molecules and atoms, the atoms consist of a nucleus and electrons. The nucleus is made of protons

Figure 1.1: Quark and lepton family, the fundamental constituents of matter in Standard Model. Masses are taken from Particle Data Book [3].

and neutrons (together they are called nucleons) which are composed by quarks, anti-quarks and gluons (called partons).

Throughout history, physicists have been working with scattering experiments at higher and higher energies to achieve information on smaller and smaller scales. Scattering efficiency and behavior depends on the size of the scatters relative to the wavelength of radiation (x $\sim \lambda \sim 1/E$). Quarks and leptons are considered the two basic type of fundamental elementary particles. At the moment the hierarchy ends at quarks and leptons, no substructure has been observed. They are considered as point like particles. According to modern Standard Model, there are 6 quarks, up, down, charm, strange, top and bottom and 6 leptons, electron, muon, tau and their corresponding neutrinos (shown in Fig. 1.1).

There are four fundamental forces: the gravity, the weak force, the electromagnetic force and the strong force. Each of these forces are carried by different force carriers called bosons as shown in Table. 1.1. They are responsible for all interactions between them. The Photon is the carrier for the Electromagnetic force, the Gluon is for the Strong Force, the W and the Z bosons are for the Weak Force. The theory which describes all fundamental particles and interaction between them is called Standard Model.
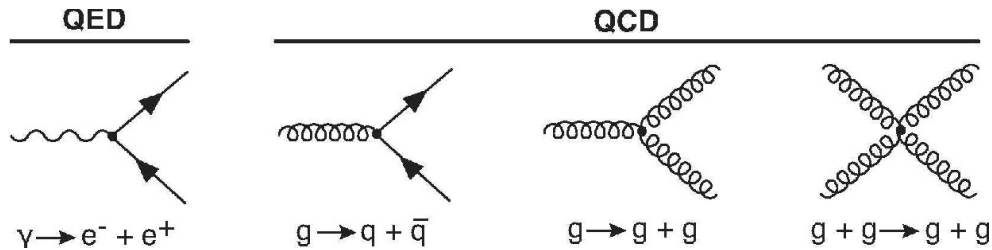
Figure 1.2: Feynman diagrams for QED and QCD vertices's.

Table 1.1: Forces and their strengths relative to strong force [3].

Name	Relative strength	Range	Exchange particle
gravity	10^{-38}	∞	graviton
weak	10^{-13}	$< 10^{-18}m$	Z^0, W^+, W^-
electromagnetic	10^{-2}	∞	photon
strong	1	∞	gluon

The branch of the standard model that deals with electro-magnetic and weak interactions are called Quantum Electrodynamics (QED) and the calculations are very accurate. These interactions are typically perturbative calculations that expand in powers of $\alpha_{EM} \sim 1/137$. Strong interactions between quarks and gluons are better described by Quantum Chromodynamics (QCD), "chromo" for additional quark color quantum numbers. Fig. 1.2 shows few Feynman diagrams for QED and QCD processes. According to the Standard Model quarks have six flavors. Each quark flavor has a corresponding type of antiparticle called the anti-quark, with same the magnitude but opposite charge. There are three types of "color" charge, arbitrarily labeled as red, green and blue and their corresponding anti-colors are anti-red, anti-green and anti-blue. The quark carries a color while the anti-quark carries an anti-color. Gluons, the strong force carriers can have two colors and known as color octet. This encode the fact that when a gluon interacts with a quark and rotates the quark's color in SU(3) space. Where SU(3) is the gauge symmetry in QCD

corresponds to the color charges.

Unlike leptons, quarks have not been observed as independent particles. Only a combination of quarks and anti-quarks "confined" into color-neutral hadrons can exist. There are two types of hadrons, masons and baryons. Mesons (π, K, ρ, η) carry a quark and an anti-quark $(q\bar{q})$, where baryons (p, Λ, Ω, n) consist of three quarks, qqq(or $\bar{q}\bar{q}\bar{q}$). All hadrons found experimentally are color neutral. So when three quarks form a baryon, they must combine in colorless combination red-green-blue, irrespective of quark flavors. Quarks have baryon number B=1/3 and anti-quarks have baryon number B=-1/3. Hence baryons will have baryon number B= $\pm$1 and mesons have B= 0. Though it was proposed that baryons can have more than three quarks, called "exotic baryons", such as pentaquarks formed by 4 quarks and 1 anti-quark but they were never observed.

In QCD framework quarks interacts with themselves through mass-less gauge fields, gluons. There are eight types of spin-1 gluon which can interact with quarks as well as with other gluons, shown in the basic Feynman diagram in Fig. 1.2. These interactions between two quarks (q and $\bar{q}$) can be describe with the potential energy,

$$V(r) = Kr - \frac{\alpha_s}{r} \tag{1.1}$$

Where r is distance between q and $\bar{q}$. At small distances quarks behaves just like electrons with a coulumbic potential α_s/r but at large distances this interaction becomes much stronger since gluons can interact with themselves. At sufficiently high separation the potential energy increases and it eventually becomes energetically favorable for the original pair to splits into two quark anti-quark pairs. α_s in the above equation is the coupling constant, also known as the running coupling constant. To be precise, this coupling is not actually a constant term; it changes with the four momentum transfer (Q^2) and can be written as,

$$\alpha_s \approx \frac{12\pi}{(33 - 2N_f)ln(Q^2/\Lambda_{QCD}{}^2)} \tag{1.2}$$

where N_f is the number of accessible quark flavors which can't be larger than six and

Figure 1.3: Running coupling constant as a function of Q [4]

Λ_{QCD} is a constant QCD scale parameter, which needs to be determined experimentally ($\Lambda_{QCD} \approx 250 MeV/c$). As shown in Fig. 1.3 the effective coupling between quarks is infinitely strong at low Q, exhibiting confinement phenomena. The coupling constant decreases with increasing Q. At large Q or short separation, the effective coupling constant becomes so small that partons can move freely and their interactions may be calculated with perturbation theory. This phenomena, called "asymptotic freedom", was discovered by Wilczek,Politzer and Gross in 1973 who won Nobel Prize in 2004 because of this discovery [5, 6]. So in normal conditions quarks and gluons are confined into hadrons but at higher temperature and density a new state of matter Quark Gluon Plasma (QGP) can exists which is composed of deconfined quarks and gluons. Lattice QCD is one of the theories that describes the interaction between quarks and gluons in non-perturbative regime [7]. Lattice QCD calculations show that there is a phase transition from hadronic matter, where quarks and gluons are confined into hadrons, to QGP at an extremely high temperature $T_C \sim 170 MeV$ and high energy density $\epsilon_C \sim 1 \; GeV/fm^3$ [8, 9].

1.2 QCD Phase Space

The behavior of QCD at extreme high temperatures and densities has long been of interest. According to the standard model of cosmology, our universe originated in a "Big Bang" from a state of almost infinite energy and temperature [10]. At this initial state of the universe, quarks, antiquarks and gluons were deconfined and occupied the whole universe in a thermalized state of QGP. As time passed and the energy density dropped below the critical limit $\epsilon_C \sim 1 GeV/fm^3$ and the temperature dropped below $T_C \sim 170$ MeV, a phase transition occurred between the QGP and normal matter, where colored degrees of freedom became confined and hadrons were formed. A schematic phase diagram of hadronic matter including QGP is shown in Fig. 1.4, shows the normal nuclear matter, hadronic gas and the QGP phase. The horizontal axis is the baryon density normalized to the density of normal nuclear matter ($\sim 0.15 \; GeV/fm^3$) and the vertical axis is the temperature. However, direct evidence of the QGP phase from the "Big Bang" is hidden behind the last scattering
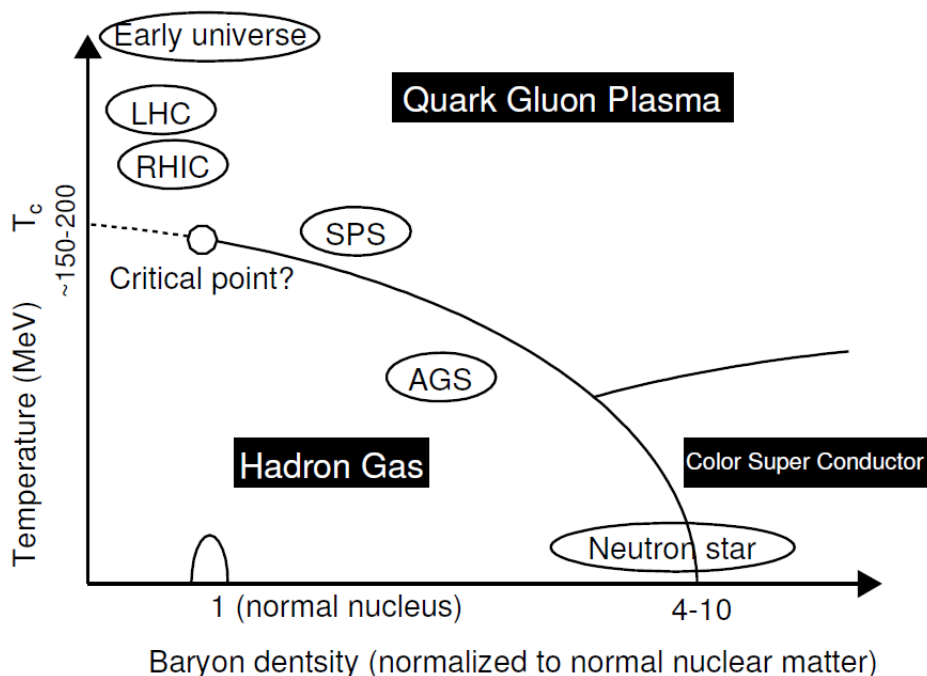
Figure 1.4: QCD phase diagram

surface of the cosmic microwave background which came at later stage of universe's early history [11]. So a direct study of QGP from astronomical observations of the early universe is not possible. There have been some predictions that radio-quiet neutron stars, a new type of "quark" star might also allow for astronomical observations of the deconfined phase of matter [12]. However at this time, heavy nuclei collisions at high energy laboratories can provide the only opportunity to carry out the studies of the nature of quark gluon plasma,

The QCD phase diagram is very similar to the phase space of water. In the phase space diagram of water there are three possible states: water, ice and vapor. The point at very high temperature and pressure, where the liquid and gaseous phases become indistinguishable is called the critical point. The critical point for water is 647K (374° C) at pressure $600Nm^{-2}$. For $T < T_c$ the transition between liquid and vapor is first order, implying discontinuities in entropy and volume and beyond that its second order having discontinuities in specific heat and isothermal compressibility. Similarly in the proposed phase diagram of QCD, the control

parameters are T and baryon density. In the bottom left-hand corner of the phase diagram where temperature and baryon density are both small, the thermodynamic behaviors of QCD can be described in terms of a vapor of hadrons, which are composite states of quarks and anti-quarks. Eventually there comes a point where either a transition or a crossover occurs to a phase where the dominant degrees of freedom are no longer hadrons but quarks themselves together with gluons in a state of Quark Gluon Plasma. Different phases have different symmetries of their own and are separated by critical lines.

Unfortunately, the transition near QGP is in an inherently non-perturbative regime and it is not easy to perform calculations. Lattice QCD, which makes use of Euclidean space-time grid to calculate the path integral of the QCD partition function, is used to perform numerical calculations. Experimentally it is hard to map the whole phase diagram because of the difficulties in tuning the temperature and the density in the laboratory. However, the phase transition between confined and deconfined phases of QCD is being studied extensively in heavy ion collisions experiments and in lattice QCD. It has been confirmed that the QGP undoubtedly exists at sufficiently high energies produced in heavy ion collisions. In lattice QCD calculations, a purely gluonic (SU(3) gauge symmetric) system, for which the Equation of State (EoS) has been computed without approximations, the deconfinement phase transition is found to be of the first order and the critical temperature is $T_C \approx 170 MeV$ [8, 9]. Once QGP is formed, it must quickly expand and cool down due to fast expansion and as temperature T falls below T_c, hadrons started forming, this called chemical freeze-out.

1.3 Heavy Ion Collision

The Relativistic Heavy Ion Collider (RHIC) is able to recreate Quark Gluon Plasma state by colliding heavy ions moving at very close to the speed of light. Heavy ion collisions are schematically shown in Fig. 1.5, where two nuclei collide with impact parameter b. As seen in the figure, due to their relativistic speed, the colliding nuclei are Lorentz contracted and look like thin pancakes. Nucleons which are in the overlap region on the transverse

plane participate in the collision and called "participants". Other nucleons, which do not participate in the collision are called "spectators". Participants deposit a large amount of energy in a very small region creating a hot and dense state of matter of high energy density. The energy density is proportional to the number of participants. For small impact parameter $b \sim 0$, almost all the nucleons participate in the collision and, is called a "central collision". On the other hand, at larger impact parameters, only a few nucleons collide and those collisions are called "peripheral collisions".

In proton-proton collisions, after such collisions, the produced quarks and gluons fly away practically free, dress with a gluon cloud and rapidly form color singlet bound states, hadrons. But in a heavy ion environment the situation radically changes. When many partons are scattered simultaneously into the same volume element and a hot-dense medium of partons is formed, where the interactions of quarks, antiquarks and gluons are so effectively screened that the formation of bound states is inhibited and QGP is formed. As the medium expands and cools down, it passes through different phases, as shown in Fig. 1.6. Hadronization is the phase, when the temperature becomes low enough for free partons to become confined into hadrons. Next, kinetic freeze-out occurs when the expanding hadrons are too sparse to interact with one another. At this point they will continue along their trajectories and can be experimentally observed. It is important to mention that in order to understand any QGP medium properties through the nature of the particle production the evolution through other phases must be accounted for as well. Hadronization in particular is not understood well.

It is challenging to study the properties of the medium experimentally due to its exceedingly short lifetime. Over the past 25 years of heavy ion collision history, many experimental probes have been suggested to study the properties of QGP states. One interesting way to probe QGP experimentally is through heavy **quarkonium($q\bar{q}$) suppression** in heavy ion collisions. Heavy quarks (HQ), charm and bottom quarks are produced through hard scattering in the very early stage of the collisions in the medium. Their bound states are called charmonium($c\bar{c}$) and bottomonium ($b\bar{b}$). Due to their heaviness, they are least ef-
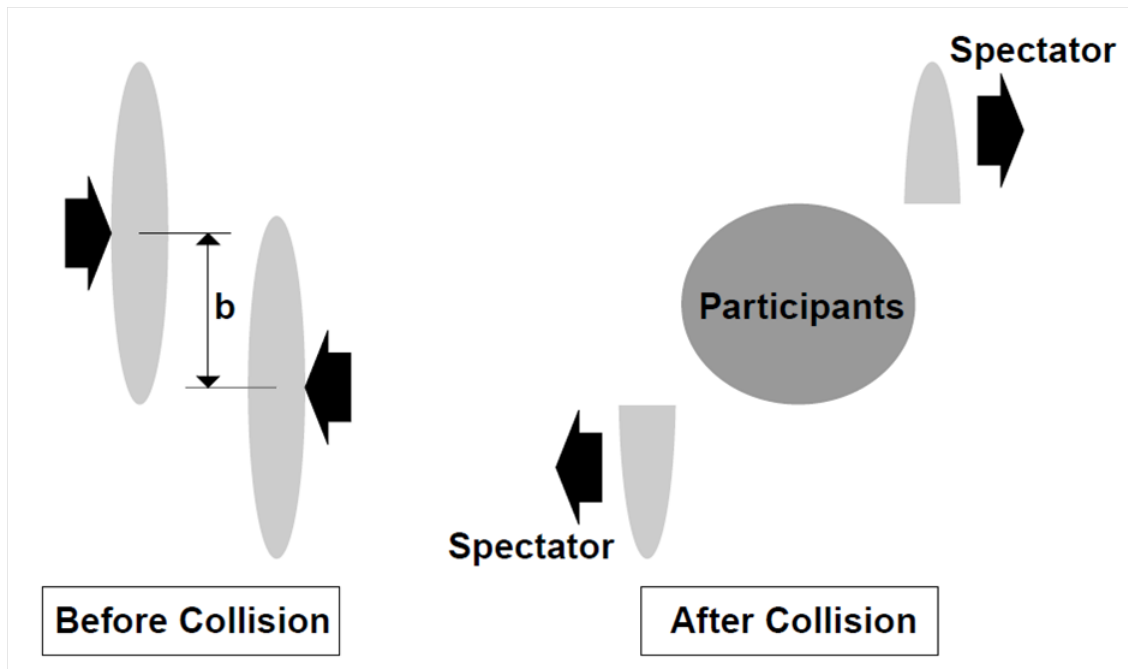
Figure 1.5: The view of the colliding nuclei before and after the collisions. Two nuclei with impact parameter b were bring into collision at almost the speed of light. System divides into components after the collision, the spectator and participants.
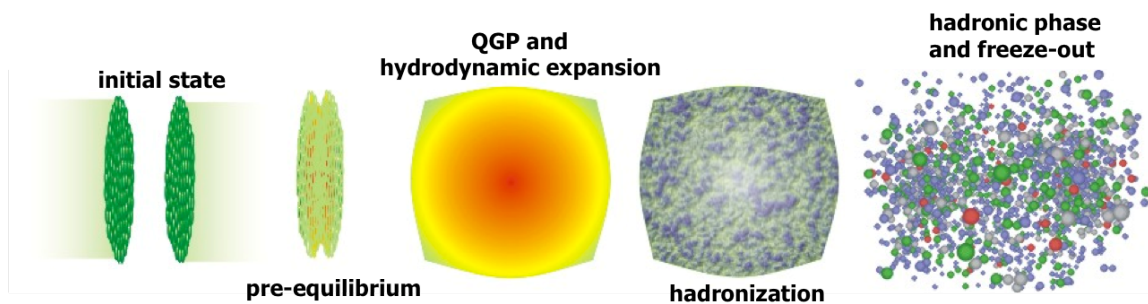
Figure 1.6: Stages of heavy ion collisions at RHIC.

fected by the final state interactions like hadronization. If a hot-dense medium like QGP is formed, Quarkonia bound states will dissolve or never form in the medium due to color screening. This probe was first proposed by Matsui and Satz in 1986 [13]. The presence of QGP will prevent production of $q\bar{q}$ pairs and lead to a suppression. This quarkonia bound state suppression phenomena can be tested experimentally in order to quantify the medium properties. Furthermore, this feature behaves like a thermometer of the medium, as the dissociation temperature will be different for different quarkonium states depending on their binding energies. For my thesis I will be focusing on J/ψ (a charmonium, $c\bar{c}(1S)$ bound state) analysis at various center of mass energies, to explore the QGP signature by analyzing the energy dependence of J/ψ suppression at Au+Au collisions at RHIC.

CHAPTER 2

J/ψ MESONS

For many years studying J/ψ has been a very interesting topic in both experimental and theoretical particle physics. The reason is that J/ψ carries important signatures of the initial state medium properties which created in heavy ion collisions. The J/ψ discovered in 1974, is the first charmonium (made of one charm and another anti-charm quark), has a rest mass of 3096.87 ± 0.04 MeV/c^2 and a mean lifetime of 7.2×10^{-21} s [3]. It was discovered by two independent research groups simultaneously. SLAC (Stanford Linear Accelerator Center) and BNL both announced the discovery of this particle simultaneously on the date of 11th November 1974 [14, 15]. Burton Richter from SLAC and Samuel Ting from BNL were awarded Nobel prize in physics in 1976 for this discovery. It primarily decays into hadrons, branching ratio B($J/\psi \rightarrow$hadrons)=87.7±0.5% but it also decay through the lepton channels to e^-e^+ (B($J/\psi \rightarrow e^-e^+$)=5.94±0.06%) and $\mu^-\mu^+$ (B($J/\psi \rightarrow \mu^-\mu^+$)=5.93±0.06%), which experimentalists use to study J/ψ [3]. Since its discovery, many more charmonium states have been discovered: ψ', η_C and χ_C etc. Several charmonia states are shown in Fig. 2.1, with their major decay modes between the those charmonia states.

2.1 J/ψ Production

This section briefly describes the J/ψ production mechanisms. The production of heavy quarkonia is expected to be perturbative, since charm quarks are heavy compared to the typical QCD scale $\Lambda_{QCD} \sim 0.2$ GeV, which corresponds to $\alpha_s(c) << 1$. Fig. 2.2 shows different heavy quark production diagrams, where (a)-(c) are leading order processes and (d)-(f) are higher order processes. The dominant source of J/ψ production at RHIC energies is gluon fusion (a) of Fig. 2.2), which takes place at very short time $\tau_{pert} \approx 1/2 * m_C$.

A number of theoretical approaches have been proposed for the calculations of heavy-
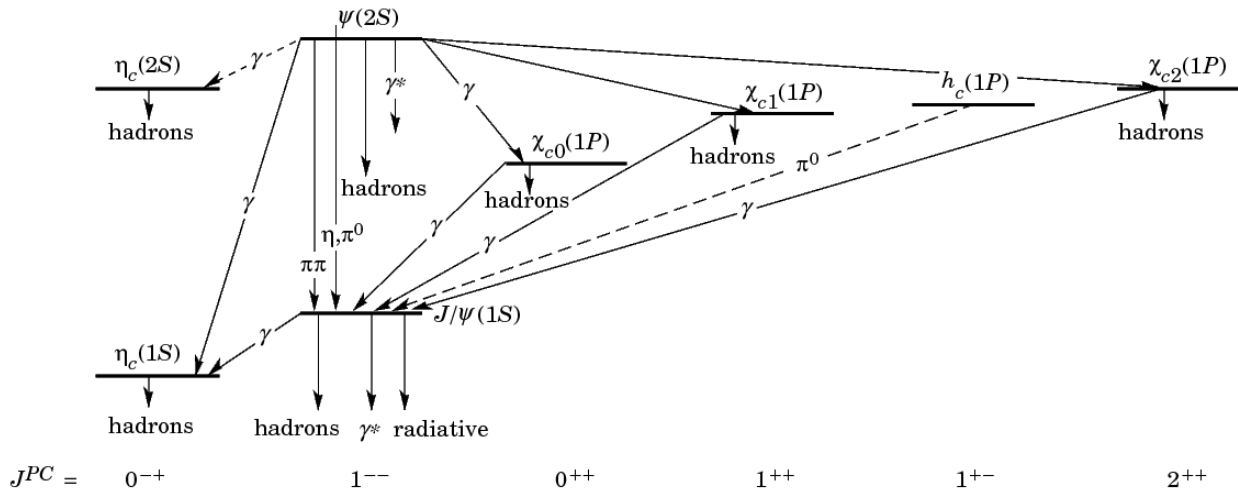
Figure 2.1: Charmonia states and their decay modes [16].
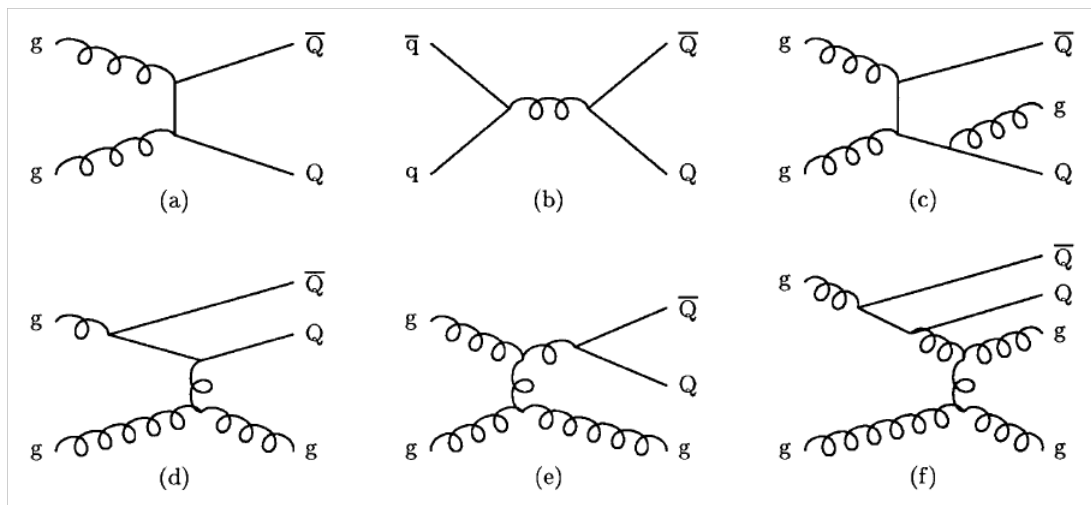
Figure 2.2: Heavy flavor production diagrams: (a) Gluon fusion (leading order) (b) Quark-antiquark annihilation (leading order) (c) Pair creation with gluon emission (d) Flavor excitation (e) Gluon splitting (f) Together gluon splitting and flavor excitation [17].

quarkonium production to explain the experimental results. These include the Non-relativistic QCD (NRQCD) factorization approach, the color-singlet model (CSM) and the color-evaporation model (CEM) etc.

Non-relativistic QCD (NRQCD)

NRQCD is an effective field theory that describes the behavior of bound states of a heavy-quark (Q) and a heavy-antiquark($\bar{Q}$). The model is non-relativistic because the velocity v of Q and $\bar{Q}$ in the $Q\bar{Q}$ rest frame is non-relativistic ($v << c$) [18]. One might think that the large mass of the charm quarks as the reason to neglect relativistic effect and quarkonia production can be calculated accurately by perturbative theory. However, low momentum and nonperturbative nature associated with the dynamics of the quarkonium production make it questionable. NRQCD carries out the perturbative process, with which one can factorize the production cross section of the $c\bar{c}$ pairs as a powers of α_s.

Color-singlet model (CSM)

In CSM, a $Q\bar{Q}$ pair is in a color-singlet bound state, where Q and $\bar{Q}$ are separated by distance $\sim 1/m_Q v$ which is smaller than Λ_{QCD}. CSM postulates that the formation of a meson out of two heavy quarks can be factorized. It also assumes that the color and spin of the $q\bar{q}$ pair do not change during binding and therefore the $q\bar{q}$ pairs are required to be produced in color singlet states. The model describes the J/ψ photo-production very well but fails to describe the Tevatron data in $p + \bar{p}$ collisions at $\sqrt{s}$ =1.8 TeV by a factor of ~ 60 [19, 20]. Recently, it has been found that very large corrections to the CSM appear at next-to-leading order (NLO) and next-to-next-leading order (NNLO) in α_s [21]. Given the large corrections at NLO and NNLO, it is not clear that the perturbative expansions in α_s are convergent.

Color-evaporation model (CEM)

CEM is able to reproduce a number of experimental results very well. The model assumes that the color state of the produced $c\bar{c}$ is completely random and there is one out of nine chances of ending up with colorless (singlet state) meson. In other cases they are
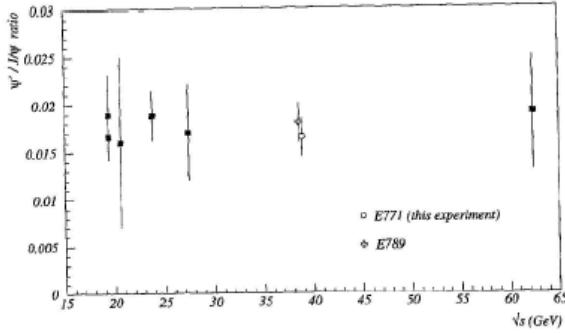
Figure 2.3: The feed-down from ψ' as a function of center of mass energies [24].
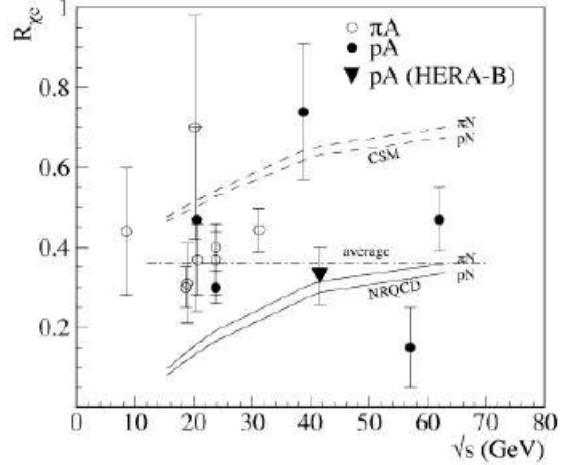
Figure 2.4: The feed-down from χ_C decay to J/ψ as a function of $\sqrt{s}$, alongwith prediction from NRQCD and CSM models [25].

assumed to end up in open charm (or D) mesons, where one charm quark paired with another quark of lesser mass. This can be written as

$$\sigma(J/\psi) = \frac{\rho}{9} \int_{2m_C}^{2m_D} dm \frac{d\sigma_{c\bar{c}}}{dm} \tag{2.1}$$

where $\frac{d\sigma_{c\bar{c}}}{dm}$ is the differential $c\bar{c}$ production cross-section with respect to mass m. m_C and m_D are the masses of open charm and D mesons. The natural value of ρ is the inverse of the number of quarkonia states between $2m_C$ and $2m_D$, basically determined from experimental results. CEM has the restriction on the mass of $c\bar{c}$ pairs, which should be below the mass of $D\bar{D}$. The reason it is called "color evaporation" model is because $c\bar{c}$ pairs are assumed to neutralize its color by interacting with collision gluon field [22, 23].

Feed-down

Feed-down effects are an important feature to be noted in J/ψ production. Total J/ψ production can be divided into total four categories: (a) Directly produced J/ψ ($\sim 60\%$), (b)
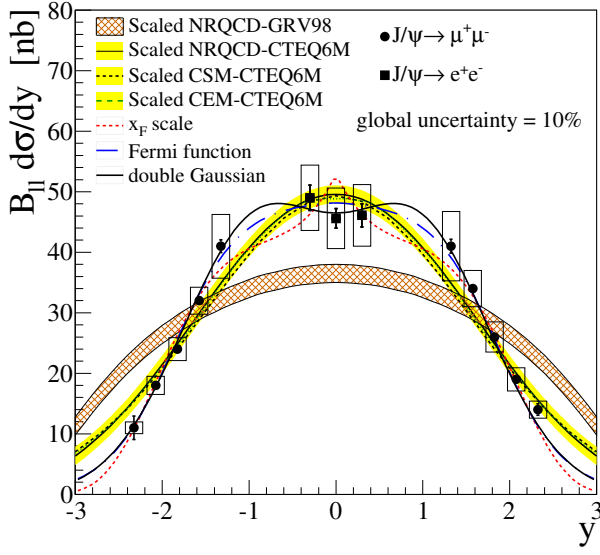
Figure 2.5: Rapidity distribution of J/ψ production at 200 GeV $p+p$ collisions [26].
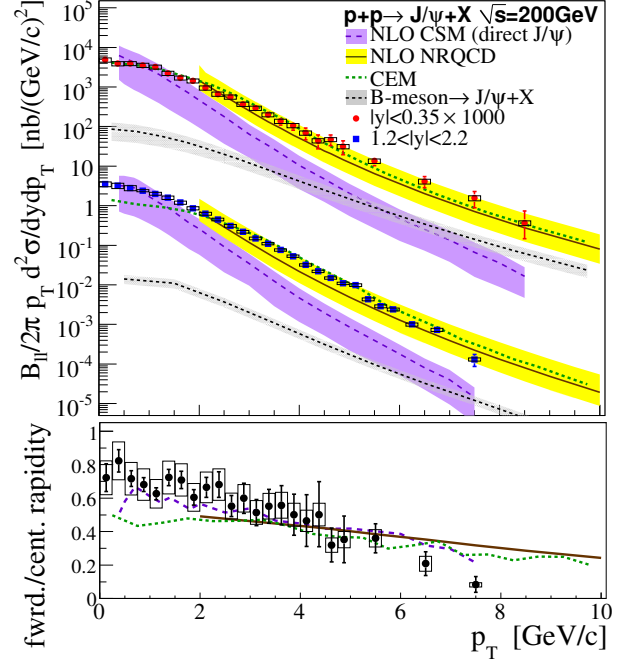
Figure 2.6: Pt distribution of J/ψ production at 200 GeV $p + p$ collision [26].

J/ψ produced from decay of three χ_C states ($\sim 30 - 40\%$), (c) J/ψ produced from ψ' decay ($\sim 5 - 10\%$), and (d) J/ψ produced from open bottom decay ($\sim 6\%$). Fig. 2.4 show the ratio of χ_C production cross section which decayed to J/ψ to the production cross sections of inclusive J/ψ as a function of collision energy. The world average is around $\sim 35\%$ [25]. Fig. 2.3 is the ratio $B(\psi' \to \mu^+\mu^-)\sigma(\psi')/B(J/\psi \to \mu^+\mu^-)\sigma(J/\psi)$, with an average of $\sim 1.6\%$. This corresponds to a feed-down $B(\psi' \to J/\psi)\sigma(\psi')/\sigma(J/\psi)) \sim 6\%$ [24].

PHENIX has measured J/ψ production at $\sqrt{s} =$200 GeV p+p collisions, in a very wide range of acceptance in rapidity and p_T [27, 26]. Where rapidity (y) and p_T are kinematic variables as defined in Appendix. A. Fig. 2.5 and Fig. 2.6 show the J/ψ production in a very wide range of rapidity and p_T, compared to predictions from CSM, NRQCD and CEM models. It is worthwhile to mention that there has been a lot of work done towards understanding J/ψ production, but there is still a way to go before there is a complete understanding of the complicated $p + p$ (or $p + \bar{p}$) environments. In the next section, we

will review the J/ψ properties in heavy ion collisions as compare of a $p + p$ system. A clear understanding of $p+p$ environment is required before quantifying the heavy ion collisions.

2.2 J/ψ Production in Heavy Ion Collisions

Since the mass of the charm quarks is heavy, the creation of the charm quark pairs takes place at the very early in the collision. Then J/ψ were formed from those pre-resonance $c\bar{c}$ pairs at a very short time and it is thought that J/ψ may be formed before the formation of QGP [28]. After creation, J/ψ or the pre-resonance of $c\bar{c}$ pairs evolve with the evolution of the hot dense medium created in heavy ion collisions. Thus the produced J/ψ's contain signatures which are sensitive to the initial conditions inside the colliding nuclei. Due to their heaviness they are barely affected through hadronization as well.

Medium effects on J/ψ production in heavy-ion collisions can be categorized into two groups. One is the effects on the J/ψ production after the formation of QGP, called "final state effects". The other is the effects before the formation of QGP, called the "cold nuclear matter effects (CNM)" or "initial state effects". As the cold nuclear matter effects, following effects can contribute towards the J/ψ production:

- Modification of gluon distribution function in heavy nuclei.

- Interaction of pre-resonance $c\bar{c}$ state or J/ψ with the participant nucleons (a.k.a nuclear absorption).

- Multiple interactions of partons inside nuclei (Cronin effect).

Final state effects including the following mechanisms those are responsible for modification of J/ψ production in heavy ion collisions:

- Color screening and dissociation of $c\bar{c}$ pairs.

- Re-combinations of J/ψ from uncorrelated $c\bar{c}$ pairs.

- Interaction of J/ψ with secondary co-moving particles.

2.3 Cold Nuclear Matter Effects

In addition to the effect of QGP (sometimes called as hot matter effects and discussed in next section), the explanation of J/ψ suppression has gotten more complex in the last 15 years, due to the suppression of J/ψ within normal nuclear matter (called cold nuclear matter effects), which was missing from the prediction of Matsui and Satz [13].

Gluon shadowing

The quark and anti-quark distributions as a function of momentum fraction (i.e. fraction of total momentum carried by a parton, x) and momentum transfer Q^2 have been probed through the deep inelastic scattering (DIS) of leptons and neutrinos from nuclei.

$$x = \frac{m_T}{\sqrt{s}} e^y \tag{2.2}$$

where $m_T = \sqrt{p_T^2 + m^2}$ is the transverse mass of J/ψ. The European Muon Collaboration (EMC) experiment shows that the nuclear Parton Distribution Functions (nPDF) deviate from those of free nucleons [29]. Nucleons shadow each other modifying the nPDFs relative to those of the free nucleons, a phenomenon called "shadowing", which depends on the momentum fraction x and square of the momentum transfer Q^2. At $0.01 \leq x \leq 0.3$, some experiments found an enhancement of partons compared to free nucleons, called "anti-shadowing", shown in Fig. 2.7. The nuclear-modified PDF reflects the modification of parton density which results in a modified number of the hard scatterings that create $c\bar{c}$ pairs from $g + g$, $q + g$ and $q + \bar{q}$ interactions. At RHIC energies the J/ψ production is dominated by $g + g$ interactions and gluon distributions will be modified as shown in Fig. 2.7, which will result in J/ψ modification as well. It can be seen that the nPDFs are not well constrained, particularly at the low x region of gluon distribution which dominates at RHIC forward energies. EPS09, EKS98 and nDS are different parametrizations, which are very model dependent at present [30, 31]. Experimental measurements are needed to reduce these uncertainties. This modified nuclear PDF (nPDF) distributions can significantly contribute to
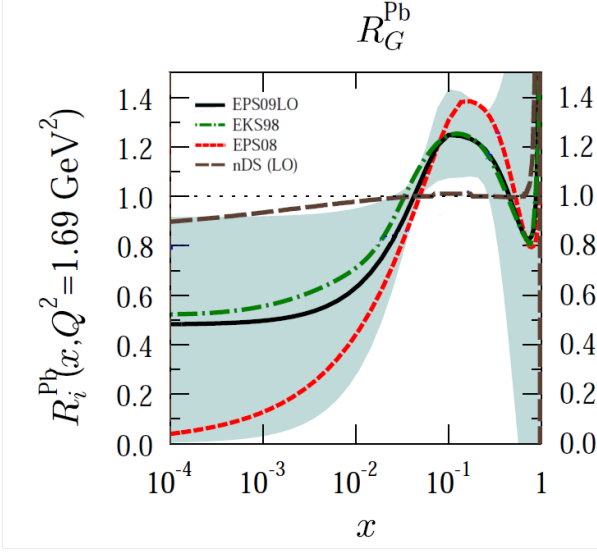
Figure 2.7: Gluon nPDF modifications in Au nuclei (A=208) compared to $p+p$ [31].
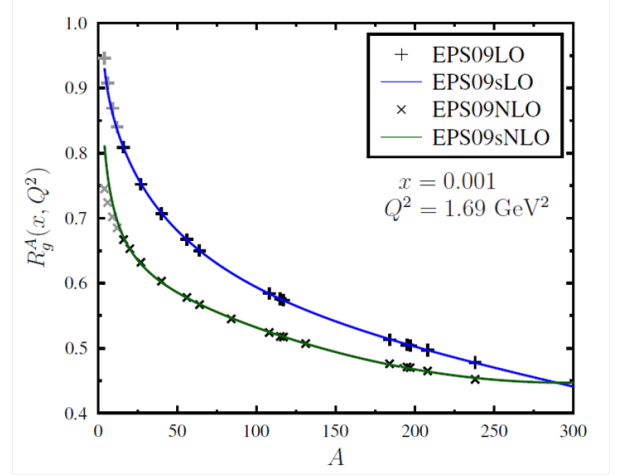
Figure 2.8: The spatially averaged gluon modification at a fixed value of x and Q^2 for EPS09 LO and NLO models [31].

the J/ψ suppression, depending on the parton momentum fraction x and the square of the momentum transfer Q^2. The modifications to the gluon PDF in a nucleus relative to that in a proton at a fixed x and Q^2 is shown in Fig. 2.8 as a function of mass number A.

Nuclear absorption

In addition to modified nPDFs, there is a significant chance that J/ψ will fail to form because $c\bar{c}$ precursors will interact with the medium while moving through the nucleus. This is called the "break-up cross-section" as in break up of a pair. Sometimes this is also referred as "absorption cross-section", which is a mis-leading term since charm quark pair still exists even if they become uncorrelated. In a Glauber formalism of $p + A$ collisions [32], this can be written as:

$$\sigma_{pa} = \frac{\sigma_0}{\sigma_{br}} \int db[1 - (1 - T_A(b)\sigma_{br})^A] \tag{2.3}$$

where σ_0 is the nucleon-nucleon charmonium production cross-section, σ_{br} is the $c\bar{c}$ break-up cross-section, $T_A(b)$ is the nuclear thickness seen by the impacting proton as a function of impact parameter b and A is the mass number of the nucleus. Currently there are no consensus on the value of J/ψ break-up cross-section from theory and generally it is extracted

from data.

Cronin effect

Partons undergo multiple scattering while they traverse the nuclei before producing J/ψ's. For instance, gluons from the projectile collide with various target nucleons modifying their transverse momentum at each collision vertex, will lead to a wider p_T distribution of J/ψ, compared to those in $p+p$ collisions, referred as the "Cronin effect" [33]. This leads to an increase of the average transverse momentum squared in A+A collisions

$$\langle p_T^2 \rangle_{AA} = \langle p_T^2 \rangle_{pp} + \frac{\langle \delta p_T^2 \rangle}{\lambda_{gN}} \langle L_{gN} \rangle \tag{2.4}$$

where $\langle p_T^2 \rangle_{pp}$ is the average squared transverse momentum of J/ψ in $p+p$ collisions. $\langle \delta p_T^2 \rangle$ is the average of added squared transverse momentum by one gluon-nucleon scattering and λ_{gN} and $\langle L_{gN} \rangle$ are the mean free path and average path length of the gluon in uniform nuclear matter before it produces a charmonium.

2.4 Final State Effects

Final state effects of J/ψ production are detailed in this section:

Color screening

While the discovery of J/ψ was a big milestone in our understanding of quark-antiquark bound states, the suppression of J/ψ would indicate the existence of Quark Gluon Plasma. In the hot-dense QCD medium produced in heavy ion collision, when the temperature is well above the critical temperature, the J/ψ and it's excited states are expected to melt. This was first predicted by Matsui and Satz in 1986 [13]. If a QGP medium is formed, production of J/ψ and other quarkonium bound states would be suppressed by color screening. Suppression does not imply that $c\bar{c}$ was not produced, but rather a depletion of the observed J/ψ's relative to the expected yield either because $c\bar{c}$ pair fails to form a J/ψ or J/ψ itself is destroyed through its subsequent interactions. This suppression is supposed to be an ideal test of the

$$\text{(a)} \quad V(r) = \kappa r - \frac{\alpha_{eff}}{r} \qquad \text{(b)} \quad V(r) = -\frac{\alpha\ e^{-r/\lambda_D}}{r}$$
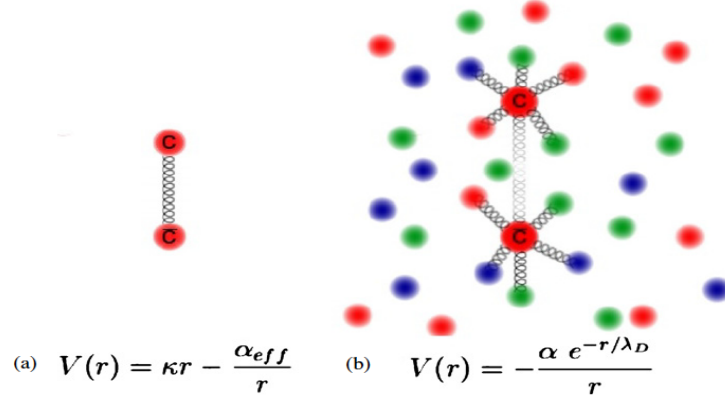
Figure 2.9: $c\bar{c}$ pair potential energy in (a) vacuum and (b) in QGP [34].

deconfinement and phase transition.

In a medium of charged particles Debye screening occurs when the interactions of one charge is reduced or canceled through screening by the surrounding medium. The idea was taken from electro-magnetic interactions but it applies to color-charge as well. Inside QGP, since quarks are freely floating, we would expect a color-screened coulombic potential [34],

$$V(r) = -\frac{\alpha_{eff}}{r} exp[-r/\lambda_D] \tag{2.5}$$

where λ_D is called the Debye screening radius, the radius at which the effective charge of a particle is reduced by a factor of 1/e. Fig. 2.9 shows the potential energy between a charm and anti-charm quark in vacuum and QGP. Note that the linear term in the (Eq. 1.1) of quark potential model, would disappear as the plasma temperature T approaches the transition temperature. When the screening radius λ_D becomes less than the binding radius $r_{J/\psi}$ of the J/ψ bound state, the confining force can no longer hold the quarks together and deconfinement sets in. This phenomena is true for any other quarkonia $(q\bar{q})$ states as well.

Lattice QCD also predicted the presence of strong screening above deconfinement, determined from the free energy of a static quark-antiquark pair [35]. The dissociation temperature for different charmonium and bottomonium states from lattice calculations are listed

Table 2.1: Dissociation temperature T_D/T_c for quarkonia inferred from lattice QCD calculations [35].

Resonance	J/ψ	χ_c(1P)	ψ' (2S)	Υ (1S)	χ_b (1P)	Υ (2S)	χ_b (2P)	Υ (3S)
T_D/T_c	2.10	1.16	1.12	$\geq$4.0	1.76	1.60	1.19	1.17

in Table. 2.1. However, the picture as laid out by Matsui and Satz "We thus conclude, that there appears to be no mechanism for J/ψ suppression in nuclear collisions except the formation of a deconfining plasma, and if such a plasma is produced, there seems to be no way to avoid J/ψ suppression", is not entirely correct, because there are also other possible effects as discussed next, which also could lead to suppression of J/ψ.

Recombination of J/ψ

Recent theoretical models predict that the J/ψ yield would be enhanced due to the recombination of uncorrelated $c\bar{c}$ pairs at RHIC energy, where these charm quarks are in abundance created by many nucleon-nucleon collisions [36, 37, 38]. In this scenario, it is assumed that the number of J/ψ is from recombination is approximately proportional to N_c^2/N_h, where N_c and N_h are the number of created charm quarks and produced hadrons. Though the relative scale is unknown but this effect is not negligible at RHIC energies because charm production cross section increases faster with $\sqrt{s}$ and scales with the number of nucleon-nucleon collisions. In some statistical models it is assumed that the initially produced J/ψ's from hard scattering are all dissociated in QGP and those which observed experimentally are mainly due to regeneration from charm and anti-charm quarks in the QGP [39]. It is difficult to discriminate the two models based on the finally produced J/ψs. It should be noted that the charm production, such as cross section as function of charm p_T, rapidity and its modification in hot and dense medium need to be understood first in order to study the recombination of J/ψ. At RHIC energy, the charm production cross-section is factor $\sim$2 compared to theory calculations and the rapidity shape is flatter than that expected from theoretical models [40]. In Au+Au collisions at RHIC, it has been observed

that charm quarks loose sufficient energy in hot dense medium [41]. These effects needed to be well accounted for before predicting the regenerations in heavy ion collisions.

Comover Interactions of J/ψ

The comover scattering of charmonia is an additional absorption of charmonia states by secondary hadrons, called comovers, which occurs in the hadronic phase [42, 43]. The survival probability of charmonia, S_{co}, can be expressed as follows:

$$S_{co} = exp(-\int d\tau \rho_{co}(\tau)\sigma_{co}v) \qquad (2.6)$$

Where $\rho_{co}(\tau)$ is the comover density at the proper time τ, σ_{co} is the charmonium absorption cross section by comovers and v is the velocity of charmonium relative to a comover. Although it is difficult to theoretically model the dissociation cross section of J/ψ with co-mover's model, there are few models which takes into account the dissociation process by comovers, and can reproduce the J/ψ suppression at SPS energies with dissociation cross section σ_{co} of 0.65 mb [44, 45].

Furthermore, directly produced J/ψ with high p_T may escape from QGP produced in heavy ion collisions without any interaction, which is called "leakage effect". Another physical effect that has been proposed is that of initial state parton energy loss. In a recent calculation [46], the initial-state parton energy loss is presented and its impact on J/ψ production in p+A collisions. In the case of initial-state radiative energy loss, they modeled $\Delta E/E \propto L^2$, assuming a quadratic path dependence for energy loss.

2.5 Experimental J/ψ Measurements

To date, chamonia productions and their suppression have been extensively studied experimentally at various particle colliders. In 1980's various experiments were carried out at Alternating Gradient Synchrotron (AGS) at BNL and Super Proton Synchrotron (SPS) at the European Center for Nuclear Research (CERN) [47, 32, 48]. The RHIC at BNL started its operation at 2000 [1]. Recently Large Hadron Collider (LHC) at CERN started their

operations at the highest level of energy ever achieved by any other experiments [49, 50]. Table. 2.2 shows a list of the collider experiments. In the next sections a brief review of experimental J/ψ studies from those experiments are discussed.

Table 2.2: Particle collider experiments.

Accelerator	Collision energies per nucleon	Collision species
AGS (BNL, 1986-)	∼5 GeV	$p + A, O + A, Si + A, Au + Au$
SPS (CERN, 1986-)	17.3, 19.4 GeV	$p + A,\ S + U,\ Pb + Pb,\ In + In$
Tevatron (FNAL) (1987-2011)	39 - 1.8 TeV	$p + \bar{p}\ p + Be, p + Fe, p + W$
RHIC (BNL, 2000-)	39, 62.4, 200, 500 GeV	$p + p,\ d + Au,\ Au + Au,\ Cu + Cu,$ $Cu + Au,\ U + U$
LHC (CERN, 2008-)	2.76, 5.5, 7 TeV	$p + p,\ Pb + Pb, p + Pb$

SPS Measurements

The NA38, NA50, NA51 and NA60 experiments at the CERN-SPS studied J/ψ production in light and heavy-ion collisions through their decay into dimuon pairs [47, 32, 48]. Nuclear targets include Be, Au, Cu, Ag, W, O, U and Pb with proton beams. The production cross-section was extracted relative to the production of Drell-Yan (DY) pairs. It is assumed that the DY production gets scaled with the number of inelastic nucleon-nucleon collisions without any modifications. Fig. 2.10 shows the J/ψ production relative to DY as a function of the effective path lengths of J/ψ's in nuclear collisions. As seen in the figure, except for the central $Pb + Pb$ collisions, the relative J/ψ cross-section follow an exponential function, which suggests that the nuclear absorption was the cause for modifying the J/ψ yield. An absorption cross-section of σ_{abs} =4.18±0.35 mb was extracted for SPS [51]. A clear deviation of J/ψ suppression from the normal nuclear absorption pattern is seen for heavy ion $Pb + Pb$ collisions, which was interpreted as the evidence of deconfinement at SPS.
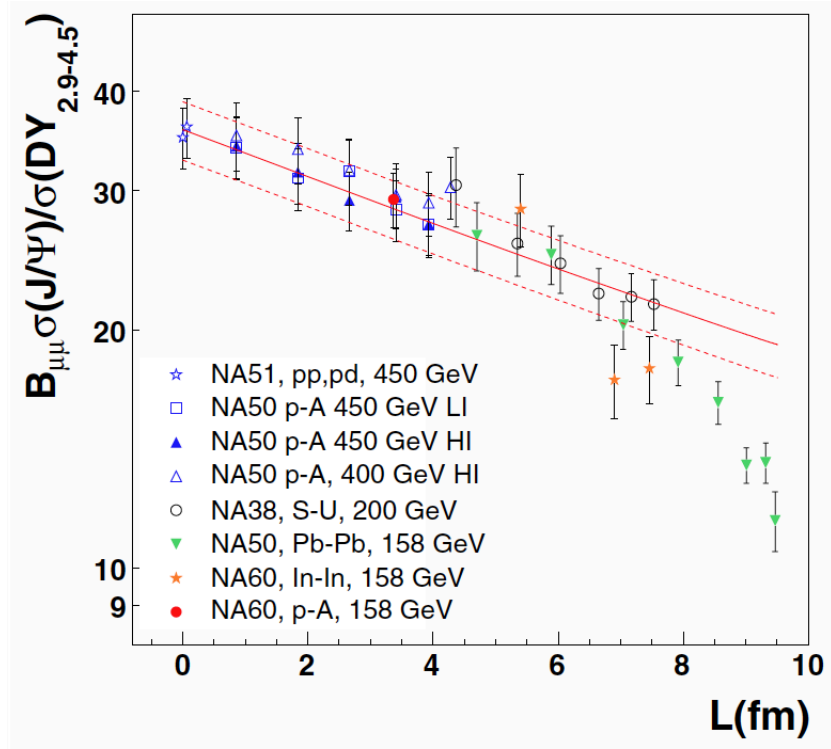
Figure 2.10: J/ψ production relative to DY production as a function with path Length L for several collision systems. Normal nuclear absorption pattern is also shown in solid line. A clear deviation from normal nuclear absorption is seen for $Pb + Pb$ collision.

The additional suppression in $Pb + Pb$ collisions suggests a medium similar to Quark Gluon Plasma was formed in heavy ion collisions.

Fermilab Measurements

Fermilab E866/NuSea measured J/ψ and ψ' nuclear dependence for proton-nucleus collisions, while throwing proton beams on Be, Fe and W fixed targets at $\sqrt{s} = 39$ GeV [52]. As shown in Fig. 2.11, the nuclear modification factor α decreases at higher x_F. The x_F is Feynman x which refers to the fraction of the maximum allowed momentum that the J/ψ or $c\bar{c}$ have, or roughly speaking how fast they are going. The nuclear modification α was obtained assuming the cross-section dependence on the nuclear mass, A, has the functional form, $\sigma_A = \sigma_N \times A^\alpha$, where σ_N is the cross-section of a nucleon. As can be seen, the suppression for the ψ' is stronger than that for the J/ψ for x_f near zero but
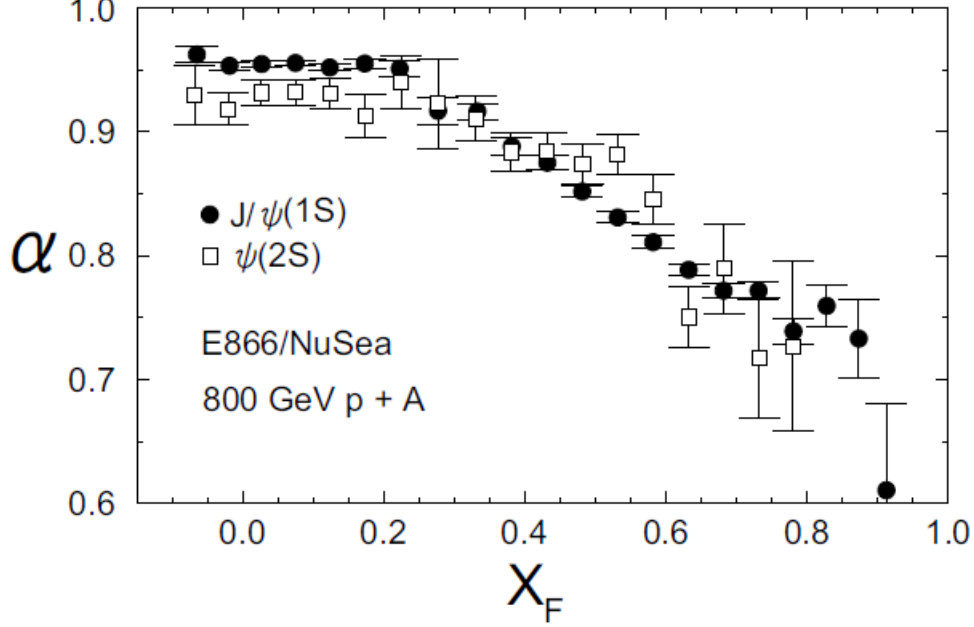
Figure 2.11: nuclear modifications for J/ψ and ψ' vs x_F at E866/NuSea experiments [52].

becomes comparable to that for the J/ψ for $x_F > 0.6$. The J/ψ nuclear modification α can be represented for convenience by a simple parametrization $\alpha(x_F) = 0.960(1 - 0.0519x_F + 0.338x_F^2)$.

RHIC measurements

At the RHIC collider J/ψ production has been measured by the PHENIX and STAR experiments [53, 54]. In PHENIX measurements, the J/ψ yield at $p+p$ was used as baseline measurement and relative modifications in $d + Au$ and $Au + Au$ are used to quantify the nuclear modifications e.g. CNM and QGP effects on J/ψ production [26, 55, 56]. At mid-rapidity ($|y| < 0.35$), J/ψ was measured via $e^- e^+$ pairs and at forward and backward rapidity ($1.2 < |y| < 2.2$) via $\mu^+ \mu^-$ pairs. PHENIX $p+p$ results are shown in Fig. 2.5 for J/ψ differential cross section times di-lepton branching ratio over a very wide rapidity range of acceptance. The data slightly favors a flatter distribution at mid-rapidity. The total cross section times the branching ratio determined for J/ψ production in 200 GeV $p+p$ collisions is $B_{ll}\sigma_{pp}^{J/\psi} = 178 \pm 3(stat) \pm 53(syst)$ nb. Fig. 2.6 shows the the J/ψ p_T distribution at 200 GeV

$p+p$ collisions. Mid-rapidity measurements were scaled up by 10^3 for a visual clarity. The theoretical curves show that, the next-to-leading order of NRQCD was able to successfully reproduce both the rapidity and p_T distribution in $p+p$ collisions at RHIC.

Phenix recorded d+Au collisions at $\sqrt{s}$ =200 GeV in order to study cold nuclear matter effects. The modification of J/ψ yield due to the nuclear target provides important insights into the evolution of $q\bar{q}$ pairs through nuclear matter. PHENIX wide acceptance in kinematic phase-space, rapidity and p_T provides a unique opportunity to study the nuclear environment over a broad kinematic range in order to disentangle different mechanisms. It was found that J/ψ is significantly suppressed in the deuteron going direction compared to $p + p$ collisions scaled by the number of binary collisions:

$$R_{dAu} = \frac{1}{\langle N_{coll} \rangle} \frac{d\sigma^{dAu}/dy}{d\sigma^{pp}/dy} \tag{2.7}$$

where $\langle N_{coll} \rangle$ is the average number of nucleon-nucleon collisions and is determined from Glauber simulations [57]. The top panel of Fig. 2.12 shows the J/ψ rapidity yields in $d+Au$ minimum bias (MB) collisions scaled by $\langle N_{coll} \rangle$ along-with $p+p$ yields for comparison. A clear suppression can be seen at forward rapidity, the bottom panel shows the nuclear modification factor R_{dA} at $\sqrt{s}$ =200 GeV. A model prediction, including the nPDF shadowing from EPS09 parametrization and an absorption cross section of $\sigma_{abs} = 4$ mb is also shown in the same figure. A higher suppression of J/ψ is observed as one goes in the forward direction (in the d-going direction), corresponding to a region sensitive to initial state low-x gluons in the Au nucleus. The value of the break-up cross section is consistent within uncertainties with that measured in SPS [55].

Measuring J/ψ modifications in heavy ion collisions $(A + A)$ can help us quantify the color screening length in the QGP. In order to quantify those hot nuclear matter effects, PHENIX also measured the J/ψ modification in Au+Au collisions. But before extracting the QGP effects on J/ψ production, a detailed understanding of the baseline J/ψ production, as well as CNM effects present in heavy ion collision, is required. Fig. 2.13 shows the nuclear
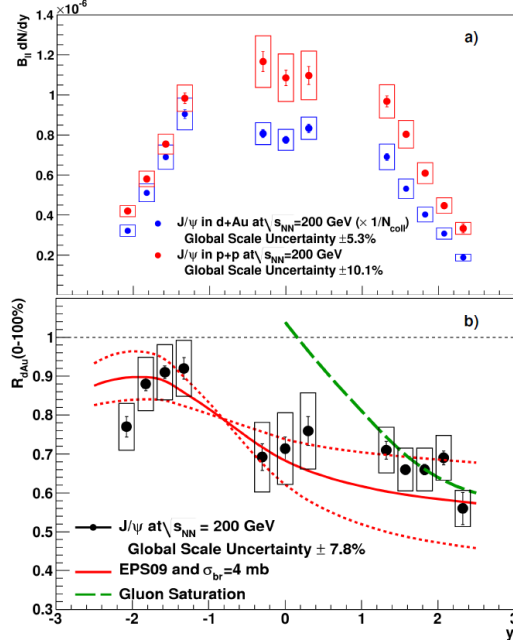
Figure 2.12: (a) J/ψ rapidity distribution in p+p and d+Au collisions and a higher suppression can be seen at forward rapidity than backward rapidity. (b) R_{dAu} nuclear modifications [55].

modification factor as a function of number of participant nucleons at $\sqrt{s} = 200$ GeV [56].

$$R_{AA} = \frac{1}{\langle N_{coll} \rangle} \frac{dN^{A+A}/dy}{dN^{p+p}/dy} \qquad (2.8)$$

A strong suppression by a factor of 4 and 6 is observed in central collisions at mid and forward rapidity respectively. However, the observed PHENIX R_{AA} is at the similar level to that seen in the NA50 experiment. This was very surprising, since the RHIC energy density is much higher than that achieved by SPS and a higher suppression was expected. Adding more to the puzzle, the forward-rapidity suppression is higher than that at mid-rapidity. The ratio of forward/mid rapidity R_{AA} first decreases then reaches about 0.6 for $N_{part} > 100$. This contradicts simple energy density picture of suppression, where the energy density is supposed to be higher at mid-rapidity than forward rapidity. Hence a less J/ψ suppression at forward rapidity was expected. The lack of energy dependence of the J/ψ R_{AA} is still a
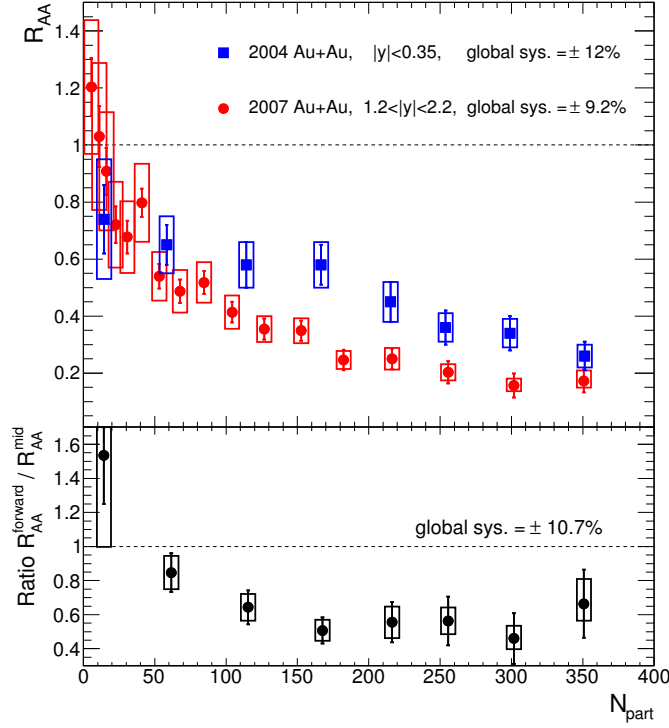
Figure 2.13: J/ψ nuclear modification factor R_{AA} as a function of number of participants for Au+Au collisions. Blue points are mid-rapidity points and red points are forward-rapidity points [56].

puzzle for theorists.

LHC measurements

The LHC collider, started its operation at 2010 in much higher energy regime than any particle collider ever built. In 2010, four experiments CMS, ALICE, ATLAS and LHCb collected data at 7 TeV $p+p$ and 2.76 TeV $Pb + Pb$ collisions [49, 50]. It is obvious that at this energy, the medium created by heavy ion collisions was well above the critical temperature. In particular, at the energies available at LHC a large number of heavy quarks are produced which could lead to an increased production of quarkonia via statistical recombination. Hence, in addition to CNM and QGP effects on J/ψ production a significant contribution from recombination must be accounted for.
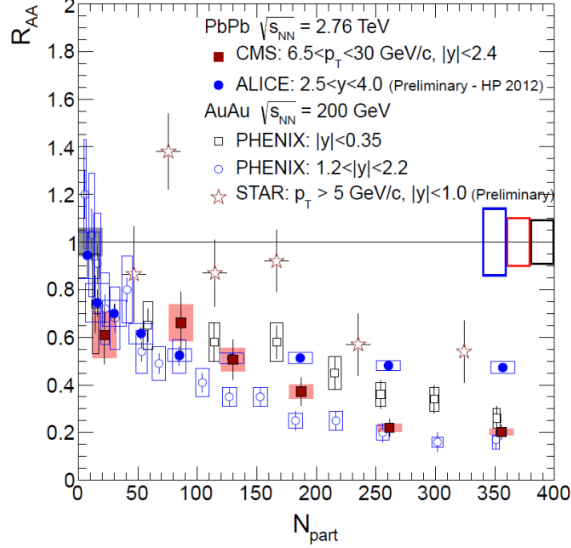
Figure 2.14: The nuclear modification factor of prompt J/ψ as a function of centrality [49].

Figure 2.15: The nuclear modification factor of non-prompt J/ψ as a function of centrality [49].

The CMS experiment is the first experiment to be able to separate non-prompt and prompt J/ψ production in heavy ion collisions through the dimuon channel. Non-prompt J/ψ's from b-hadron decays and prompt J/ψ's were separated by a two dimensional fit to the invariant mass and the transverse distance between the collision vertex and reconstructed secondary vertex of the $\mu^+\mu^-$ pair [49]. Fig. 2.14 shows a strong centrality-dependent suppression for prompt and non-prompt J/ψ. In peripheral $Pb + Pb$ collisions, the suppression is three times smaller than in the most central collisions. A high-p_T J/ψ measurement by STAR at RHIC shows much smaller suppression, while the suppression is similar to the one measured by PHENIX. The ALICE R_{AA} measurement of low-p_T inclusive J/ψ's at forward rapidity shows almost no centrality dependence [58]. It is noteworthy that the difference between the strong suppression measured at high-p_T J/ψ and low-p_T J/ψ, might be a sign of significant recombination.

At LHC energies the inclusive J/ψ yield would contain a significant non-prompt contribution from B-hadron decays. Since the lifetime of B hadrons ($\sim 500\mu m/c$) is much

longer than the formation of QGP ($\sim 10 fm/c$), this contribution should not suffer from color screening. Instead the reduction in the non-prompt J/ψ yield could reflect the b-quark energy loss in the medium. Fig. 2.15 shows that non-prompt J/ψ's are also suppressed by a factor of ~ 2.6 with respect to the $p+p$ collisions for the central collision.

2.6   Motivation For This Study

The motivation for this study is to perform a systematic study of hot and dense matter created in heavy-ion collisions at RHIC. As discussed in previous sections, the J/ψ suppression is surprisingly similar in SPS, RHIC and LHC. The consensus is that the different competing effects contributing to the modification of J/ψ yields varies with energy, but their cumulative of those effects might be similar at those measured energies. In order to distinguish those effects, as well as to determine the onset of the quark gluon plasma, we need measurements at a very wide range of energies. There are energy gaps between SPS ($\sim 20 GeV$) to RHIC ($\sim 200 GeV$) to LHC ($\sim 2.6 TeV$). The RHIC energy scan program, started in 2010, provides a unique opportunity to study J/ψ production in heavy ion collisions as a function of medium energy density and system sizes by exploring the energy gap between SPS and RHIC. This effort is crucial for quantifying the significance of J/ψ as a probe for studying the signatures of the formation of Quark Gluon Plasma in relativistic heavy ion collisions. During 2010, PHENIX recorded 600 million Au+Au MB events over three weeks of running at $\sqrt{s_{NN}} = 62.4$ GeV and 200 million MB events at 39 GeV. In this study, the details of the analysis and results of J/ψ measurement at PHENIX muon arm at 39 and 62.4 GeV are presented.

CHAPTER 3

EXPERIMENT

3.1   RHIC

The Relativistic Heavy Ion Collider (RHIC) located at Brokhaven National Laboratory, NY, is a hadron collider, made to accelerate a wide variety of nuclei and ions from protons to deuterium, copper, gold and uranium ions. It started its operation in 2000. The main purpose of RHIC is to recreate the extreme densities and temperature of the hadronic matter and study their properties. Early investigations of such experimental facilities at Berkeley Bevalac (1975-1985), the BNL AGS (1987-1995) and the CERN SPS (1987-present) have reached their culmination with the commissioning of BNL's RHIC, a dedicated facility for the study of nuclear collisions at ultra-relativistic energies. A schematic view of RHIC is in Fig. 3.1. At the beginning, four RHIC experiments BRAHMS, PHENIX, PHOBOS and STAR were built at four of the six intersection points to study these collisions.

- BRAHMS: Broad RAnge Hadron Magnetic Spectrometers Experiment.

- PHENIX: Pioneering High Energy Nuclear Interaction eXperiment.

- STAR: Solenoidal Tracker at RHIC

- PHOBOS: Named after the moon of Mars.

RHIC has been able to deliver collisions with the different nuclei species (Au+Au, Cu+Cu, d+Au) at over a wide range of center of mass energies, $\sqrt{s}$=7-200 GeV, as well as protons up to $\sqrt{s}$= 500 GeV. The RHIC complex consists of Tandem Van de Graaff, Booster Accelerator, Linear Accelerator Complex (LINAC), Alternating Gradient Synchrotron (AGS) and the main rings of the Relativistic Heavy Ion Collider (RHIC). The process for accelerating of follows: heavy nuclei ions are first accelerated by a Tandem Van de Graaff to 1 MeV,
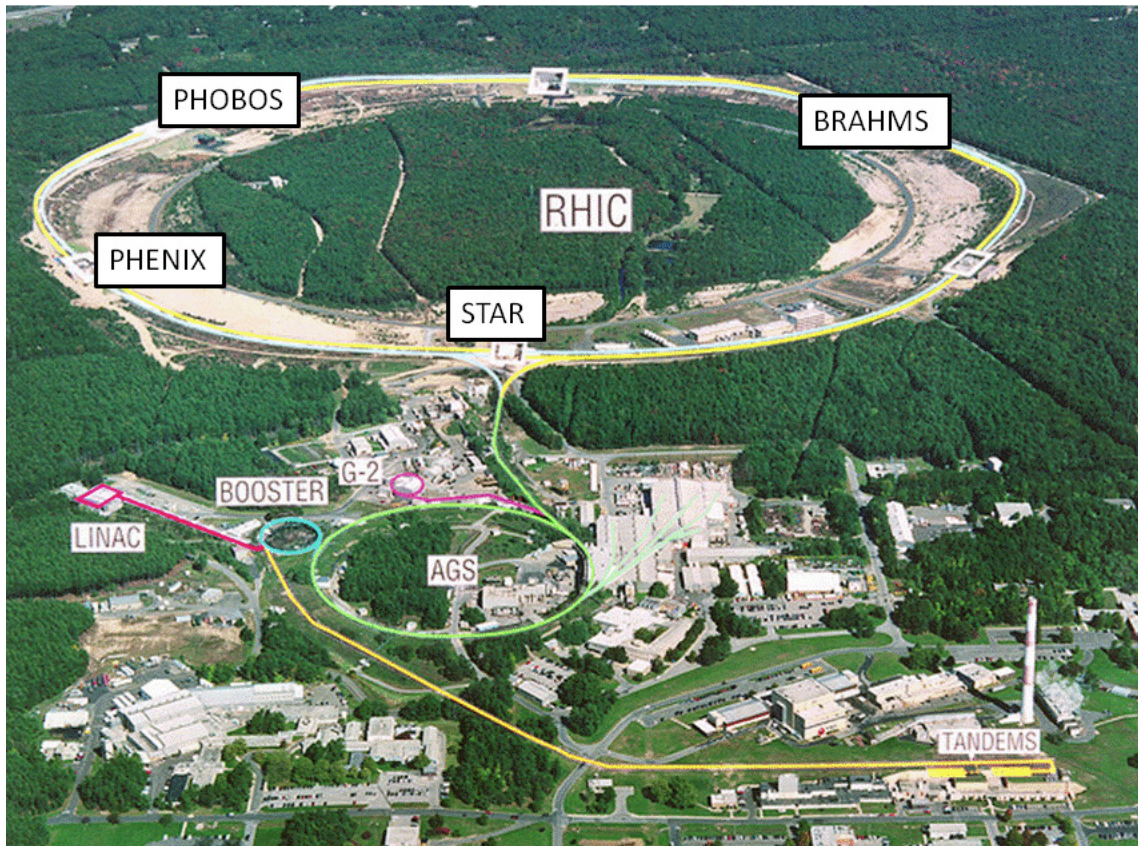
Figure 3.1: The Relativistic Heavy Ion Collider Facility.

then by the Booster Synchrotron up to 95 MeV and finally by the Alternating Gradient Synchrotron (AGS) to 10.8 GeV and then the beam get injected into RHIC's blue and yellow rings. At this stage heavy ions have been stripped of all the electrons and are finally accelerated to the desired energies at RHIC ring.

Four experiments start taking data in 2000. By 2006 BRAHMS and PHOBOS had achieved their physics goals and have been decommissioned. Among current experiments, PHENIX is designed specially to measure electrons, muons and photons from rare probes and STAR is designed to use a large time projection chamber to track charged particles over a large geometrical acceptance.

3.2   PHENIX Experiment

The PHENIX experiment probes several fundamental features of the strong interaction. PHENIX is able to probe different phases of heavy ion collisions by virtue of it's ability to measure the rare processes that involves photons, electrons and muons as well the predominant hadronic production. A recent photograph of PHENIX detector is shown in Fig. 3.2. The PHENIX detector consists of a number of subsystems which can be categorized into four groups: beam detectors, magnets, central arms and muon arms. The beam detectors are used for triggering and event characterization. One central magnet and two muon magnets generate magnetic fields to enable us to measure the momenta of charged particles [59]. The rapidity coverage and azimuthal acceptance of this subsystem is given in Table 3.1. They consist of Zero-Degree Calorimeters (ZDC) and Beam- Beam Counters (BBC). A pair of ZDC's detect neutrons from grazing collisions and form a trigger for the most peripheral collisions. The ZDC is used by all four RHIC detectors. A pair of BBCs provide a measure of the time-of-flight of forward particles to determine the time of a collision, provide a trigger for the more central collisions and provide a measure of the collision position along the beam axis [60]. A side view of the PHENIX detectors are shown in Fig 3.3. The top panel shows the central arm, which located on each side of the interaction region and consist of tracking system for charged particles and electro-magnetic calorimetry. The calorimeter is the
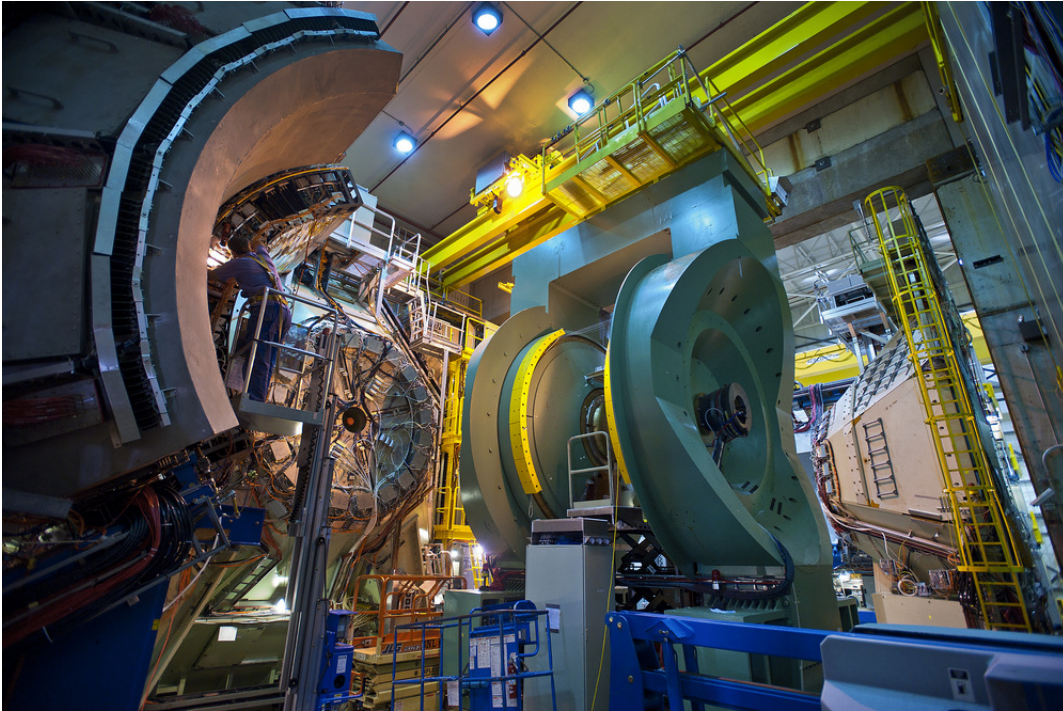
Figure 3.2: PHENIX detector.

outermost subsystem on the central arms and provides measurements of both photons and energetic electrons. The rapidity coverage of the central arm is $|\eta| < 0.35$. It includes the Drift Chamber (DC), two layers of Pad Chambers (PC1 and PC3), Ring Imaging Cerenkov Counter (RICH), Time Expansion Chamber (TEC), Time of Flight detector (TOF) and Electromagnetic Calorimeter (EMCal) [61, 62, 63]. The bottom panel of Fig. 3.3 shows the muon arms, which optimized for detection of muons in the forward and backward rapidity regions $(1.2 < |\eta| < 2.4)$. Each arm consists of a Muon Tracker (MuTr), a Muon Identifier (MuID) and Resistive Place Chambers (RPC) [64]. The beam pipe is at the center and is 76 mm in diameter and 1.0 mm in thickness. Since this work is based on the J/ψ analysis through the dimuon channel detected in the muon arms, we are only going to discuss PHENIX muon arm detectors in detail. Details about central and global detectors can be found elsewhere [65].
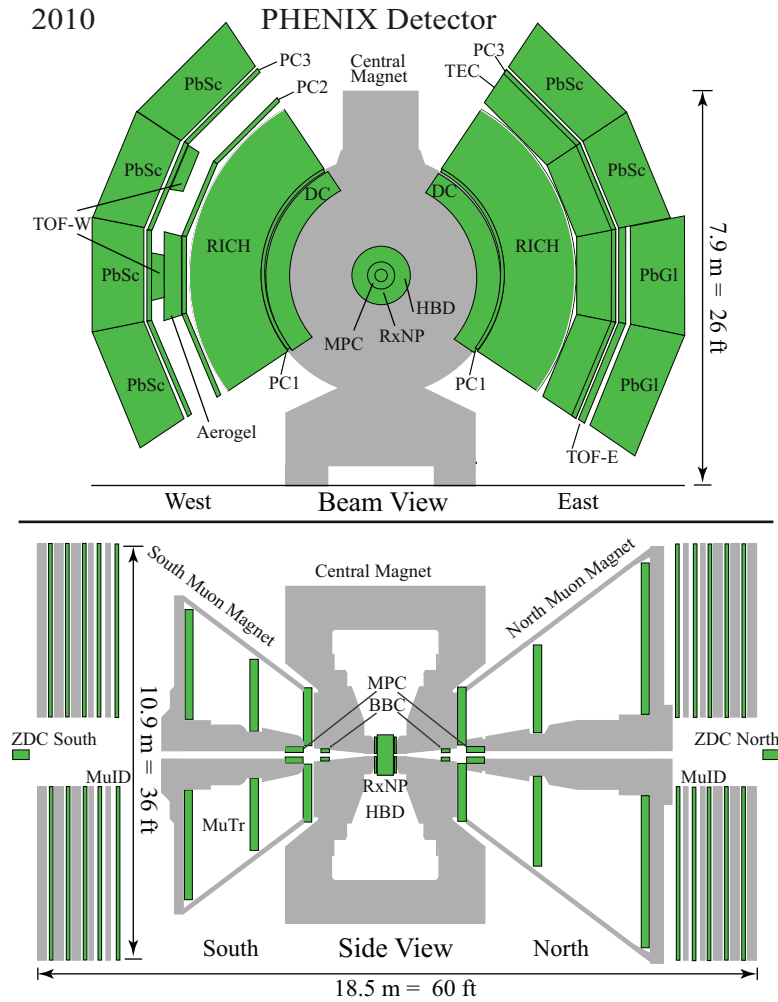
Figure 3.3: PHENIX detector configuration during Run-10. Top half is the XY plane view of the Central Arm. Bottom half is the YZ plane view of the Muon Arm [66].

Table 3.1: PHENIX detectors [65].

Subsystem	$\Delta\eta$	$\Delta\phi$	Purpose and special features
BBC	$\pm 3.1 - 3.9$	$360°$	trigger, vertex, timing
			and geometry determination.
ZDC	± 2 mrad	$360°$	trigger, vertex, timing
			and geometry determination.
DC	± 0.35	$90° \times 2$	Good momentum and mass resolution
			$\Delta m/m$=1.0% at m=1 GeV
PC	± 0.35	$90° \times 2$	Pattern recognition,
TEC	± 0.35	$90°$	Pattern recognition, dE/dx,
RICH	± 0.35	$90° \times 2$	Electron identification
TOF	± 0.35	$45°$	Good hadron identification
EMCal	± 0.35	$90° \times 2$	photon and electron identification
			and energy measurement
MuTr	$\pm 1.2 - 2.2$	$360°$	Tracking for muons
MuID	$\pm 1.2 - 2.2$	$360°$	muon/hadron separation
RPC	$\pm 1.2 - 2.2$	$360°$	Muon triggering

3.3 Muon Spectrometers

Two muon spectrometers at PHENIX forward angles are at rapidities of $-2.25 < y < -1.15$ for the south arm and $1.15 < y < 2.44$ for the north arm. Each spectrometer has full azimuthal acceptance and consists of an initial hadronic absorber followed by three sets of cathode strip chambers, referred to as the Muon Tracker (MuTr), which is inside a radial magnetic field, followed by five planes of Iarocci tubes interleaved with steel absorber plates, referred to as the Muon Identifier (MuID). Muon candidates are found by reconstructing tracks through the magnetic field in the MuTr and matching them to MuID hits penetrating

through to the last plane. The Initial absorber is made of 60 cm of low-carbon steel and a 20 cm brass absorber pointed towards the interaction region to absorb the hadronic background and take advantage of penetrating abilities of muons. In the absorber layer these hadrons undergo strong interactions and stop with a probability 1-exp(-L/Λ), where L is the path length in the absorber material and Λ is the nuclear interaction length for different species. In terms of muon interaction length, the absorber is 5Λ long. The primary goal of the absorber is to reduce the background from pions to make meaningful muon measurements. The backplate of the Muon Magnets adds 20 cm of steel in South Arm and 30 cm in North Arm. Finally there are four layers of steel in the MuID, with thickness of 10, 10, 20 and 20 cm, that particles must pass through to reach the last detecting layer. This would provide two orders of magnitude rejection of pions and kaons ($\sim 10^2$). The inclusive muon candidates (N_I) are those, which are successfully reconstructed at the last plane of the MuID (gap 4). These muons has contribution from different sources: 1) "decay muons (N_D)" which are from π or K that decay before reaching the absorber, 2) "punch through hadrons (N_P)" which penetrate the entire detector and are misidentified as muons, and 3) muons from heavy flavor decay (N_μ). Fig. 3.4 shows a schematic depiction of the relative yield per event of different components of the inclusive muon candidates reconstructed in the muon arm. As seen in the figure, most of these interacting hadrons are effectively eliminated as possible muon candidates.

Muon Tracker

The Muon Tracker is made of three stations of cathode-strip readout tracking chambers mounted inside conical-shape muon magnets and has multiple cathode strip orientations and readout planes in each station. With this kind of design, the cathode planes provide 100 μm resolution measurements of the particle trajectories. A unique wire laying apparatus was designed and implemented for each station. The anode planes are alternating structures of 20 μm gold-plated W sense wires and 75 μm gold-plated Cu-Be field wires with a sense wire sparking of 10 mm. Half of the cathode planes have strips perpendicular to the anode wires and other half have strips at stereo angles between 0 and ± 11.25 deg with respect to
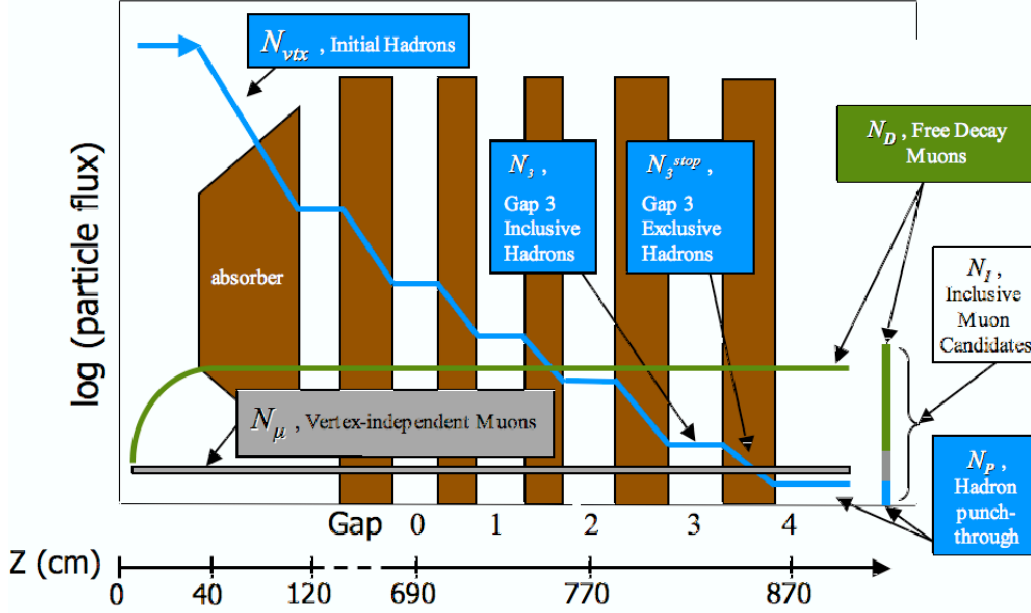
Figure 3.4: A schematic view of relative flux of different component of inclusive muon candidate [67].

the perpendicular strips. Two layers of cathode strips are on either side of a layer of anode wires, the combination of which is referred as a gap or gas gap. These gaps are then group into three stations, with station 1 and 2 having 3 gaps and station 3 have two gaps, a total of 8 gaps and 16 cathode planes. A schematic view of different stations is in Fig. 3.5. A gas mixture of $50\% \ Ar + 30\% \ CO_2 + 20\% \ CF_4$ is used and proper gas recirculation system has been implemented. The typical operating conditions is with high voltage of 1850 V and a gain of approximately 2×10^4. With this kind of setup, the charge deposited by a minimum ionizing particle in the cathode planes is ~ 100 electrons. This would result in an average cathode charge of 80 fC with a Landau charge distribution. Tracking layers are roughly radial magnetic field (shown in Fig. 3.6), such that particles coming from the interaction point will bend mostly in the ϕ-direction. Stations 2 and 3 were constructed as separated octants, with the strips oriented together within each half-octant. Due to station 1's smaller size, it was build as quadrants but the strip layout was still done in octant's in order to match with other stations. With this kind of position resolution a relative mass resolution
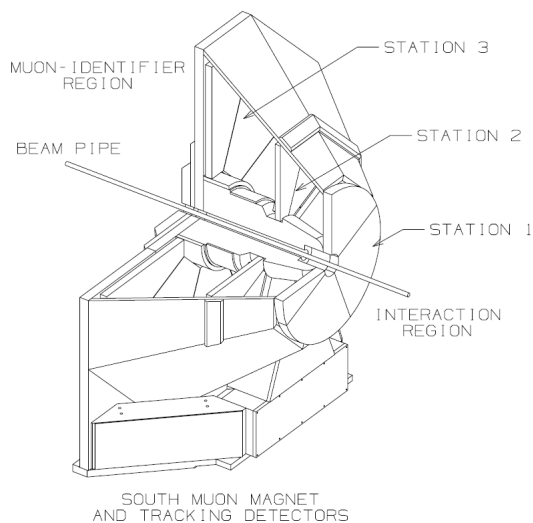
Figure 3.5: PHENIX muon tracking spectrometer (south arm) [64].
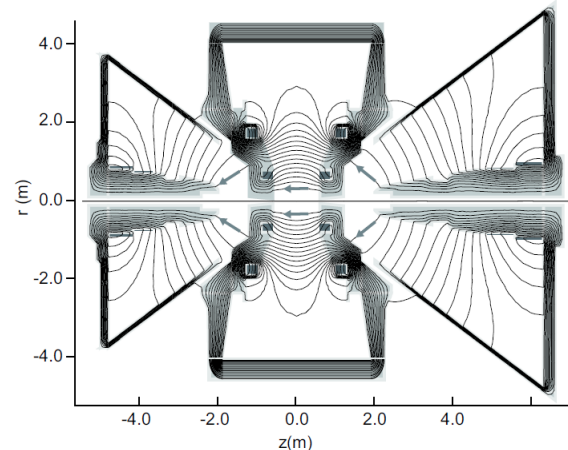
Figure 3.6: Magnetic fields in PHENIX. The beams travels along r=0-axis in this figure and collide at r=z=0. Arrows indicate the field direction [64].

from the reconstruction of a muon pair is approximately $\sigma(M)/M = 9\%/\sqrt{M}$, where M is the dimuon mass in GeV/c^2.

Muon Identifier

The muon identifier (MuID) consists of five layers of Iarocci streamer tubes interleaved with four layers of steel absorbers. The purpose of MuID was to reject hadron contaminations in an inclusive muon sample by requiring the muon candidates to pass through multiple layers of steel. It also provides fast muon and dimuon triggers, although specific to this thesis, for the Au+Au collisions analysis the minimum bias BBC trigger used which does not depend on any physics process. These Iarocci tubes consists of eight 100-μm gold coated CuBe anode wires within each 8.35 cm $\times$ 1.3 cm plastic casing, at the center of long channels of a graphite coated plastic cathode. A gas mixture of CO_2 (92%) and $i-C_4H_{10}$ (8%) is filled in the tubes. A two-pack is a pair of tubes connected together and staggered by half a channel. They are ORed together, allowing one tube to cover the other's dead area, resulting in higher overall efficiency. A cutaway view of a two-pack is shown in Fig. 3.7. Groups of two-packs oriented
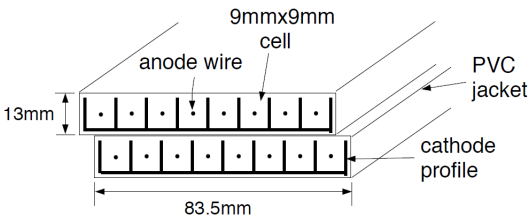
Figure 3.7: Cutaway view of two-pack with MuID Iarocci tubes [64].
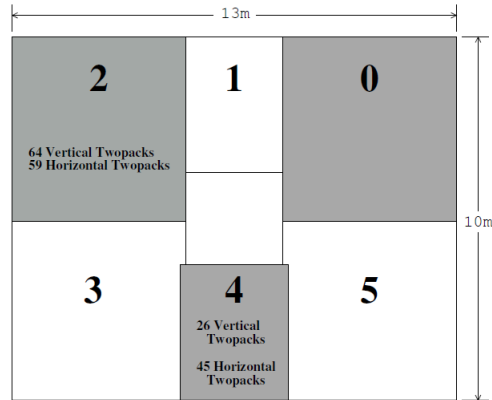
Figure 3.8: PHENIX MUID panels in south arm. Shaded panels are mounted closer to the interaction point [64].

both horizontally and vertically are held inside an aluminum box so that both projections are measured. A layer of MuID is divided in six panels which slightly overlap each other and reduce dead area. MuID panels are shown in Fig. 3.8, panels marked with 0,2,3,5 are longer panels with 64 vertical and 59 horizontal two-packs. While panels 1 and 4 are shorter in size and 26 horizontal and 45 horizontal two-packs. The tubes are operated in the proportional mode at 4500 V to increase longevity.

3.4 Trigger

PHENIX is designed to make measurements on a variety of colliding nuclei from $p+p$ to Au+Au. The online system has two levels of triggering denoted as LVL1 and LVL2. The Level-1 trigger (LVL1) is responsible for selection of special interesting events and rejecting uninteresting background events. LVL1 trigger is fully pipelined, therefore the online system is free of dead time through LVL1. The interaction rate of RHIC luminosity varies from few kHz for Au+Au central collisions to approximately 500 kHz for minimum bias $p+p$ collisions. The LVL1 trigger and lower levels of the readout are clock driven by bunch-crossing signals from the 9.4 MHz RHIC clock. LVL1 consists of two separate subsystem. One is the Local

Level-1 (LL1) system and another is the Global Level-1 (GL1) system. LL1 communicates directly with participating detectors such as BBC [68]. The BBC LL1 trigger (BBCLL1) is an event trigger based on a LL1 algorithm for each RHIC beam crossing. The timing information from BBC is used to select an event in nominal interaction region ($|z| < 50$ cm). The timing information about RHIC bunch crossing from north and south BBC is sent to BBCLL1 module to make a trigger decision. LL1 also gather information from other subsystems e.g. dimuon trigger using MuID, electron and photon triggers from EMCal-RHIC LL1 trigger (ERTLL1) to record a particular interesting event. The GL1 receives and combines all the LL1 data to make a combined trigger decision, which decides whether the event should be recorded or not. The higher level of readout and LVL2 trigger are data-driven where the results of triggering and data processing propagate to the next higher level only after processing of a given event is completed.

The PHENIX experiment defines BBCLL1 as the minimum bias (MB) trigger which is used for taking MB events and studies of global variables, trigger efficiencies etc. This MB trigger is used for this thesis analysis.

3.5   Data Acquisition

The PHENIX Data Acquisition System (DAQ) is designed to record data at very high rates and volumes both for $p+p$ and high multiplicity events. It is designed to accommodate the improvements in design luminosity provided by RHIC each year. The overall data flow is shown schematically in Fig. 3.9. Signals from various PHENIX subsystems are processed by Front End Modules (FEM) that convert detector signals e.g. charge deposited on a cathode wire, or the electron avalanche in a photo-multiplier tube into a digital format. FEMs store signals from an adjustable latency of some 40 beam crossings (every 106 ns) in a digital buffer. This involves analog signal processing with amplification, development of trigger input data and sufficient buffering to allow time data processing by the LVLL1 trigger and digitization. This is carried out for all detector elements at every beam crossing synchronously with RHIC beam clock.

Once the decision is made to accept an event, the data fragments from FEMs are sent over fiber optic connections to the Data Collection Modules (DCMs). In this section zero suppression occurs, a procedure which removes samples that are below a threshold and low enough to be considered as signal, as well as more specific tests for different subsystems. All electronics include embedded firmware contained in field-programmable gate arrays (FPGAs). The event data from several DCMs are collected together and sent to Event Builder (EvB). Two most important features of the EvB are the maximum event rate performance and the aggregation of data from several DCMs. The EvB is set to process events at an input rate of 12.5 kHz and to handle aggregate data rates as high as 500 MB/s. "Sub-event Buffers" (SEBs) would receive and buffer data from DCMs and transfer them on request to a set of "Assembly /Trigger Processors" (ATPs) under the control of "EvB Controller" (EBC). At this stage, an event number is assigned for the data compiled by ATPs from collected from SEBs and sends a "flush" message to the SEBs when an assembly has been completed. The event data is collected from the ATPs and merged into six buffer boxes, which are Linux-based storage devices with sixteen hard drives in a RAID array. These buffer boxes store the data in the PHENIX experimental hall temporarily until, upon the declaration of a good run from the shift leader, the data is transferred to a permanent tape storage in the RHIC High Performance Storage System (HPSS).
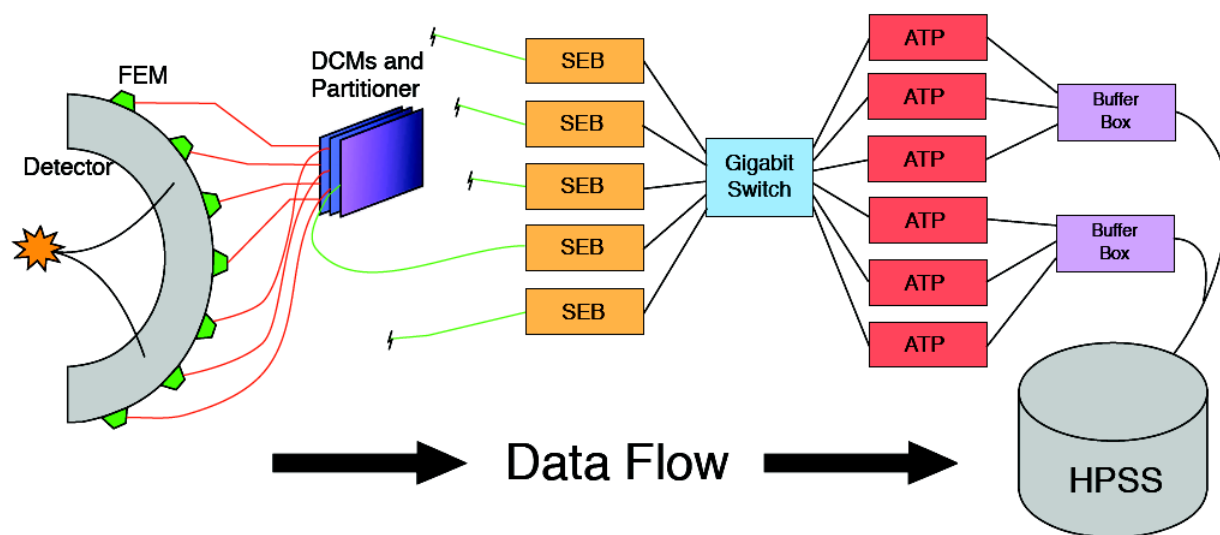
Figure 3.9: DATA collection by PHENIX data acquisition system.

CHAPTER 4

MUON SOFTWARE

Track reconstruction in the Muon Arms are performed by using standard C++ object-oriented software, called "MUTOO" for MuTr and "MUIOO" for MuID [69]. Software modules are then run within the standard PHENIX Fun4All data processing framework, which provides access to the data on an event-by-event basis. Significant focus was given during the muon software development to provide an environment that enables physicists to develop analysis in an environment that is safe, easy to use, and promotes modularity. MUTOO makes extensive use of ROOT, a data analysis framework developed at CERN [70], the C++ Standard Template Library, GNU Scientific Library and the Boost Libraries. The analysis software of the PHENIX muon spectrometer is a collection of Interface Objects (IO) for each particular stage of the analysis chain. IOs provide protected data access as well as a persistent storage of analysis primitives in data summary tapes (DSTs). The well defined tasks for these IOs impose a level of modularity in the analysis software. For example, TMutHit interface objects are the hit objects which represent calibrated, as well as un-calibrated raw charge data for active cathode strips in the MuTr. A collection of IOs are called Interface Object Containers (IOC) which provide safe and efficient access to subsets of IOs associated with particular detector. A loose analogous to IOC's are C-style arrays. These provide storage for a collection of objects and provide an interface for sequentially accessing the objects they contain. These also implement the object associations between different stages of analysis. For example, a cluster object is associated with the number of hit objects that make it up. Some basic criteria which were strictly enforced in the software:

- Interface objects are simple enough to be ROOT-streamable using the rootcint generated streamers.

- Interface objects must have a pure abstract class that contain no data members. This

requirement is a simple acknowledgement that interfaces will change over time and old code should be able to deal with evolving interfaces (a.k.a schema evolution). Advantage of C++ polymorphism for allowing new versions of a class with new functionality added, without destroying the older code, is the key concept of this implementation.

- Interface objects must be keyed. That is, IOs must inherit from PHKey (a key class). Interface object containers are ordered associative containers, that is they provide a mapping from key to object and the ordering of the objects in an IOC is determined by the ordering of their keys. In addition, this mapping is essential for providing associations between objects. For example, an association between object A and objects B, C and D is maintained by A holding the ordered keys for objects B, C and D. Association is simple enough

  PHKey::associate(A, B);

  A TMutCluster object of a cluster will hold the keys for its associated TMutHit objects which form that cluster. Getting back the ordered associated hits for a cluster

  $cluster\_pointer \rightarrow get() \rightarrow get\_associated\langle TMutHit \rangle();$

- IOC data members that access IOs through an index or multiple indices must be bounds checked and throw a standard C++ exception in the case that those bounds are not respected. In analogy to C-style arrays, the objects in an array can be accessed sequentially by array pointers. The fundamental source of access violations in C-style arrays is that user happily keeps ptr++'ing beyond the bounds of the array since the pointer itself (nor the array for that matter) has any notion of how long it is. A basic feature of IOCs is that they offer access via bounded iterators.

- IOCs have clearly defined ownership semantics for the objects they contain. This is implemented with boost smart pointers. Shared or reference countered pointers keep track of the number of outstanding pointers to the object they hold. When the reference count drops to zero they deallocate resources associated with the object.

- Iterators used in MUTOO framework also differ from usual standard library iterators,

because MUTOO iterators are bounded. Advancing an iterator beyond the end of its valid range is protected via an exception through a DEBUG code.

The final layer of the architecture is the analysis modules which interact with the aforementioned IOs and performs the core analysis task. Each analysis has an analysis module interface (AMI) specification that indicates which objects to interact with. The last layer of the architecture is the Subsysreco interface, (sometimes called "super-modules") which is a fun4all framework interface used for regular analysis at PHENIX.

4.1   Muon Software Algorithm

The MuTr analysis software (MUTOO) is designed to reconstruct charged tracks in the muon spectrometer via the particles momentum at the primary vertex. Signals from the MuID detector can either be used to seed the reconstruction in MuTr or can be associated after MuTr reconstruction. A valid muon candidate consists of a combination of a MuTr track and an associated MuID road. The Muon Tracker Analysis can be categorize into four levels:

- Generating coordinates from a particular detector from raw detector signals.

- Pattern recognition or association of coordinates to form track coordinates.

- Momentum and vertex reconstruction.

- Simulation and evaluation modules to test algorithms.

Table 4.1 lists all interface objects which were used during the analysis. This super module calls various modules including mMutFindTrack, where the actual pattern recognition has been implemented. The steps for reconstructing a track is follows:

1. **MUID roads:** Track reconstruction at muon arms begins with reconstructing MuID roads. The MuID is used for triggering muons in the muon arm and occupancy is lower. First, adjacent hit Iarocci two-packs are combined into clusters. 2D tracks are formed

Table 4.1:   Interface objects implemented in MUTOO software framework

Class	Purpose
TMutHit	calibrated and uncalibrated cathode hit information
TMutClus	contiguous groups of active cathodes
TMutCoord	directed line segments representing a fit to cathode clusters
TMutGapCoord	spacepoint formed from two TMutCoord w/ common gap
TMutStub	linear tracklet made from hits in single station
TMutTrk	muon track
TMutVtx	dimuon object
TMCPrimary	parent Monte Carlo particle
TMutMCTrk	Monte Carlo track object
TMutMCHit	Monte Carlo hit object
TMutEval	evaluation object

by progressing backwards toward the event vertex in the x-z and y-z planes using vertically and horizontally oriented two-packs. These 2D tracks are then combined into three dimensional tracks and fitted with a straight line, since there is no magnetic field in the MuID.

2. **MuTr tracks-lets:** In the MuTr, adjacent hit strips are first combined into clusters. Strip charge distributions inside a cluster are fitted with a Mathieson distribution to extract the cluster centroid. Cluster centroids from different cathode planes are then combined into a "gap coordinate"(x,y) since the planes are of different angles. Finally, a linear track-let is formed within a station by combining three gap coordinates with a linear fit. These track-lets are called "stubs".

3. **Seed Tracks from MuID:** Seeding tracks from the MuID is optional. Sometimes MuID roads are matched after MuTr tracks were reconstructed independently. Reconstructed roads in the MuID are used to define windows in station three of the MuTr. Stubs which fall within these windows are used to define track seeds. A stub is a track segment in a given station and represented by the interface object TMutStub. The code assigns a maximum of one track associated with each station three stub. One track can be associated with multiple MuID roads, which falls within the proximity window.

4. **Fit Stubs:** A track candidate (TMutTrk object) formed, that associates station three TMutStub and one or more TMuiRoadO. The stub finder algorithm executes a simple linear fit to gap coordinates if the number of accumulated coordinates are sufficient to constrain the fit. The module mMutStubFit executes the fit to projections using a linear track model and GSL based minimization, including proper error propagation and coordinate weighting.

5. **Find and Associate stubs in Station Two:** Existing track candidates are then used to define search windows in station two of the MuTr. The stub finder algorithm again defines a window for each track candidate. If a stubs was found and it pass a set

of minimal quality cuts, the code tries to associate each stub with a track candidate. If more than one stub found in that given window, a new track is added by cloning the original one.

6. **Bending Plane Fit:** The module mMutBPFit executes a two or three station bend plane fit depending on the number of stubs associated with the track. A straight line fit will not work since the tracks bends due the magnetic field in MuTr. This module uses a parametric track model with one or two effective bend planes to constrain the track parameters. The momentum resolution one can achieve is on the order of 10-20% and execution is very fast. This bent track then used to define windows in station one.

7. **Stubs in Station One:** This is the same as station two, except the window is now defined by the bent track for more accurate projection to station one, where occupancy is highest.

Fully reconstructed tracks in a single event are shown in Fig. 4.1. It is necessary to mention that tracks are reconstructed independently in the two arms, North and South. Some of these tracks which share the same clusters in the MuTr called "ghost tracks". To eliminate them, a bend-plane fit is performed again including station one and tracks which share common clusters are compared. Only tracks with lower χ^2/ndf and more hits are kept; others are rejected (or flagged as ghost tracks). At this point, the muon arm reconstruction is complete and reconstructed tracks can be used for physics analysis.
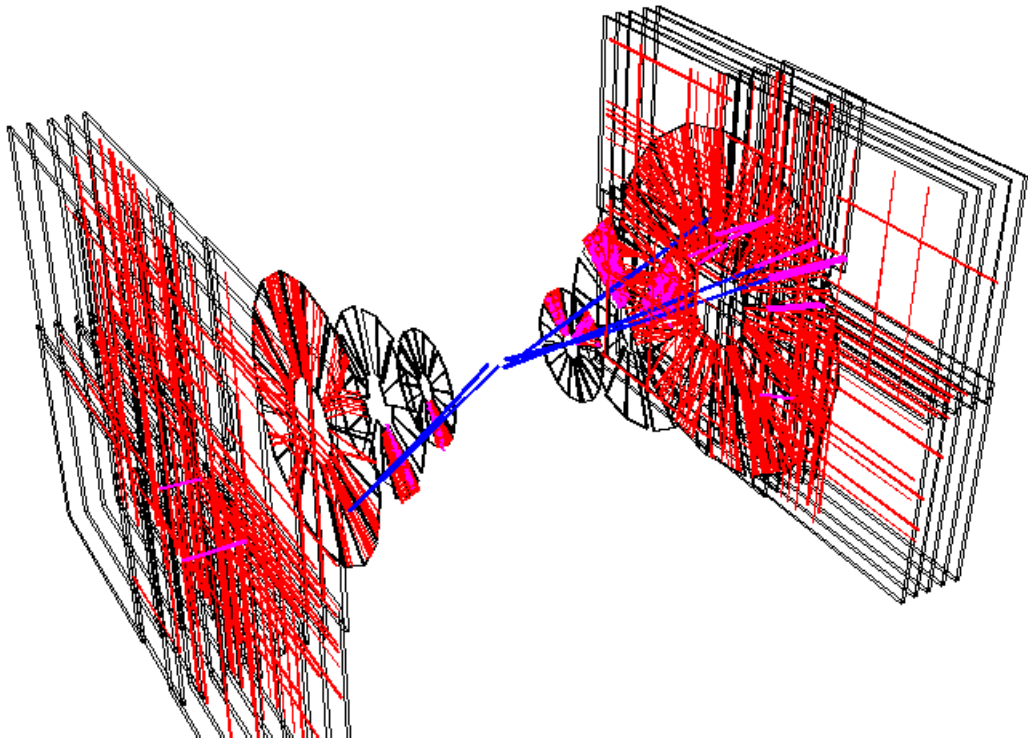
Figure 4.1: Event display showing track reconstruction in PHENIX muon arm.

CHAPTER 5

DATA ANALYSIS

This analysis used data taken by PHENIX during the RHIC Run-10 period (in 2010). The data collected at 39 and 62.4 GeV Au+Au collisions provides an opportunity to study the J/ψ production as a function of collision energy with the PHENIX forward muon arms. The details of the analysis are discussed in this chapter.

5.1 Au+Au Collisions At $\sqrt{s} = 39$ and 62.4 GeV

The 2010 RHIC run was devoted to the heavy ion program. The RHIC beam energy scan program started in 2010. During this run PHENIX recorded a massive amount of heavy ion data covering a wide range of collision energies. During this period, Au+Au collisions at $\sqrt{s} = 200$, 62.4, 39 and 7.7 GeV were recorded with the PHENIX detectors. The total number of minimum bias events collected was 8.2 billion, 700 million, 250 million and 1.5 million at $\sqrt{s} = 200$, 62.4, 39 and 7.7 GeV respectively with z-vertex ± 30 cm. Unfortunately the muon arms were switched off during the 7.7 GeV running because of such a low energy the rapidity shape of the particle production gets so narrow that we don't expect any hits in the forward muon spectrometer. The Au+Au minimum Bias (MB) trigger is defined by

$$\text{Minimum Bias} \equiv \text{``BBCLL1}(>0 \text{ tubes})\text{'' or ``BBCLL1}(>0 \text{ tubes}) \text{ novertex''} \tag{5.1}$$

where "BBCLL1(>0 tubes)" means that at-least one hit is required on each BBC and the z-vertex position is calculated from the timing difference between the North and South BBCs. A valid trigger requires the z-vertex to be $|z_{BBCLL1}| < 37.5$ cm. "BBCLL1(>0 tubes) novertex" is defined in a similar manner but there is no requirement on the z-vertex distribution. The events used in this analysis are from the BBC minimum bias trigger with a cut on BBC $|Z_{vertex}| < 30$ cm applied to ensure high quality data. Fig. 5.1 and Fig. 5.2
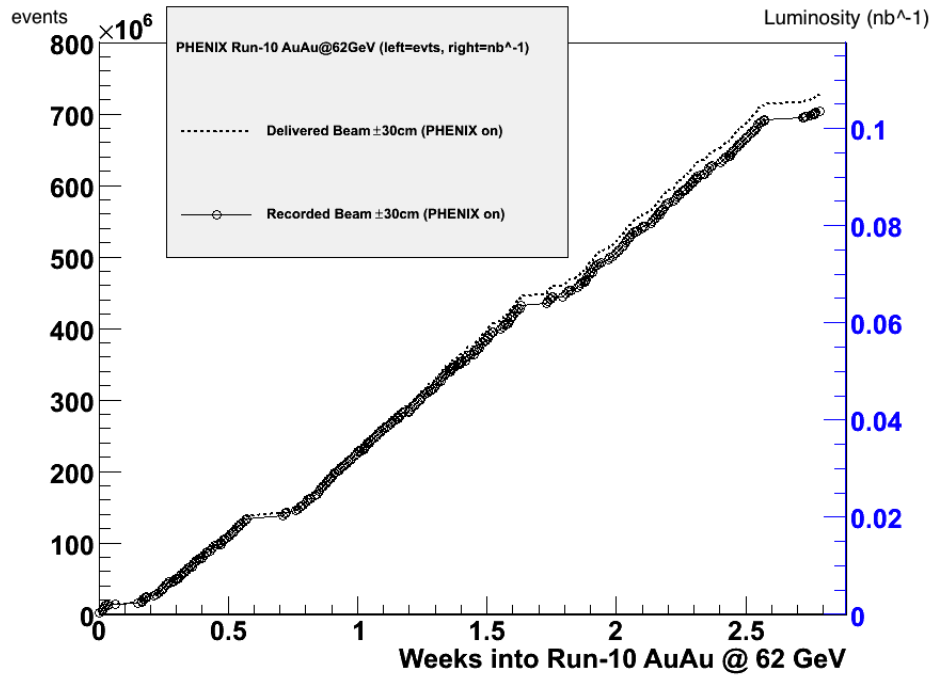
Figure 5.1: Run10 62.4 GeV Au+Au data taking.

show the performance of the PHENIX data taking during the Run10 period. The y-axis shows both accumulated events delivered by RHIC and those recorded by PHENIX as a function of time. Table. 5.1 details the time period, run-range and muon arm magnet (MM) configurations.

Table 5.1: 39 and 62.4 GeV Au+Au collisions.

$\sqrt{s}$	Run-range	Time-period	Magnet polarity
39 GeV	313472-314994	March 19th - April 8th	MM+-
62.4 GeV	310656-313322	April 9th - April 22nd	MM+-
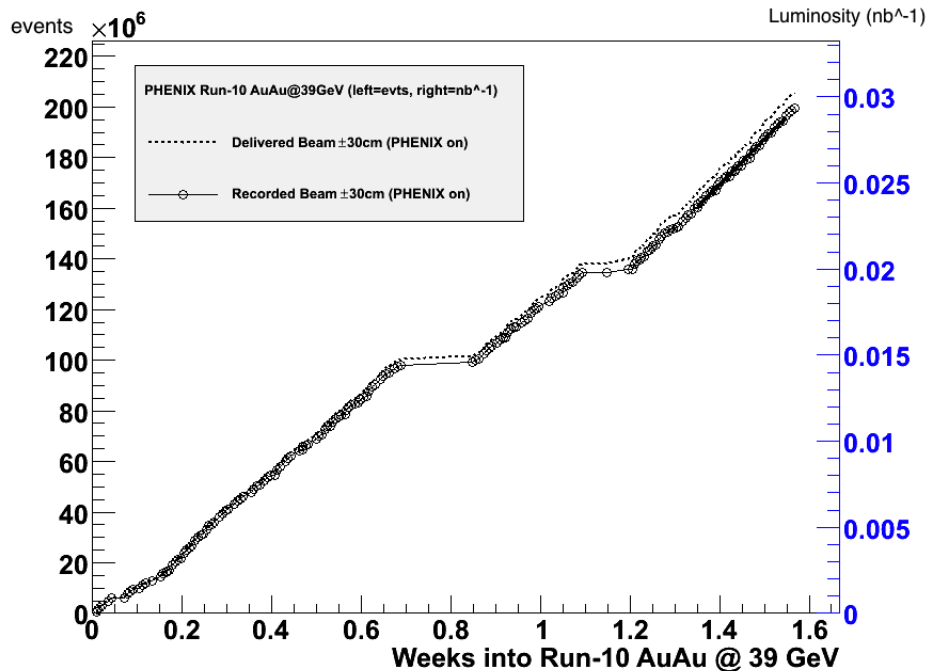
Figure 5.2: Run10 39 GeV Au+Au data taking.

5.2 Collision Centrality

Before any physics analysis can be performed, the global event properties of the events must be analyzed from raw data. Centrality corresponds to the measured fraction of the total inelastic cross section of Au+Au collisions, which is directly related to the impact parameter of two colliding nuclei, as well as the number participating nucleons (N_{part}) and the number of nucleon-nucleon collisions (N_{coll}). Centrality ranges from 0% to 100%. Collisions with centrality 0% corresponding to the impact parameter 0, are called "central collisions". "Peripheral collisions" are those when the impact parameter is $\sim 2R$ whose corresponds to $\sim$100% centrality, where R is the radius of the Au nuclei. The total energy measured by the BBC is proportional to the impact parameter of the Au+Au collisions, and is normally used to categorize the events into centrality classes. This procedure was used for categorizing 200 GeV Au+Au events into centrality bins. However, due to the narrow rapidity distribution at low energy Au+Au collisions, the distributions from the BBCs, located at $3.1 < |\eta| < 3.9$

can not be used in the low energy runs.

The shape of the rapidity distribution strongly depends on the energy and centrality as well. Lower energy collisions have a much narrower rapidity distribution than 200 GeV or higher energy collisions. The centrality determination and efficiency estimates for PHENIX low energy Au+Au collisions were made using Pad Chamber (PC) and Reaction Plane detector (RxNP) hit distributions. The rapidity coverage of PC and RxNP are $|\eta| < 0.35$ and $1.0 < |\eta| < 2.8$ respectively. One can assume that two nuclei can collide with any impact parameter with equal probability which corresponds to a flat centrality distribution. So, 0-10% centrality corresponds to the 10% of the collisions with the highest multiplicity.

A Glauber Monte Carlo model simulation was performed to determine an average of the physical variables, the impact parameter b, the number of binary nucleon-nucleon collisions N_{coll}, the number of participants N_{part} and the nuclear overlap function T_{AB} in Au+Au collisions for each centrality category [57]. First a Glauber N_{part} distribution is generated for the relevant beam collision energy. It is assumed that the particle production per event follows a negative binomial distribution.

For each nucleon-nucleon collision a random number of hits (or particles) n_i is simulated from the negative binomial distribution (NBD, characterized by k and μ) for i^{th} participant. Then, the total number of hits from a single binary collision is $N_{hits} = \Sigma_{i=1}^{N_{part}} n_i$. The key is to fit the real data hit distributions from PC and RxNP to that from Glauber simulation to estimate the NBD parameters k and μ by assuming multiplicity for each nucleon-nucleon collision follows some kind of NBD distribution.

$$P_{\mu,k}(n) = \frac{\Gamma(n+k)}{\Gamma(n+1)\Gamma(k)} \frac{(\mu/k)^n}{(\mu/k+1)^{n+k}} \tag{5.2}$$

where μ is the mean number of particles and k is related to the variance $k = \frac{\mu^2}{Var(n)-\mu}$. Assuming that the detector is efficient enough to measure the high possible multiplicity ($\sim 100\%$ efficiency), the MC events are then scaled to fit the actual detector hit distributions. Two NBD fits are shown in Fig. 5.3 and Fig. 5.4 which reproduce the PHENIX PC1 multiplicity
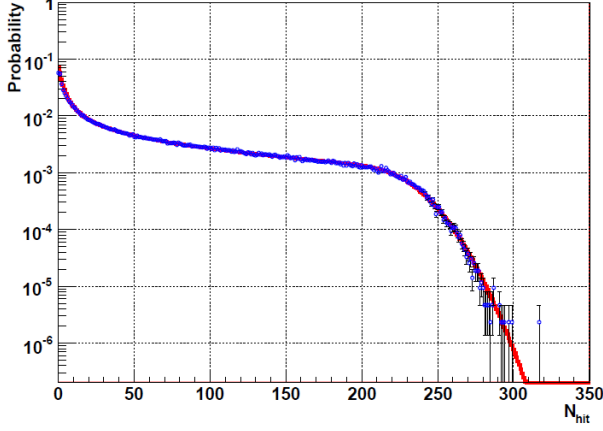
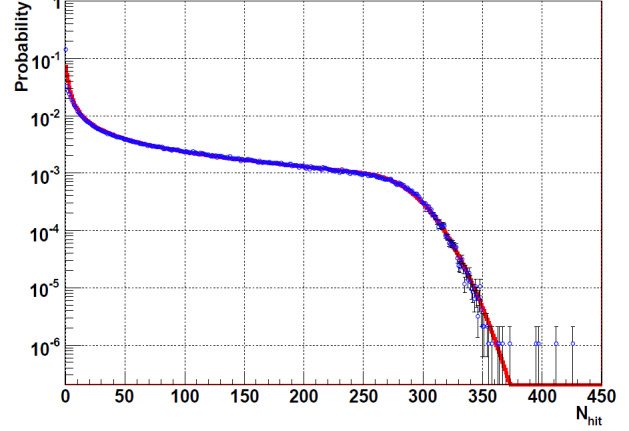Figure 5.3: Glauber NBD fit to PC1 hit distributions at 39 GeV.

Figure 5.4: Glauber NBD fit to PC1 hit distributions at 62.4 GeV.

distribution very well, corresponding to μ=0.578 and k=1.028 for 39 GeV and μ=0.738 and k=1.014 for 62.4 GeV.

After a good fit is obtained, the trigger efficiency is calculated by:

$$\epsilon_{trigger} = \frac{\text{Total Data Events}}{\text{Total MC Events}} \tag{5.3}$$

which is 85.9 $\pm$ 2% for 39 GeV and 85.7 $\pm$ 2% for 62.4 GeV. The Glauber model parameterizations used for this analysis are: Woods-Saxon nuclear radius R=6.45 $\pm$ 0.20 fm, surface thickness a= 0.54 $\pm$ 0.1 fm, and nucleon-nucleon inelastic cross section σ_{NN}=34 $\pm$ 3 mb at 39 GeV and σ_{NN}= 37 $\pm$ 3 mb at 62.4 GeV. Once a sufficiently large number of Glauber-simulated collisions were generated, the Pad Chamber hit distributions were used to divide them into centrality classes. Similarly, RxNP hit distributions were also re-generated using the Glauber simulation and the difference between the results from PC and RxNP is added as a systematic uncertainty. The event distribution is truncated to the total trigger efficiency, which is 86% for our case. Hence, the centrality of each event is in the range 0-86, with 0 being the most central and 86 for the most peripheral. The mean value for the physical parameters were then calculated, $\langle b \rangle$, $\langle N_{part} \rangle$, $\langle N_{coll} \rangle$ and $\langle T_{AB} \rangle$ for each centrality class. The

systematic uncertainties associated with these quantities were estimated by varying Glauber parameters. The average values of the above quantities are given in Table. 5.2 and Table. 5.3 for 39 and 62.4 GeV Au+Au collisions respectively. Total number of centrality bins are 4 in 62.4 GeV and 2 in 39 GeV. The data from PC or RxNP does allow for finer bins but the J/ψ counts are statistically limited, as discussed in next sections. The centrality bins listed here are according to the J/ψ s bins.

Table 5.2: Glauber results for 39 GeV

Centrality	$< N_{part} >$	$< N_{coll} >$	$\langle b \rangle$	$\langle T_{AB} \rangle$
0 - 40%	204.42 ± 4.42	444.84 ± 50.28	6.14 ± 0.36	13.10 ± 1.56
40 - 86%	34.10 ± 1.64	43.46 ± 3.72	11.56 ± 0.72	1.41 ± 0.23

Table 5.3: Glauber results for 62.4 GeV

Centrality	$< N_{part} >$	$< N_{coll} >$	$\langle b \rangle$	$\langle T_{AB} \rangle$
0 - 20%	274.8 ± 3.84	689.9 ± 78.89	4.41 ± 0.18	18.65 ± 1.62
20 - 40%	138.7 ± 4.646	270.5 ± 27.46	7.96 ± 0.35	7.31 ± 0.58
40 - 60%	59.74 ± 3.893	85.71 ± 9.064	10.36 ± 0.46	2.32 ± 0.22
60 - 86%	14.66 ± 1.238	14.29 ± 1.65	12.89 ± 0.54	0.39 ± 0.05

5.3 Quality Assurance

The main purpose of the analysis is to understand the J/ψ production of 39 and 62.4 GeV center of mass energies in Au+Au collisions using the data taken by PHENIX in 2010. Before measuring any physical quantity, it is important to ensure that the data is of good quality. Hence, a comprehensive quality assurance (QA) analysis of the data is

imperative. Once good runs were sorted successfully, where detector had a stable behavior, the reconstructed J/ψ mesons from those sorted runs were then corrected for the limited muon arm acceptance and detector inefficiencies.

First, the raw data from the forward muon arms were reconstructed by using the pro.85 version of the PHENIX software library with the ROOT software framework. There were a total of 239 and 330 physics DAQ runs recorded with BBC minimum bias trigger at $\sqrt{s}$=39 and 62.4 GeV, respectively. Muon QA files with many low level informations (cluster charge and size, track residuals, etc.) were generated during the data production process, which were then used to exclude runs which significantly deviate from the overall run-by-run average. Checks were performed on both 39 and 62.4 GeV datasets to ensure that any runs collected while the detectors were performing poorly are removed. A uniform performance is needed to make simulations possible to represent the overall quality of the data. These checks include:

- Shift-logs: Initial QA is done by using online monitoring information and shift crew logs to remove the data where significant portions of the detectors were switched off or misbehaving. Generally these runs are rejected by the PHENIX production team and are get produced at all in order to save time.

- MuTr Disabled high voltage channels: Runs were thrown out if a significant portion of the detector was disabled. The number of disabled HV channels was very stable during the Run10 period for the north arm. There are a few runs which have higher number of disabled HV channels for the south arm. Fig. 5.5 shows the run-by-run distribution of the disabled HV channels at 62.4 GeV. There were 50 disabled high voltage channels throughout the run. Any run which has significantly more than 50 disabled channels was thrown out. A similar check was performed for 39 GeV data as well. The final criteria for good runs was established for runs that have less than 120 disabled channels, keeping in mind that the dataset is statistically limited and runs were not thrown away unless it was necessary.

- MuTr Cluster charge: This relates to some of the hardware changes in MuTr which
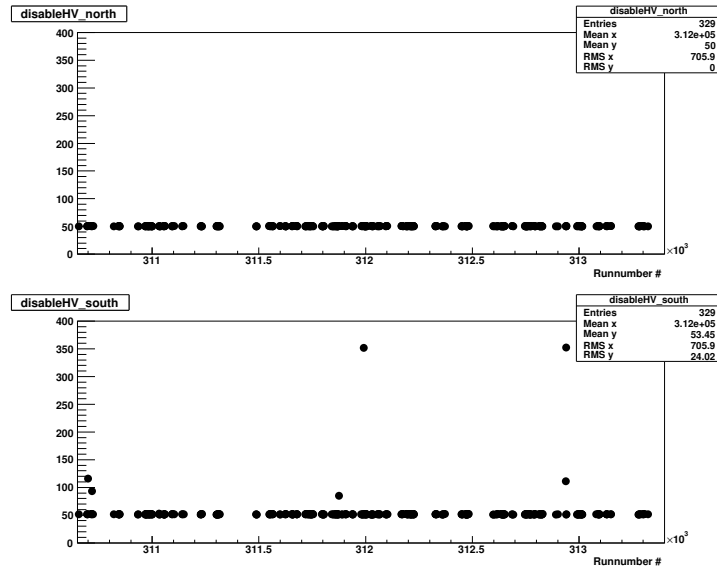
Figure 5.5: Number of disabled high voltage channels in north (top) and south (bottom) arms (62.4 GeV).

occurred before the data taking started in 2010. A large number of capacitors were replaced and the conversion from ADC to charge was revisited. We applied new gain correction factors to determine the strip charge from the raw ADC values. These gain corrections were tuned using $p+p$ data collected in 2009 and then used for Au+Au analysis. The cluster charge distribution was then fitted with a Landau function. The cluster charge distribution for each gap in the south arm from the data and the simulation is shown in ig. 5.6. Runs with very different charge distributions were removed. This was done by looking at the Landau peak and most probable value (MPV). Runs more than one standard deviation away from the mean were removed.

- Number of clusters: Runs that have a deviation of more than two standard deviations from the mean for each of the three stations were rejected. Table 5.4 shows the mean and standard deviations of the clusters for the south and north arms. A large deviation of the mean values indicates a very noisy channel which could lead to large number of fake tracks.
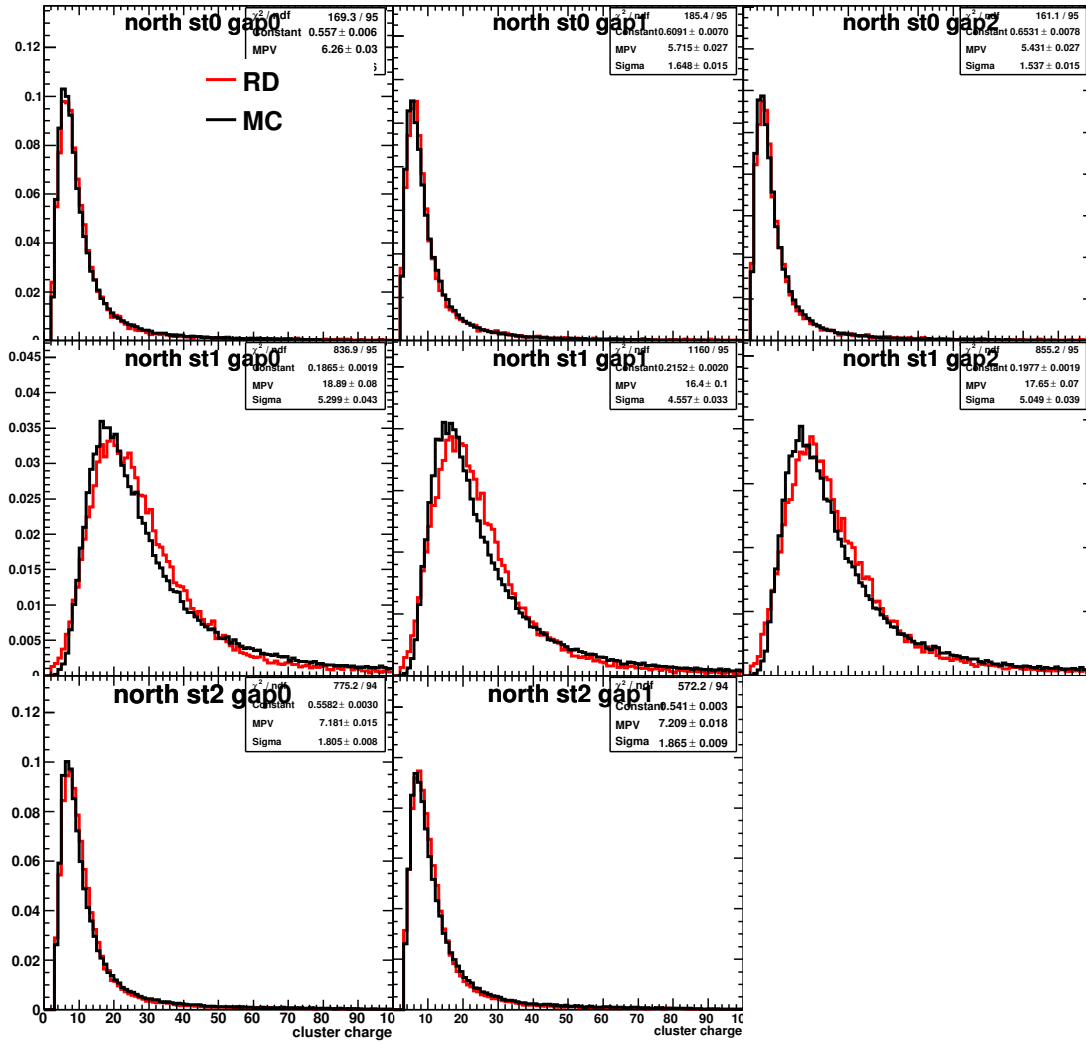
Figure 5.6: Landau fit results of the cluster charge distribution from the south arm as a function of run number (62.4 GeV).

Table 5.4: The mean and standard deviation of the number of clusters in each station.

$\sqrt{s}$	Stations	South	North
62.4 GeV	1	3.48 ± 0.30	5.30 ± 0.59
	2	3.70 ± 0.29	6.32 ± 0.57
	3	6.41 ± 0.27	11.78 ± 0.37
39 GeV	1	2.84 ± 0.32	4.58 ± 0.60
	2	2.88 ± 0.29	5.05 ± 0.62
	3	5.10 ± 0.21	9.30 ± 0.44

- Hot/Dead planes and packets: Hot planes are defined as plane hits more than one standard deviation away from the mean and dead planes have no hits. Hot packets are defined as packet hits more than 2 standard deviations away from the mean and dead packets have no hits. Two runs with dead planes were found in the north arm for 62.4 GeV and were discarded.

After the runs with the above criteria are removed, the remaining runs should have fairly uniform detector performance. More details about the runs that were thrown out are listed in Appendix B. The total number of good quality runs is 322 from the South Arm and 321 form the North Arm at 62.4 GeV after the QA analysis. No runs were rejected from the 39 GeV dataset due to the uniform detector performance during that short time period. The total number of good runs of 39 GeV is 239.
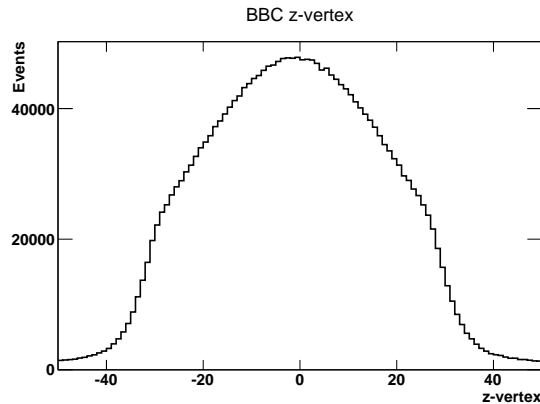
BBC z-vertex

Figure 5.7: BBC z-vertex distribution at 62.4 GeV Au+Au collisions.

5.4 Data Quality Cuts

Once QA is done and a "good runlist" is prepared for each arm, additional cuts are applied at the analysis software level to improve the quality of the data. The algorithm for finding a muon track and reconstructing a dimuon out of two single muons is detailed in Chapter 4. These cuts are called analysis cuts and implemented at various stages of the analysis, e.g. event-level, track-level and pair-level. Monte Carlo simulations were used to optimize these cuts to achieve a reasonable background rejection and signal extraction.

Event z-vertex

The event vertex is measured by the BBC. z-vertex distributions are typically a Gaussian like distribution. Only events that fall within ± 30 cm were considered. Fig. 5.7 shows the BBC vertex distributions in 62.4 GeV Au+Au collisions. A cut at ±30 cm will reject ∼14% of the events.

MuTr and MuID matching

Tracking algorithms find the tracks and roads inside MuTr and MuID. MuTr tracks were then matched with MuID roads within an event to confirm a valid muon candidate. This has been done by projecting MuTr tracks on the first plane of MuID and defining a window for a valid association. In low-occupancy collisions such $p+p$ this is sufficient but in Au+Au

collisions the multiplicity is much higher and such associations are much harder. A DG0 cut is defined as the distance between the reconstructed track in MuTr station 3 extrapolated to the first plane of the MuID and the position of its best associated road is within this range. The DDG0 cut is defined as the angle difference between the tangent of the track and road angles with respect to the beam axis. Corresponding values are listed in Table. 5.5.

Tracks reconstructed in MuTr

For a muon to pass through 140 cm of steel and 20 cm of brass in the initial absorber and to be able to penetrate to the last gap of the MuID it must have a minimum p_z. The minimum value was estimated from simulations, in which muons must have that much p_z to be able to penetrate the front absorber. Muon candidates that do not pass the minimum p_z cut are most likely come from noise and were rejected.

Tracks in the MuTr are reconstructed through a fit to the MuTr hit positions called a Kaplan fit. This fit takes care of the track bending in the magnetic field and estimates the particle's momentum. A χ^2/ndf cut is applied to ensured the quality of the fit. An estimate of a good χ^2/ndf from the simulated tracks was applied to the data in order to reject false tracks which occur due to misfiring in the detector.

Pair selection

Finally dimuons are reconstructed from two single muon tracks and event vertex information from BBC. A dimuon is selected such that the two participating single muons should be separated enough to rule out any overlap or occupancy issues. In the MuTr, we ensure that pair tracks do not share the same octant. This is called an octant cut. For the MuID, an isolation cut is used to ensure pair roads either do not share same the MuID panel or are separated by 100 cm in the x-y plane. These separation cuts are not much effective for tracks within a single event. However, this is an important cut to be able to perform event-mixing technique which is used for estimating background combinatorial pairs from different events without any overlaps. Finally, two muon vertices along with the BBC z-vertex were fitted to calculate the dimuon vertex. A dimuon vertex χ^2/ndf cut was applied to select good dimuon

pairs. Table 5.5 lists all the cuts that were used in this analysis.

Table 5.5: Analysis cuts applied for J/ψ signal extraction.

Cut-type	Cuts
Event	$|z_{BBC}| <$30 cm
Track	MuID last gap Hit
	MuTr Hit > 8
	DG0$<$20(15) in South(North) Arm.
	DDG0 < 9
	MuTr χ^2/ndf < 20 (30) for South (North) arm
	$P_z >$1.05(1.17)GeV/c for South(North) arm
Pair	$1.2 < |y| <$2.2
	Octant Cut
	MuID Isolation Cut
	Vtx $\chi^2 <$4

5.5   Signal Extraction

The J/ψ signal was extracted from the dimuon invariant mass spectrum through component analysis. First a dimuon invariant mass spectrum was constructed from single muons for each p_T, rapidity and centrality bin. The dimuon invariant mass $(M_{\mu^+\mu^-})$, is calculated using the following equation:

$$M_{\mu^+\mu^-} = \sqrt{(E_{\mu^+} + E_{\mu^-})^2 - (|\vec{p}_{\mu^+}| + |\vec{p}_{\mu^-}|)^2} \qquad (5.4)$$

where E_{μ^+} and E_{μ^-} are the total energies of the two muons while $\vec{p}_{\mu^+}$ and $\vec{p}_{\mu^-}$ are their momenta.

Fig. 5.8 shows the raw dimuon invariant mass spectra (solid blue) for the 62.4 GeV Au+Au collisions in the south arm. The raw dimuon spectra contains dimuons from all possible physics processes as well as a lot of background tracks. The source of these background pairs can be categorized into 2 groups. The unphysical backgrounds are due to mis-fire in the MuTr cathode strips (noise) which generates ghost-tracks and fake-tracks. Ghost tracks are removed by requiring a hit not to be share by multiple tracks. Only the track with lowest χ^2/ndf is kept. The background is estimated using two methods: event-mixing technique and likesign technique. The background subtracted spectra is assumed to have dimuons from hard processes only. This spectra will still have the physical background in addition to the J/ψ s which includes contributions from other physics processes, like charm, bottom and DY pairs. Finally a peak at dimuon mass 3.1 GeV will confirm a successful J/ψ reconstruction. The details of the background subtraction techniques are discussed next.

Background evaluation

To calculate the number of J/ψ candidates, it is very important to subtract the background in the dimuon invariant mass spectrum. Sources of background and evaluation techniques are as follows:

- Uncorrelated pairs (combinatorial background) are those pairs where two muons are from different sources and independent of each other. This background becomes very significant in higher multiplicity environment like Au+Au collisions. Combinatorial background is estimated through event mixing method.

- Dimuons generated by physics processes other than J/ψ decay are also considered as background. Correlated pairs are those which come from open charm ($D\bar{D}$), open bottom ($B\bar{B}$) and Drell-Yan production (together they are called continuum). This type of physics background exists under the J/ψ mass peak and can not be removed by the event mixing method. After the subtraction of the combinatorial background,

contamination from the correlated background is estimated through an exponential fit to the mass range above and below the J/ψ mass range where no other resonance is expected.

Event-mixing background is used to account for the uncorrelated cominatorial background. Standard PHENIX event-mixing software used with muon-specific module which contains all event and track-level cuts are used to estimate the background. In this technique, muons from one event are combined with muons from a pool of previous events to estimate the background. A pool of 10 events was stored at a time and muons from same centrality (10% wide), z-vertex (2 cm wide) are then combined with each other to form two-track random combinations. For example, one muon from an event and another muon from a different event in the event buffer with identical centrality and vertex bin, produces an uncorrelated $\mu^+\mu^-$ pair. The dimuon histograms from event mixing will not have any resonance peak, since no mixed pair comes from J/ψ decay. In this technique 2×10 (number of pool depth) mixed events were produced for every event. Hence, it is necessary to introduce a normalization factor to scale the mixed background to the foreground (pairs from the same event) level. This normalization is not straight-forward because of the detector resolution and event fluctuations. The normalization of the mixed pairs is estimated by,

$$BG^{mixed}_{+-} = BG_{+-} \frac{\sqrt{FG_{++}FG_{--}}}{\sqrt{BG_{++}BG_{--}}} \tag{5.5}$$

Where FG stands for foreground pairs within the same event and BG are the background pairs from mixed pairs between events. $++,--$ and $+-$ are the $\mu^+\mu^+$, $\mu^-\mu^-$ and $\mu^+\mu^-$ pairs. The remaining unlike-sign dimuon signal after the mixed background subtraction are:

$$N_{+-} = FG_{+-} - BG^{mixed}_{+-} \tag{5.6}$$

Fig. 5.8 shows both the foreground and normalized background unlike sign dimuon pairs (FG_{+-} and BG^{mixed}_{+-}) between 1.8-5 GeV dimuon mass at 62.4 GeV Au+Au collisions. The small bump around ~ 3.1 GeV is the J/ψ signal.
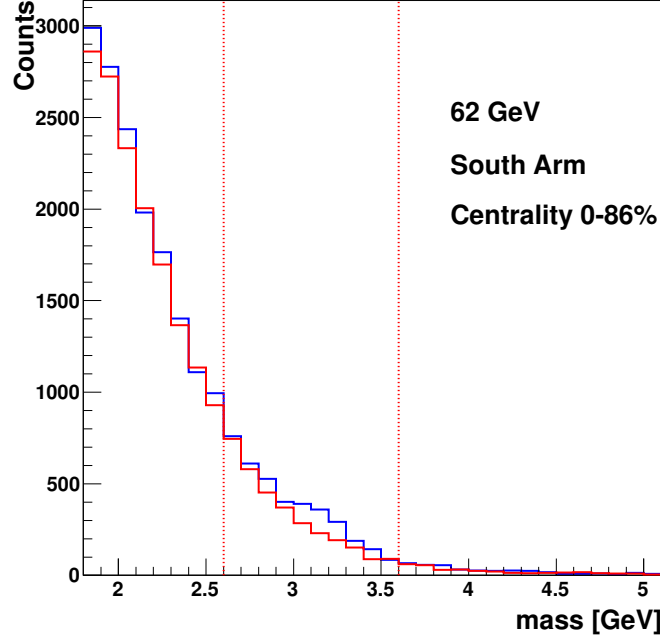
Figure 5.8: Raw dimuon counts for unlike-sign (solid-blue) and like-sign (solid-red) pairs.

One way to test the performance of the event mixing technique and its proper normalization is through like-sign pairs. Like-sign pairs are mostly combinatoric, so when we subtract $++$ and $--$ foreground pair histograms from the normalized mixed like-sign background, one should not see any dimuon signal at all. Fig. 5.9 shows the 62.4 GeV background subtracted like-sign dimuon spectra which is almost flat in the J/ψ mass region [2.6-3.6 GeV]. It can be seen that the fluctuations in the combinatoric background is higher for the mass range below J/ψ, resulting a fluctuations around ~ 2 GeV in the mixed background subtracted likesign signals. This corresponds to our poor understanding of the background at this region.

In the **Like-sign** background technique, it is assumed that the like-sign pairs within an event are purely from combinatoric background. The like-sign background is estimated by:

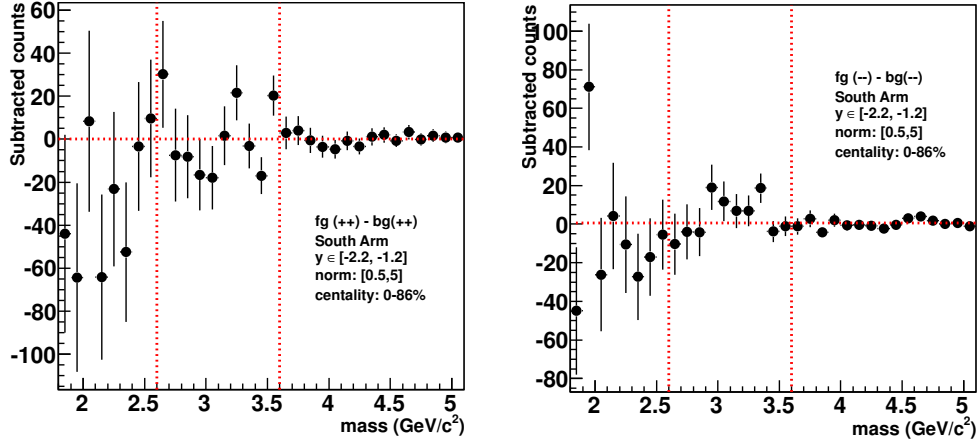$$FG_{\pm}^{like} = 2R\sqrt{FG_{++}FG_{--}} \qquad (5.7)$$

Figure 5.9: A successful background subtraction by event mixing for like-sign pairs.

where FG stands for the foreground pairs, corresponding to the pairs that are formed within the same event. R accounts for possible asymmetry in the positive and negative muon production and/or asymmetry due to detector trigger or acceptance bias relative to positively and negatively charged muons. For this analysis R=1 is used, since no charge asymmetry in positive and negative muons was found. This background subtraction technique has the disadvantage that the statistics of the background spectrum is limited to the number of available events. On the other hand, since unlike-sign and like-sign pairs are calculated within the same events, the background normalization is very straightforward. The unlike-sign dimuon mass spectra after like-sign subtraction is:

$$N_{+-} = FG_{+-} - FG_{\pm}^{like} \tag{5.8}$$

It is worthwhile to mention that all likesign pairs are not combinatorial pairs. Decay products of charm and bottom products contains like-sign correlated pairs. So the like-sign technique is not applicable for charm and bottom decay analysis. However, since the yield of unlike-sign dimuons from J/ψ decay is larger than the continuum yield, both event-mixing and likesign technique should yield the same result.

5.6 Invariant Mass Fit Function

The background subtracted total dimuon yield is then fitted in order to extract the J/ψ contribution to the unlike-sign dimuon spectra. An acceptance weighted triple-gaussian-exponential fit function is used to extract J/ψ signal counts from the dimuon invariant mass distribution. The fit function is the following

$$
fit\_func = P_0 \left[\frac{(1-P_3)}{P_2\sqrt{2\pi}} exp(-\frac{1}{2}\frac{(x-P_1)^2}{P_2^2}) + \frac{P_3}{P_4\sqrt{2\pi}} exp(-\frac{1}{2}\frac{(x-P_1-P_7)^2}{P_4^2}) \right] +
$$
$$
P_5 exp(-\frac{x}{P_6}) + \frac{P_8}{P_{10}\sqrt{2\pi}} exp(-\frac{1}{2}\frac{(x-P_9)^2}{P_{10}^2}) \tag{5.9}
$$

This fit function is chosen based on previous PHENIX muon arm analyses [71]. The J/ψ shape is better described with two Gaussians, corresponding to the first two terms in Eq. 5.9, one for the J/ψ peak and a second one with higher sigma to account for the fat tail, which occurs due to limitations in MuTr resolution. The two Gaussians are normalized to 1, P_3 being the ratio of the two gaussians. An exponential is used to account for the continuum contributions from open charm, open bottom and DY which is the third term in Eq. 5.9. The values used for the parameters in Eq. 5.9 are listed in Table 5.6. Parameters for two Gaussian and the exponential parameters were tuned with PHENIX $p+p$ measurements and were used in Au+Au spectra. The last term is an additional Gaussian for the low mass, to account for the low mass vector mesons (ρ, ϕ and ω) resonances. The purpose for this extra Gaussian for the low mass is to constrain the exponential fit for the continuum, otherwise, due to a significant amount of distortion in between mass range 1-2.5 GeV there will be a higher systematic error. Fig.5.10 shows the dimuon mass spectra at 62.4 GeV along-with different fit components: red is the total fit, black for two gaussian components in J/ψ mass region, green for the low mass gaussian and blue for the exponential fit.

It is important to note that the fit function also includes the dimuon mass acceptance. The total fit function is convoluted with a function representing the acceptance as a function

Table 5.6: Fitting parameters for J/ψ signal extraction.

Parameter	Description	Values & Limits
P_0	Total Gaussian Integral	[0, 1e6]
P_1	Gaussian Mean	[0.97, 1.03] $\times M_{J/\psi}$
P_2	1st Gaussian sigma	South: $0.130+ <p_T> \times 0.010$ North: $0.138+ <p_T> \times 0.004$
P_3	Two Gaussian Fraction	0.394 (South), 0.397 (North)
P_4	2nd Gaussian Sigma	South: $0.314+ <p_T> \times 0.091$ North: $0.392+ <p_T> \times 0.030$
P_5	Exponential Normal	[0, 1e9]
P_6	Exponential Slope	[0, 25.0]
P_7	2nd Gaussian Mean Shift	0
P_8	Lower Mass Gaussian Integral	[0, 1e9]
P_9	Low Mass Gaussian Peak	[0.4, 1.1]
P_{10}	Low Mass Gaussian Sigma	[0.1, 0.25]

of mass. It was found from simulations that the dimuon mass acceptance is not uniform over all mass regions. Due to the absorber, the acceptance for the low mass vector mesons are very much reduced and no low-mass peaks found for $p_T < 1$ GeV/c. Since acceptance varies among different kinematic bins, the simulated the muon arm acceptance at all kinematic bins and folded accordingly with the fit function in order to achieve a better χ^2. This is described in detail in Section 5.7.2. It should also be noted that the shape in Au+Au collision is not known properly due to higher background. Some of the fit parameters were then varied by some amount to account for the relative fluctuations in J/ψ counts and accounted for systematic errors. This part is discussed in Section 6. Fig. 5.11 shows the estimated background from event mixing technique and foreground unlike-sign pairs as well
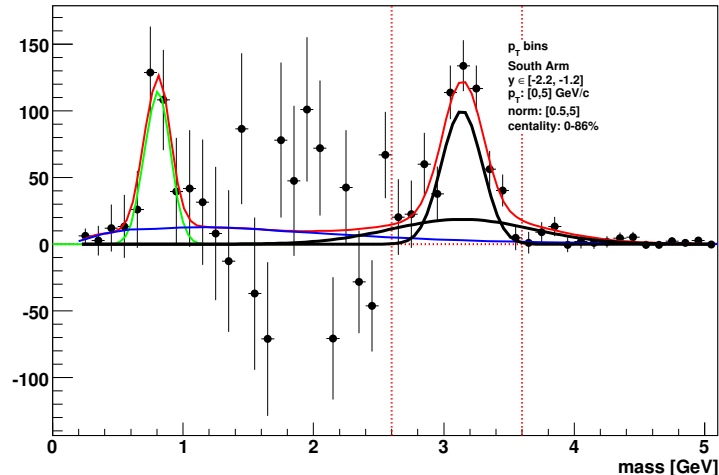
Figure 5.10: 62.4 GeV dimuon spectrum in south arm for p_T [0-5] GeV/c for all centrality. red is the total fit, black for two gaussian components in J/ψ mass region, green for the low mass gaussian and blue for the exponential fit.

as the background subtracted unlike sign dimuon mass spectra for 62.4 GeV (top two panels) and 39 GeV (bottom two panels) Au+Au collisions. This data corresponds to all kinematic bins inclusive of both muon arms.

5.6.1 62.4 GeV J/ψ Yields

In this section, the J/ψ signal counts in each centrality and p_T bins are discussed. The results are given in Tables 5.7 and 5.8. Due to limited statistics, only 4 centrality and 4 p_T bins were made. The background subtracted unlike-sign dimuon spectra were fitted in each kinematic bin independently for each arm in order to extract J/ψ counts. The dimuon spectra and fits for all kinematic bins are shown in Appendix C. Since this is a symmetric collision, a weighted average of the two arm counts was later considered towards the final counts in each kinematic bin. The final signal value given for each kinematic bin is listed in Tables 5.7, 5.8, which also include their RMS as point-to-point uncorrelated systematic errors. The signals are extracted using the background subtraction techniques, event-mixing and like-sign and averaged. Any disagreement in signal extraction by the two methods are considered as a systematic uncertainty, since we don't know which one is more
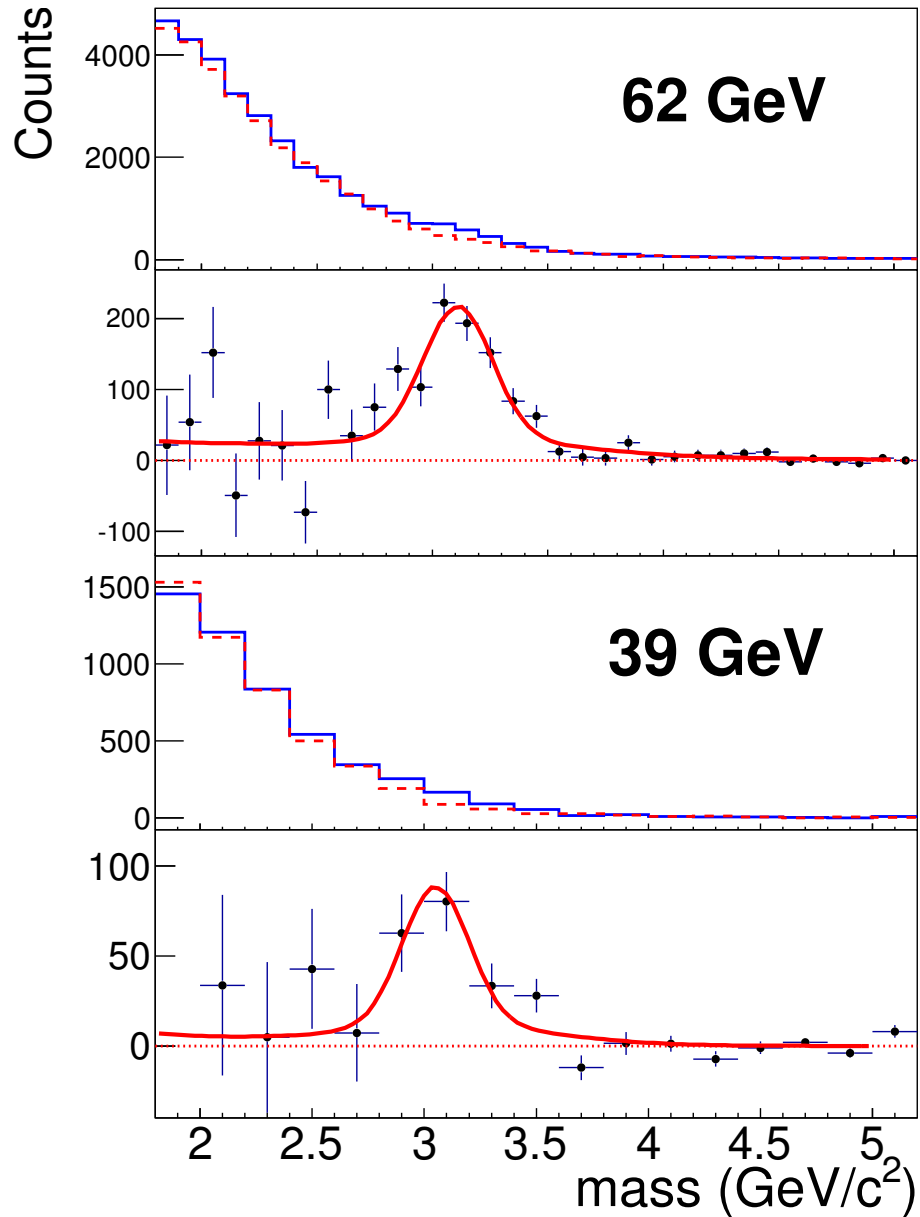
Figure 5.11: The unlike sign invariant mass distribution (blue) for all Au+Au centralities and both muon arms is shown along with the uncorrelated background calculation from mixed event pairs (red) for 62.4 GeV (top two panels) and 39 GeV (bottom two panels). The lower panel in each pair shows the subtracted distribution and a fit to the data.

correct. Signals from two methods were included while taking their RMS for point-to-point uncorrelated systematic errors. The counts presented in Table 5.7, 5.8 are in format of $yy \pm xx \pm zz$ (counts $\pm$ statistical error $\pm$ systematic error). There are additional systematic errors on the yields which are not discussed here. More details of the systematic errors are described in Chapter 6.

Table 5.7: Raw J/ψ counts from the 62.4 GeV data with associated statistical and uncorrelated systematic errors in each centrality bin.

Centrality	South Arm	North Arm
[0, 20]	$338.95 \pm 52.29 \pm 6.51$	$211.127 \pm 50.80 \pm 3.88$
[20, 40]	$179.04 \pm 29.79 \pm 7.25$	$133.16 \pm 23.19 \pm 2.44$
[40, 60]	$68.70 \pm 12.41 \pm 3.30$	$70.91 \pm 13.23 \pm 0.99$
[60, 86]	$29.67 \pm 5.79 \pm 0.39$	$34.24 \pm 6.45 \pm 0.48$

Table 5.8: Raw J/ψ counts from the 62.4 GeV data with the associated statistical and uncorrelated systematic errors in each p_T bin.

p_T	South Arm	North Arm
[0, 1]	$216.47 \pm 38.88 \pm 4.64$	$134.12 \pm 36.35 \pm 7.09$
[1, 2]	$205.97 \pm 38.83 \pm 5.59$	$195.88 \pm 36.52 \pm 4.27$
[2, 3]	$112.85 \pm 25.33 \pm 1.95$	$76.09 \pm 21.45 \pm 2.72$
[3, 5]	$34.06 \pm 12.79 \pm 2.53$	$19.04 \pm 14.17 \pm 1.82$

5.6.2 39 GeV J/ψ Yields

The signal extraction scheme for 39 GeV case is different in comparison to the 62.4 GeV data set due to very low statistics. We computed the J/ψ yield by integrating the mass range of [2.6 - 3.6] GeV assuming there is no background. The average counts of two background subtraction methods is used for the final yield while their difference is considered as a systematic error. The dimuon spectra was not fitted with any function because, with such low statistics, fits will not be optimized and it is very hard to constrain the fit parameters. In total there are ~ 170 J/ψ counts including both arms. Raw J/ψ counts are listed in Table 5.9 and 5.10. Because of the low statistics, we only made two centrality bins (inclusive of p_T) and three p_T bins (integrated over all centrality) while extracting the total yield. An additional 15% systematic error was assigned due to integrated signal extraction.

Table 5.9: Raw 39GeV J/ψ counts followed by statistical and uncorrelated systematic error as a function of centrality.

Centrality	South Arm	North Arm
[0, 40]	$86.7084 \pm 30.9075 \pm 2.53675$	$63.8019 \pm 24.9431 \pm 2.91848$
[40, 86]	$19.2034 \pm 6.69027 \pm 0.7294$	$10.1422 \pm 5.08503 \pm 0.0440257$

5.7 Acceptance and Efficiency

Raw J/ψ counts are further corrected by acceptance×efficiency corrections in order to properly account for the detector geometric acceptance and efficiencies. Once the inefficiencies due to the detector bias is well accounted for, physical quantities can be calculated. First the detector efficiencies are estimated and folded into the reconstruction code, which then we use to reconstruct simulated J/ψs from different particle generators. In this way, a

Table 5.10: Raw J/ψ counts from the 39 GeV data with the associated statistical and uncorrelated systematic errors in each p_T bin.

p_T	South Arm	North Arm
[0, 1]	$66.7 \pm 21.2 \pm 3.08$	$28.6 \pm 16.2 \pm 2.09$
[1, 2]	$25.8 \pm 20.1 \pm 1.36$	$28.7 \pm 16.2 \pm 1.41$
[2, 5]	$13.6 \pm 11.8 \pm 0.89$	$18.6 \pm 10.4 \pm 3.32$

single factor for overall acceptance×efficiency of the detector is determined.

$$\epsilon^{acc \times eff}(y, p_T) = \frac{\text{Number of } J/\psi \text{ reconstructed } (y, p_T)}{\text{Number of } J/\psi \text{ generated } (y, p_T)} \qquad (5.10)$$

where $\epsilon^{acc \times eff}$ is the total acceptance×efficiency, which includes all other efficiencies, e.g. ϵ^{det} is the detection efficiency where muons must pass through a certain number of strips to be reconstructed, ϵ^{embed} is the multiplicity dependent embedding efficiency which takes care of the inefficiencies occuring due to the high multiplicity environment in Au+Au collisions, $\epsilon^{smearing}$ is due to the smearing effect of the momentum resolution which includes detector's inefficiencies to reconstruct the actual momentum correctly and ϵ^{reco} is the reconstruction efficiency of the software's ability to reconstruct a muon track with the available number hits.

$$\epsilon^{acc \times eff} = \epsilon^{det} \times \epsilon^{embed} \times \epsilon^{smearing} \times \epsilon^{reco} \qquad (5.11)$$

One might expect that the total acceptance×efficiency will not be a constant factor since the state of the detector or the collision environment changes over the time. But the run-by-run efficiency fluctuations are ignored for this analysis. Since the dataset was taken in a very small amount of time (~ 2 weeks), we assumed that the detector configurations did not change much.

5.7.1 MuID Tube Efficiencies

MuID tube efficiencies are included in the simulations while determining the overall acceptance×efficiency of the muon arm detector. This is a data driven technique and is calculated by the requirement that the reconstructed roads should pass all the cuts with and without a hit in the MuID plane in question, and then check if we have a hit or not in that plane to calculate the efficiency. First, the code loops over the reconstructed MuTr tracks and find the closest associated MuID road. Then it checks at each plane whether there is a MuID hit associated with that road and its position relative to the road fit. The relative number of hits associated with those MuID roads is considered as the efficiency. The efficiencies obtained with this method for all tubes on every plane of the MuID are shown in Fig. 5.12. The tube id is plotted on the x-axis while the efficiencies are on the y-axis. The numbering convention of the MuID panels can be seen in Fig. 3.8. The plane averaged values are listed in Table 5.11.

Table 5.11: MuID tube efficiencies.

Arm	Plane 0	Plane 1	Plane 2	Plane 3	Plane 4	Average
South	0.953	0.941	0.966	0.943	0.853	0.931
North	0.942	0.915	0.927	0.898	0.809	0.898

5.7.2 Flat Mass Simulation

As discussed earlier, dimuon spectra decomposition was used in order to disentangle J/ψ production from other physics processes. Due to the decay kinematics of the dimuons and a limited theta acceptance of the muon arm, it was found that the dimuon acceptance is not uniform over the entire dimuon mass range. It is important to account for the correct acceptance shape while fitting the dimuon spectra for different physics processes. To calculate the dimuon acceptance, a flat mass Monte Carlo (MC) simulation was run. Dimuon events
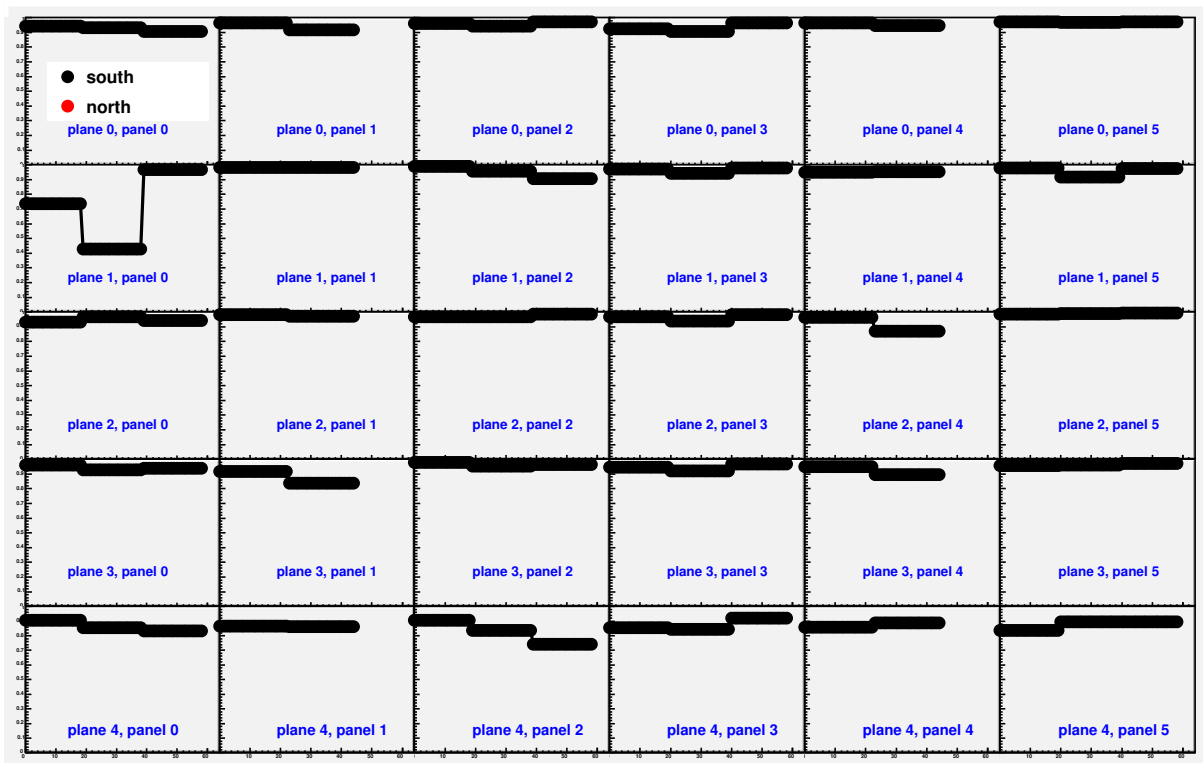
Figure 5.12: MuID tube efficiencies for south arm panels (horizontal plane)

were generated with flat mass, p_T and rapidity distributions and allowed to decay randomly to two unlike-sign muons. Details of the input distributions of the dimuons are mentioned in Table5.12. These muons were then run through the detector simulation chain, in order to account for detector acceptance. The simulated detector hits are then reconstructed with the same code as data in order to account for the reconstruction efficiency and dimuon acceptance in all phase space. Details about the detector simulations and simulating detector response is discussed in the next section. Fig. 5.13 and 5.14 show the mass dependent dimuon acceptance for different p_T and centrality bins for south arm. One can see that the PHENIX muon arms do not have uniform acceptance in all mass regions. The two dotted lines represent the J/ψ mass region (2.6-3.6 GeV where the J/ψ peak at $\sim$3.1 GeV is expected) where mass acceptance is not uniform. Hence, this line shape was used to acceptance weight our fit function in order to properly account for the mass dependent acceptance. This acc$\times$eff

Table 5.12: Summary of the generated J/ψ in flat mass simulation.

Variables	Range	Distributions
z-vertex	$-30 < z < 30$ cm	BBC z-distribution
dimuon p_T	$0 < p_T < 5$ GeV/c	Flat distribution
dimuon rapidity	$1.2 < |y| < 2.2$	Flat distribution
dimuon mass	$0 < m_{\mu\mu} < 5$ GeV	Flat distribution

also can be used for overall J/ψ yield correction but a separate Pythia simulation with realistic p_T and rapidity (instead of flat) distribution was run for the yield correction and both simulations agree with each other.
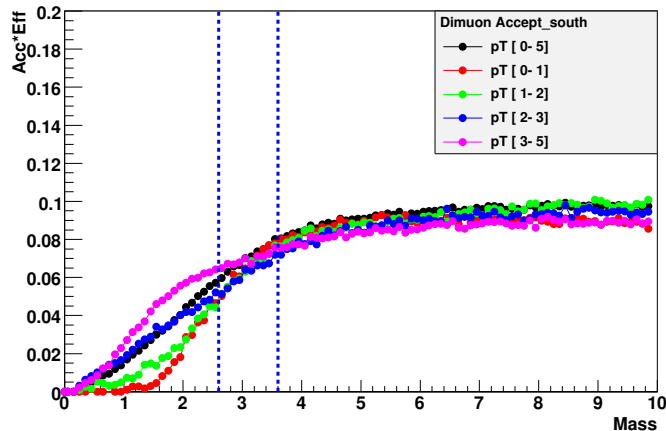
Figure 5.13: Dimuon mass acceptance of the south arm for different p_T bins.

5.7.3 Pythia Particle Generator

The Pythia event generator was used to generate J/ψ samples from $p+p$ collisions to calculate the overall acceptance×efficiency for J/ψ signals. Simulated J/ψ samples were generated using Pythia version 6.205, with the gluon fusion $(g + g \rightarrow J/\psi + g)$ process se-
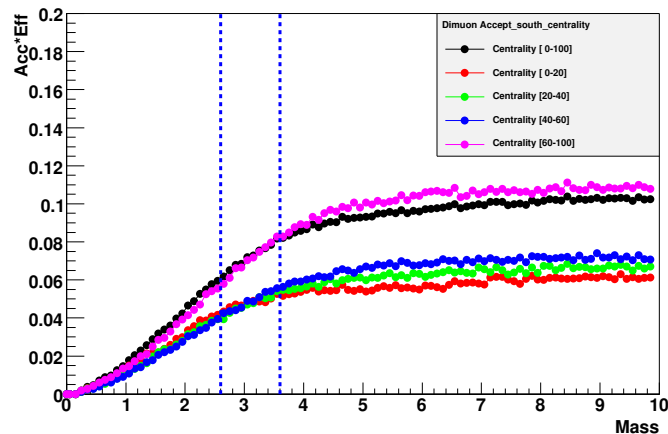
Figure 5.14: Dimuon mass acceptance of the south arm for different centrality bins.

lected (MSUB(86)=1) and only dimuon decay channel ($J/\psi \to \mu^+\mu^-$) activated at center of mass energies $\sqrt{s} = 39$, 62.4 GeV $p+p$ collisions. Muons from J/ψ decay were filtered prior to the detector simulation stage by requiring both the muons to go into $143° < \theta < 171°$ for South Arm and $9° < \theta < 37°$ for the North Arm, so they could be to get detected by the muon arms for a successful J/ψ reconstruction. Real data vertex information was extracted into a text file and then used to shift the Pythia event to that real-data z-vertex coordinates. A data driven z-vertex distribution and more realistic p_T and rapidity distribution of the J/ψ events from Pythia generator are the key assumptions for the input parameters. Since the collision z-vertex is determined by the BBC North-South timing difference, it is known only to about ± 0.5 cm (BBC vertex resolution). To reflect this, some extra smearing was added to the simulated event z-position by a Gaussian distribution of σ=0.5 cm. Fig. 5.15 and Fig. 5.16 shows the input J/ψ p_T and rapidity distribution (normalized to 1) at 39, 62.4 and 200 GeV $p+p$ collisions. As can be seen in Fig. 5.15 the J/ψ rapidity distribution at 39 GeV is much narrower than at 200 GeV. This illutrates the primary difficulty of any lower energy measurements with forward muon arms at rapidity $1.2 < |y| < 2.2$, where multiplicity decreases compared to mid rapidity (y~0) and it is very hard to make a consistent measurements as a function of $\sqrt{s}$. The p_T distribution also drops quickly at lower energies,

as can be seen in Fig. 5.16.
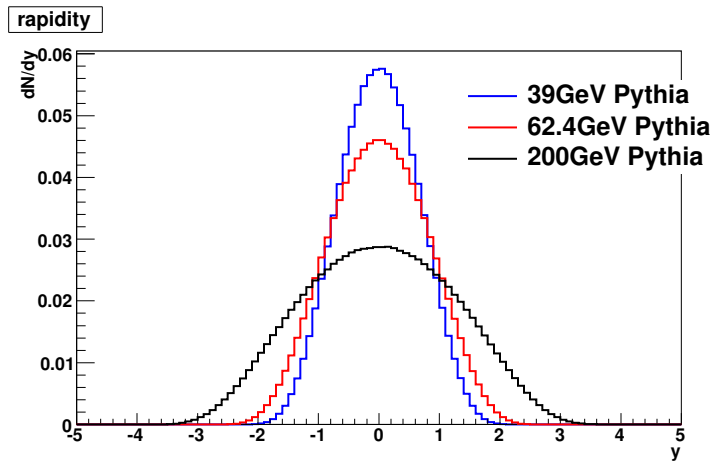
Figure 5.15: J/ψ rapidity distributions from Pythia generator for different energies.
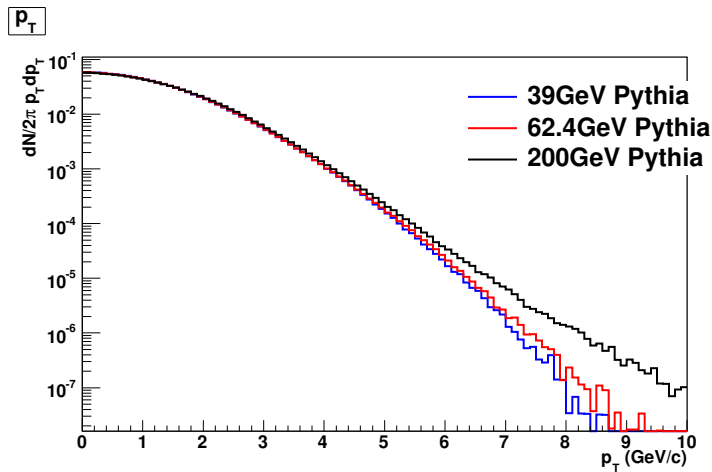
Figure 5.16: J/ψ p_T distributions from Pythia generator for different energies.

5.7.4 PISA and Detector Response

The PHENIX GEANT3 detector simulation (PISA) propagates the produced parti-
cle through the detector materials, and accounts for detector hit locations and energy loss
(dE/dx), as well as deflections due to the magnetic field. GEANT is a detector description

and simulation tool which is heavily used in high energy particle physics community for simulating particle passage through matter [72]. After PISA, standard muon reconstruction software reconstructs the tracks from the simulated hits with very similar procedure as used with data. Once GEANT processes the particle passages and simulates the hit locations and energy loss information in MuTr, the detector response is simulated as follows:

MuTr response

In real data the MuTr charge distribution follows a Landau distribution. Landau parameters are extracted from the real data and used to simulate the detector response. The simulated charge deposition distribution should also follow the same Landau distribution. Due to detector configurations, separate Landau parameters are used for each MuTr gas gap. These parameters are used to convert dE/dx to charge distribution. ADC values were calculated from the charge and zero-suppression was applied in order to simulate the electronics behavior in the actual experiment. The charge distribution in adjacent strips (when more than 1 strip is hit) were then fitted, to find out the centroid of the hit location. The MuTr response also includes the behavior of high voltage modules, dead anode wires, dead FEMs, the scratched cathodes in the North Arm, and the gain and pedestal calibrations. While running the simulations, it is mandatory to specify a reference run, and each run can be mapped to a timestamp when the data was taken. The detector configurations are stored in the PHENIX database for every run or any given point of time. This information was further used to simulate real detector condition while calculating acc×eff.

MuID response

MuID detector response is little simpler. The MuID two pack efficiencies are already extracted for each MuID tube from the real data using a purely data driven technique and kept in a separate file as discussed in section 5.7.1. The simulated two-packs are then drawn randomly with that given probability distribution. After simulating MuTr and MuID detector response, the track finding algorithm in MuTr and the road finding algorithm in MuID were run exactly the same as data to reconstruct the simulated particle. The effect

of random hits was studied in both MuTr and MuID and found to be insignificant, causing only a small loss in tracking efficiency.

5.7.5 Embedding

Next, in order study the multiplicity effect on acceptance×efficiency, the simulated dimuons were embedded into real data events. This step assumes that the probability of finding a J/ψ in a single event is almost negligible and by embedding simulated J/ψ s into a real events, a realistic environment is recreated of higher multiplicity backgrounds generated in heavy ion collisions. The multiplicity is significantly lower in 39 and 62.4 GeV than compared to 200 GeV Au+Au collisions. In 200 GeV Au+Au collisions the number of tracks in a single event is very large compared to $p+p$ events and the multiplicity effect is significant, i.e. the higher number of tracks make it more difficult to properly reconstruct each of the muon tracks individually and result in a loss of acceptance×efficiency for the most central collisions. A compilation of the track multiplicity distributions at different collision energies is shown in Figs. 5.17 and 5.18 for MuTr south and MuTr north, respectively. When embedding PYTHIA J/ψ events into real data events, real data hits were added with the simulated hits. Charge, and ADC values of the MC particles are merged with real hits strip-by-strip. If a strip has both MC and data hits, then their charge is just added together. The MuID, tube hits are similarly merged if they have either MC or real data hits. The same version of the reconstruction code with exact detector configurations as data, was used to reconstruct these embedded events. One would expect the multiplicity distributions to be the same in both the North and South arms since Au+Au collisions are symmetric but, interesting enough, the multiplicity is higher in the North arm of 200 GeV, although at 39 and 62.4 GeV they are very similar.

As the low energy runs lasted for a very short time period in comparison with the typical running length at the full energy (200 GeV), one can expect not much of run-to-run variation in the detector configuration which might cause acceptance×efficiency fluctuations. Two reference runs (311032 and 312994) were taken as representatives from the run-list (one
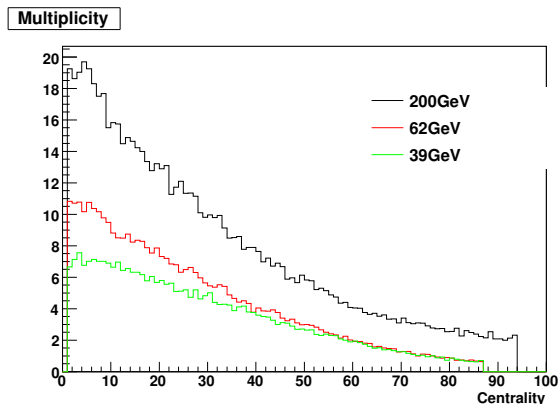
Figure 5.17: MuTr track multiplicity at different energies in MuTr south.
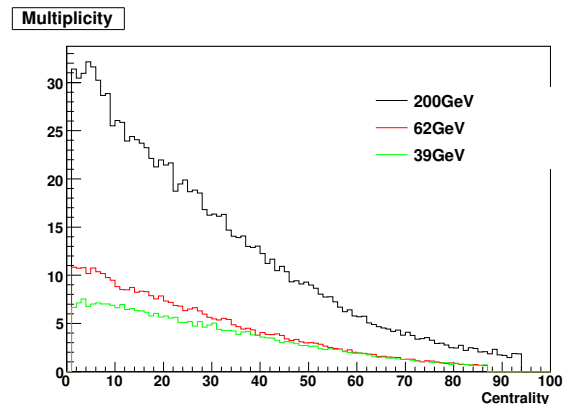
Figure 5.18: MuTr track multiplicity at different energies in MuTr north.

from the beginning of the run and one at the end of the run period). No significant variation in overall mass acc×eff was found. The vertex distribution of the simulated input events was extracted from data within ± 30 cm. While embedding, the vertex of the simulated events and data events were matched sequentially keeping in mind that the event characteristics depend on z-vertex. A realistic z-vertex distribution is important because the geometric acceptance changes depending on the collision vertex and the distance from the detector. Most importantly background particles are very much dependents on the z-vertex, because particles like pions and kaons have more time to decay to muons (aka "decay muons") when collisions are further away from the absorber, while the hard processes like the J/ψ production should have no z-vertex dependence. The acceptance× efficiency at 62.4 GeV after embedding is shown in Fig. 5.19 as a function of centrality and in Fig. 5.20 as a function of p_T. Fig. 5.21 shows the acc×eff at 39 GeV centrality bins. As seen in those figures, the acc×eff drops at central collisions compared to peripheral collision due to higher multiplicity in both 39 and 62.4 GeV. As mentioned earlier the multiplicity effect was significant at 200 GeV Au+Au collisions and the strong centrality dependence of the acc×eff was noticed [56]. But the multiplicity is much lower at 39 and 62.4 GeV Au+Au collisions (a factor of ∼2 and ∼3 lower in 62.4 and 39 GeV compared to 200 GeV) and only a weak centrality dependence is observed. Table 5.13 and 5.14 lists the acceptance and efficiency at 62.4 GeV
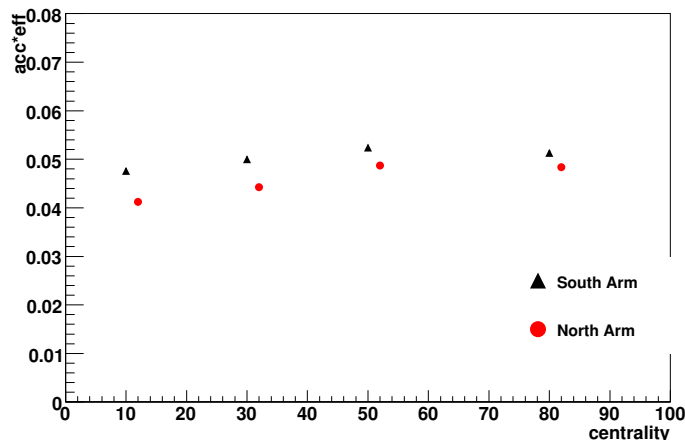
Figure 5.19: J/ψ acceptance×efficiency for four centrality bins at 62.4 GeV.

Table 5.13: Acceptance×efficiency in each centrality bin of 62.4 GeV data set.

Centrality	South Arm	North Arm
[0, 20]	0.0476 ± 0.0006	0.0413 ± 0.0005
[20, 40]	0.0500 ± 0.0006	0.0443 ± 0.0005
[40, 60]	0.0524 ± 0.0006	0.0487 ± 0.0006
[60, 86]	0.0513 ± 0.0005	0.0484 ± 0.0005

and Table 5.15 and 5.16 are for 39 GeV Au+Au collisions. One can also notice a drop in acceptance×efficiency between 62.4 GeV and 39 GeV because the rapidity and p_T distribution at these energies are not the same. The error bars are statistical errors and they are reduced significantly but generating enough statistics through simulation at 39 and 62.4 GeV.

5.8   Real Data and MC Matching

One way to quantify the accuracy of a realistic Monte Carlo simulation is to match the simulated distributions with that of the real data. Any difference is considered as the
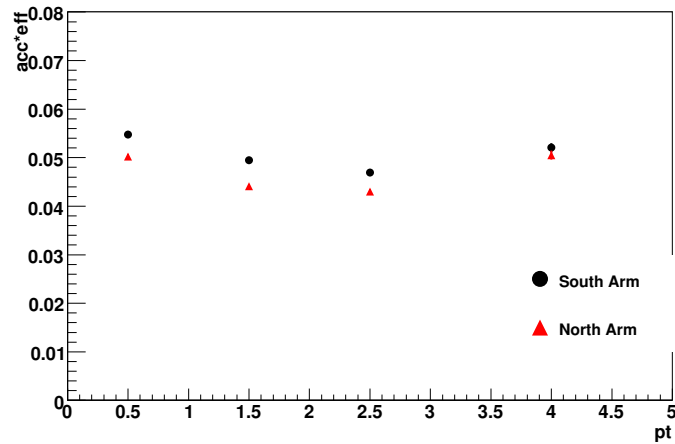
Figure 5.20: J/ψ acceptance×efficiency for four p_T bins at 62.4 GeV.

Table 5.14: Acceptance×efficiency as a function of p_T for 62.4 GeV.

P_T	South Arm	North Arm
[0, 1]	0.0548 ± 0.0006	0.0502 ± 0.0005
[1, 2]	0.0495 ± 0.0004	0.0441 ± 0.0004
[2, 3]	0.0469 ± 0.0005	0.0430 ± 0.0005
[3, 5]	0.0520 ± 0.0010	0.0505 ± 0.0009
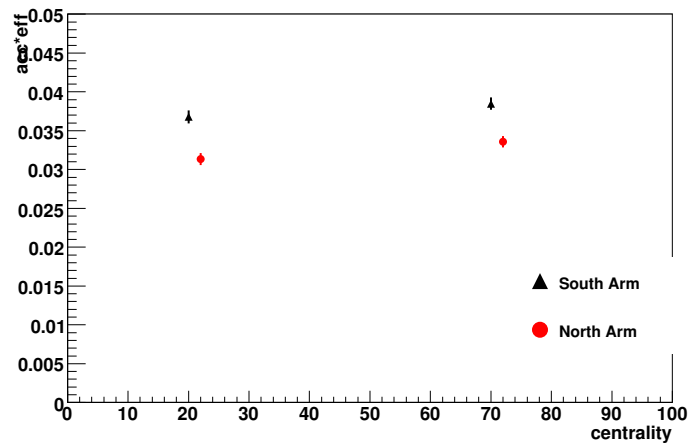
Figure 5.21: J/ψ acceptance×efficiency for two centrality bins at 39 GeV.

Table 5.15: Acceptance×efficiency as a function of centrality for 39 GeV.

Centrality	South Arm	North Arm
[0, 40]	0.0368 ± 0.0008	0.0313 ± 0.0008
[40, 86]	0.0385 ± 0.0009	0.0336 ± 0.0007

Table 5.16: Acceptance×efficiency as a function of p_T at 39 GeV.

P_T	South Arm	North Arm
[0, 1]	0.042 ± 0.001	0.036 ± 0.001
[1, 2]	0.036 ± 0.001	0.032 ± 0.001
[2, 5]	0.036 ± 0.001	0.031 ± 0.001

systematic uncertainties. The detector condition varies over time and the database keeps track of the detector conditions e.g. high voltage, dead areas, tripped channels etc. run-by-run. In the simulation, a particular reference run was used to pull out the information about the detector conditions. In this way, the simulation reproduces the inactive dead areas very well. Fig. 5.22 show the radiographs of the muon tracks reconstructed in the south muon arm. The plot shows the x and y coordinates of the hits associated with the tracks at each of the 8 gaps in the south muon arm (stations are plotted vertically and different gaps are in horizontal panels). One can see the octants and the regions where there are no hits in addition to the areas between the octants. These areas are caused by dead cathodes in MuTr, which were not working. This decreases the J/ψ detection efficiencies significantly because in order to be able to reconstruct a J/ψ successfully, the detector has to be able to measure both the muons efficiently. A similar plot can also be made from simulated events but a more direct comparison of radial distance, θ and ϕ angle was plotted in Fig. 5.23, Fig. 5.24 and Fig. 5.25, respectively for 62.4 GeV Au+Au collisions. Different octants are clearly seen
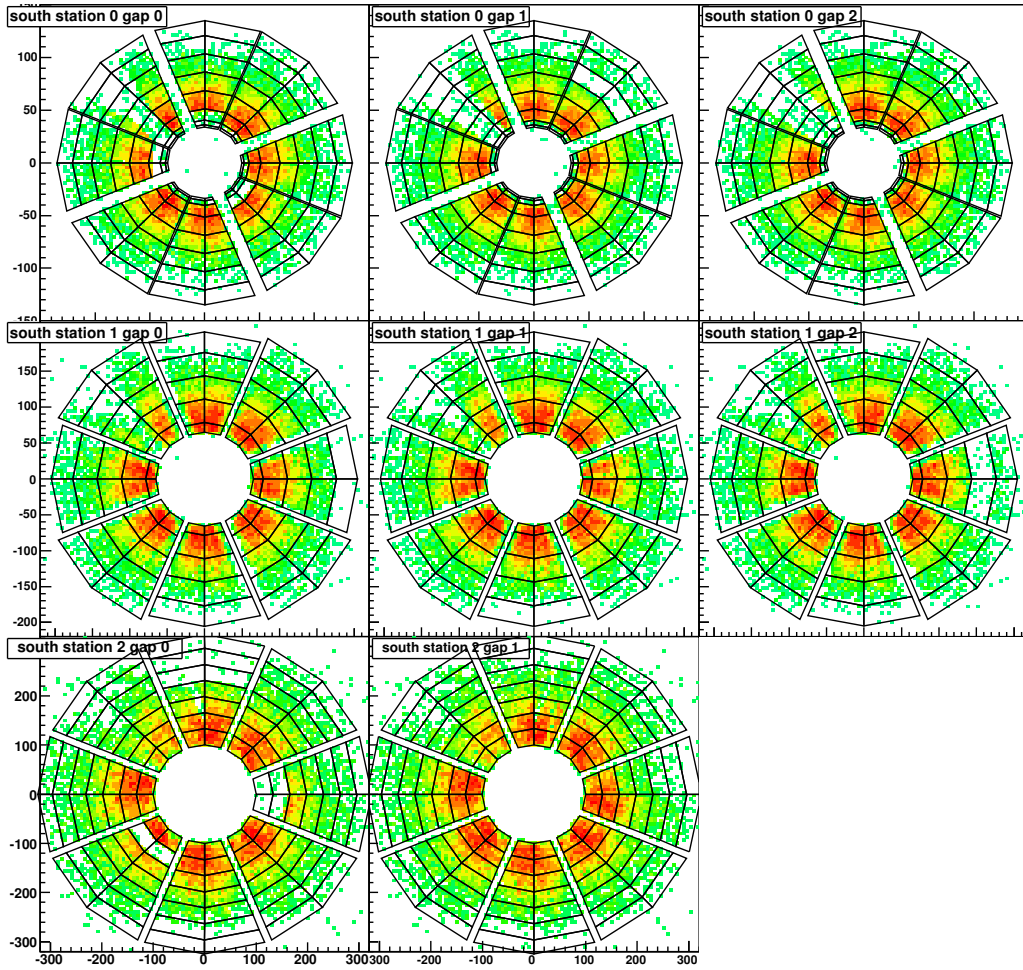
Figure 5.22: Radiographs of the south arm from real data (runnumber = 311032).

in eight peaks in the phi distributions of the tracks in Fig. 5.25. The systematic error due to the acceptance difference between simulation and real data is discussed in the next section.
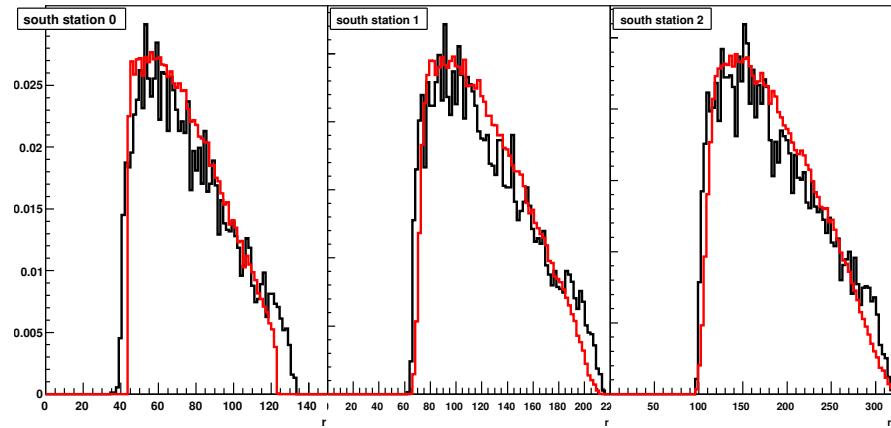
Figure 5.23: Radial distribution comparison between data (black) and MC (red) for the south arm.
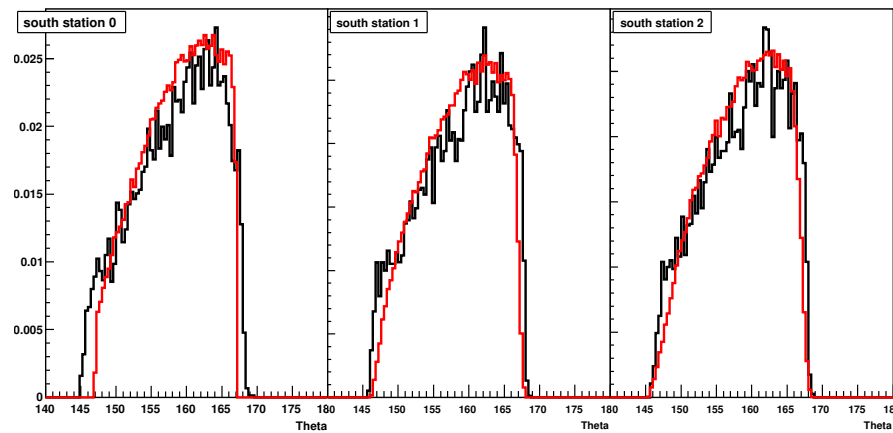
Figure 5.24: θ distribution comparison between data (black) and MC (red) for the south arm.
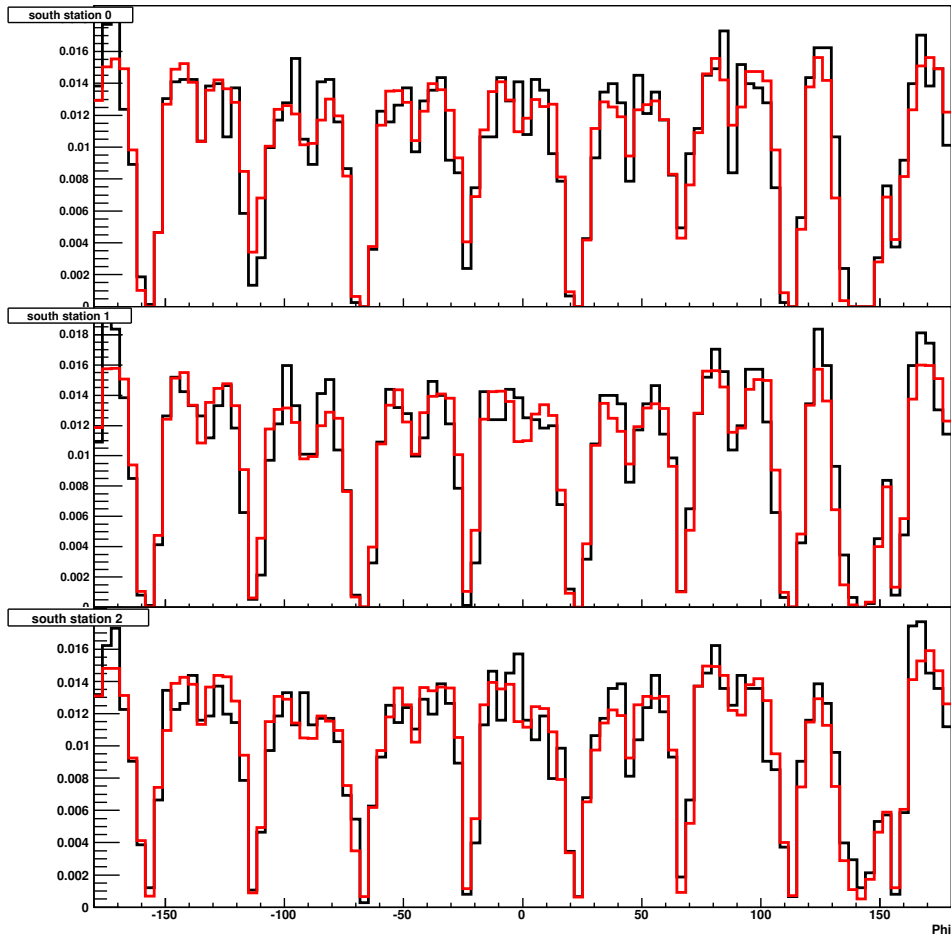
Figure 5.25: ϕ distribution comparison between data (black) and MC (red) for the south arm.

CHAPTER 6

SYSTEMATIC ERRORS

6.1 Introduction

In this section different sources of systematic errors are summarized. These sources include detector inefficiencies, fluctuations, mis-identifications and not-well-understood data behavior and analysis techniques. The types of errors included in this analysis are classified in three categories:

- Point-to-point uncorrelated systematic errors (type A), for which all measured points can vary independently from others within the error limit.

- Point-to-point correlated systematic errors (type B), for which points vary in a correlated way within error bars, not necessarily in same direction.

- Global systematic errors (type C), for which all points move coherently within the error bars by a fixed fraction of their values.

The first type of error is uncorrelated point to point and can be added quadratically with statistical errors. Total uncorrelated errors are later used as weights while fitting the results. A summary of the all systematic errors are given in Table 6.1. Details of these error sources are discussed in the following sections:

6.2 Signal Extraction

The systematic error associated with the extracted number of J/ψ counts from the background subtracted dimuon invariant mass distribution was calculated by varying the normalization factor and the relative ratio of the two Gaussians while fitting the J/ψ component.

1. The uncertainty on the unlike-sign mixed background normalization factor ($\pm 2\%$)

2. The uncertainty on the two gaussian fraction in J/ψ mass region ($\pm 25\%$)

For the 39 GeV dataset integrated J/Ψ counts with the mass range [2.6 - 3.6] GeV were used due to lower statistics. No fit was performed and a systematic error of 15% was added for the 39 GeV dataset. The above errors are counted as point-to-point uncorrelated errors and they are included in Table 5.7 and Table 5.8 for 62.4 GeV and Table. 5.9 for 39 GeV.

6.3   Acceptance×efficiency Calculation

Both the detector acceptance and efficiency vary with the simulated J/ψ rapidity and transverse momentum distribution. Even though a real z-vertex distribution was used for the embedding process, some run-to-run variations may occur resulting a variation in the correction factor which are not covered by statistical errors. The systematic errors on the acc×eff were estimated by varying these factors and estimating how sensitive they are to the correction factors.

1. The default Pythia J/ψ rapidity distribution was used in acc×eff simulation. The rapidity distribution in actual Au+Au collisions is unknown. To account for this the Pythia parton distributions were varied to account for rapidity modifications.

2. The default Pythia J/ψ transverse momentum distribution was used for acc×eff calculations. Later it was varied using different Kaplan fits to $p+p$ and Au+Au data in order to account for possible p_T modifications.

3. The Simulated vertex distribution of the J/ψ events was taken from the real data. Approximate Gaussian distributions with similar variance but different means (z=5, 10,-5,-10) were used as fluctuations in vertex distribution.

The total error, a quadratic sum of above three contributions, is close to 4%. This error is counted as a point-to-point correlated type error.

6.4 Detector Acceptance

The systematic error due to possible ϕ angle distribution mismatch between real data and simulation was also included. We compared the ϕ angle distribution (shown in Fig. 5.25) between the Monte Carlo simulation and real data in order to calculate single track occupancy in each octant. The uncertainty is given by:

$$\sigma_{single,oct} = \frac{MC_{oct} - RD_{oct}}{RD_{oct}}, \tag{6.1}$$

$$\sigma_{pair} = \frac{1}{N_{oct}} \sqrt{\sum_{oct} (2 * \sigma^2_{single,oct})}. \tag{6.2}$$

where RD stands for real data and MC stands for Monte Carlo simulation. An estimated 5% correlated systematic error is added due to this contribution.

6.5 Detector Efficiency

Systematic errors due to detector efficiencies were taken into account as follows;

- A 4% systematic error was assigned due to uncertainties in MuID tube efficiencies.

- A 2% systematic error was assigned due to MuTr overall efficiency.

The above errors are considered as point-to-point correlated, since any difference between true and estimated detector efficiency will affect all acceptance×efficiency points in the same direction.

6.6 North/South Discrepancy and Arm Average

For peripheral bins, the acceptance corrected invariant yields between south and north arms match very well. However, in central collision events a 1 to 1.5 sigma deviation is observed between south and north arms. Hence, a 3% systematic error (type B) is added to the central bins due to north/south arm mismatch.

6.7 Number of Nucleon-Nucleon Collisions

The number of average nucleon-nucleon collisions $\langle N_{coll} \rangle$ was calculated using a Glauber Monte Carlo simulation. The input parameters were varied in the simulation to account for the systematic errors. The uncertainty in the number of binary collisions are listed in Table 5.3. This type of error is considered as point-to-point correlated error.

6.8 BBC Efficiency

One should be careful with systematics from BBC trigger efficiency because it has been already included in N_{coll} systematics. So for R_{CP} calculations, there is no need to add this error. However for invariant yield calculations it must be added. We should note that the efficiencies are 85.9 +/- 2% for 39 GeV and 85.7 +/- 2% for 62.4 GeV as determined by Glauber simulations. Hence a type B systematic error of 2.3% was added for 62.4 GeV and 39 GeV invariant yield calculations.

Table 6.1: Systematic uncertainties

Description	Contribution	Type
Yield extraction	2-10%	A
Detector acceptance	5%	B
Input y,p_{T} distribution	4%	B
MuTr efficiency	2%	B
MuID efficiency	4%	B
Arm mismatch	0-3%	B
DATA and MC mismatch	4%	B
$\langle N_{\mathrm{coll}} \rangle$	10-11.5%	B
BBC Efficiency	2.3%	C

CHAPTER 7

RESULTS

The J/ψ meson studied in this analysis is through the $\mu^+\mu^-$ decay mode (branching ratio, BR=5.93 ±0.06%). It generally identified by a prominent peak at 3.096 GeV. The physical quantities we are interest in measuring are the invariant yields and nuclear modification factors. The invariant cross section of a J/ψ with momentum p_T, is expressed as

$$E\frac{d^3\sigma_{J/\psi}}{dp^3} = \frac{d^3\sigma_{J/\psi}}{d\phi dy p_T dp_T} = \frac{1}{2\pi p_T}\frac{d^2\sigma_{J/\psi}}{dy dp_T} \tag{7.1}$$

where y is the rapidity, ϕ is the azimuthal angle and p_T is the transverse momentum ($\sqrt{p_x^2 + p_y^2}$) of the J/ψ. The J/ψ invariant cross section extracted experimentally through the dimuon decay mode, are written as:

$$B_{\mu\mu}\frac{d^2\sigma_{J/\psi}}{2\pi p_T dp_T dy} = \frac{1}{2\pi p_T}\frac{n_{j/\psi}(p_T)}{\int Ldt\epsilon(p_T)\Delta p_T \Delta y} \tag{7.2}$$

where $n_{J/\psi}$ is the number of J/ψ reconstructed in a particular p_T and rapidity bin. ϵ is the overall (rapidity integrated) acceptance × efficiency as a function of p_T as estimated by simulations, Δp_T and Δy are the p_T and rapidity bin width. $B_{\mu\mu}$ is the branching ratio of $J/\psi \to \mu^+\mu^-$ decay. $\int Ldt$ is the integrated luminosity described by

$$\int Ldt = \frac{N_{MB}}{\sigma_{AuAu}\epsilon_{MB}^{AuAu}} = \frac{N_{MB}}{\langle N_{coll}^{MB}\rangle \sigma_{p+p}\epsilon_{MB}^{AuAu}} \tag{7.3}$$

σ_{p+p} and σ_{Au+Au} are the inelastic cross-sections in $p+p$ and Au+Au collisions, ϵ_{MB}^{Au+Au} is the MB trigger efficiency and $\langle N_{coll}^{MB}\rangle$ is the mean number of binary collisions calculated from Glauber model calculations. Due to low statistics at lower energy Au+Au collisions,

integrated J/ψ yields are calculated, which can be written as,

$$B_{\mu\mu}\frac{dN_{J/\psi}}{dy} = BR\sum \frac{1}{2\pi p_T}\frac{dN^2_{J/\psi}}{dp_T dy}\Delta p_T \qquad (7.4)$$

In this work, the J/ψ invariant yield (p_T integrated) in each centrality bin is reported without dividing by σ_{p+p}, which is not measured by our experiment. An extrapolation of the $p+p$ inelastic cross section at $\sqrt{s} = 39$ and 62.4 GeV is used to convert the invariant yields to the differential cross-section.

$$B_{\mu\mu}\frac{dN_{J/\psi}}{dy} = \frac{1}{\epsilon^{BBC}_{MB}}\frac{1}{N^i_{MB}}\frac{\Delta n^i_{j/\psi}}{\Delta y}\frac{1}{A\epsilon^i}, \qquad (7.5)$$

where, i is the ith centrality bin and B stands for the branching ratio. ϵ^{BBC}_{MB} is the BBC efficiency for the minimum bias trigger. For p_T dependent yields, one would have

$$B_{\mu\mu}\frac{d^3N_{J/\psi}}{dp_T^2 dy} = \frac{1}{\epsilon^{BBC}_{MB}}\frac{1}{N_{MB}}\frac{1}{2\pi p_T}\frac{\Delta n_{j/\psi}}{\Delta p_T \Delta y}\frac{1}{A\epsilon(p_T)}, \qquad (7.6)$$

where $n_{J/\psi}$ is the extracted signal counts and N_{MB} is the number of BBC minimum bias triggered events that were processed. $A\epsilon$ is the acceptance×efficiency and Δy and Δp_T are the y and p_T bin widths, respectively.

7.1 Arm Average

The analysis for each arm follows very a similar procedure but they are independent of each other. The total number of J/ψ counts, acc×eff and number of minimum bias events are calculated separately for each arm. Since the Au+Au collisions are expected to be symmetric, the north and south muon arm results should yield the same result. So the invariant yields from North and South were averaged.

To take into account the different uncertainties in the north and south arm, the weighted

averaged J/ψ invariant yields are calculated as,

$$Y_{avg} = \frac{w_S Y_S + w_N Y_N}{w_S + w_N},\tag{7.7}$$

where Y_S and Y_N are the south and north arm invariant yields. w_S and w_N are the corresponding weights (for the south and north arms) which account for all errors associated with each measurement that are independent from one arm to the other,

$$w = 1/\sigma^2_{arm,uncor}\tag{7.8}$$

where σ_{uncor} is the total uncorrelated systematic error. The total uncorrelated errors represents the quadrature sum of the statistical error and the type A systematic errors. The uncertainties in the average invariant yields are calculated as a quadrature sum of the two independent uncorrelated errors and weighted accordingly:

$$\sigma_{stat} = \sqrt{\frac{(w_N \sigma_{N,stat})^2 + (w_S \sigma_{S,stat})^2}{(w_S + w_N)^2}},\tag{7.9}$$

$$\sigma_{typeA} = \sqrt{\frac{(w_N \sigma_{N,typeA})^2 + (w_S \sigma_{S,typeA})^2}{(w_S + w_N)^2}},\tag{7.10}$$

where σ_{stat} and σ_{typeA} are the averaged statistical and type A errors. The total correlated systematic error (type B) on the average yield is:

$$\sigma_{typeB} = \sqrt{\sum \sigma^i_{typeB}}^2\tag{7.11}$$

The total correlated systematic is just the quadrature sum of the all the type B systematic uncertainties as discussed in chapter 6. The correlated errors were not weighted since those uncertainties affect both arms in a correlated fashion.

62.4 GeV

Tables. 7.1 and 7.2 list the invariant yields for each arm separately and Table. 7.3
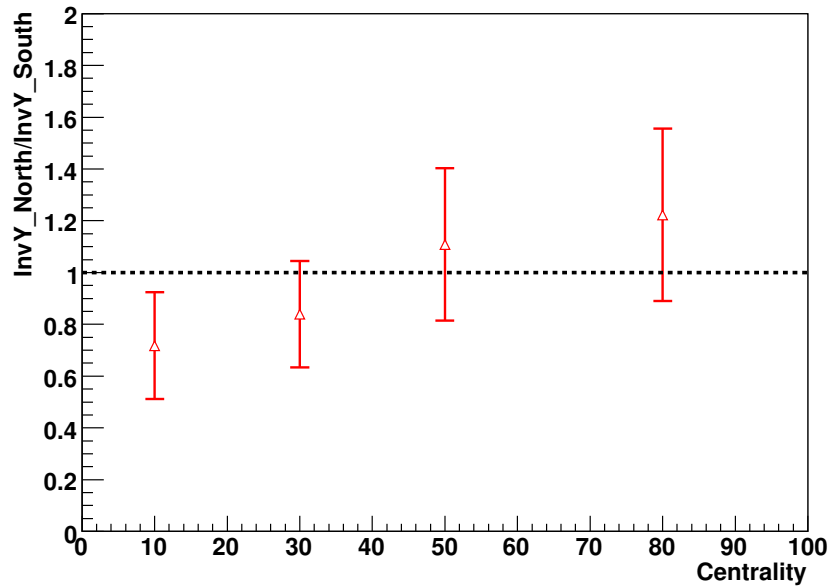
Figure 7.1: Ratio of the invariant yields between north and south arms at 62.4 GeV Au+Au collisions.

shows the resulting two arm averaged yield in centrality bins for 62.4 GeV. The ratio of the invariant yields between two arms in four centrality bins is shown in Fig. 7.1. It can be seen that the yields are in agreement between the two arms within the one-sigma level but the uncertainties are higher due to low statistics.

Similarly Tables 7.4 and 7.5 shows the invariant yields in four different p_T bins at 62.4 GeV and Table 7.6 shows the average yields in p_T bins.

Table 7.1: South arm J/ψ invariant yields for four centrality bins (p_T integrated).

Cent.	$N_{J/\psi}$	$A\epsilon$	N_{MB}	B dN/dy	$\pm$ stat.	$\pm$ typeA	$\pm$ typeB
[0, 20]	338.95	0.0476	1.28e+08	4.77e-05	7.38e-06	9.15e-07	3.88e-06
[20, 40]	179.04	0.050	1.28e+08	2.4e-05	4e-06	9.7e-07	1.95e-06
[40, 60]	68.7013	0.052	1.28e+08	8.77e-06	1.59e-06	4.21e-07	7.14e-07
[60, 86]	29.6671	0.0513	1.66e+08	2.98e-06	5.82e-07	3.89e-08	2.42e-07

Table 7.2: North arm J/ψ invariant yields for four centrality bins (p_T integrated).

Cent.	$N_{J/\psi}$	$A\epsilon$	N_{MB}	B dN/dy	$\pm$ stat.	$\pm$ typeA	$\pm$ typeB
[0, 20]	211.13	0.0413	1.28e+08	3.42e-05	8.24e-06	6.29e-07	2.79e-06
[20, 40]	133.16	0.044	1.28e+08	2.01e-05	3.51e-06	3.69e-07	1.64e-06
[40, 60]	70.91	0.049	1.28e+08	9.73e-06	1.82e-06	1.36e-07	7.92e-07
[60, 86]	34.24	0.048	1.67e+08	3.64e-06	6.87e-07	5.07e-08	2.96e-07

Table 7.3: Average invariant yields in centrality bins (p_T integrated).

Cent.	B dN/dy	$\pm$ stat.	$\pm$ typeA	$\pm$ typeB
[0, 20]	4.17e-05	5.5e-06	5.79e-07	3.61e-06
[20, 40]	2.18e-05	2.64e-06	4.63e-07	1.89e-06
[40, 60]	9.2e-06	1.2e-06	2.4e-07	7.49e-07
[60, 86]	3.25e-06	4.44e-07	3.1e-08	2.65e-07

Table 7.4: South arm J/ψ invariant yields in p_T bins for centrality [0,86].

p_T	$N_{J/\psi}$	$A\epsilon$	N_{MB}	B dN/dy	$\pm$ stat.	$\pm$ typeA	$\pm$ typeB
[0, 1]	216.47	0.055	5.5e8	1.96e-06	3.53e-07	4.2e-08	1.7e-07
[1, 2]	205.96	0.050	5.5e8	6.87e-07	1.3e-07	1.86e-08	5.6e-08
[2, 3]	112.84	0.047	5.5e8	2.38e-07	5.36e-08	4.12e-09	1.94e-08
[3, 5]	34.06	0.052	5.5e8	2.03e-08	7.62e-09	1.51e-09	1.65e-09

Table 7.5: North arm J/ψ invariant yields in p_T bins for centrality [0,86].

p_T	$N_{J/\psi}$	$A\epsilon$	N_{MB}	B dN/dy	$\pm$ stat.	$\pm$ typeA	$\pm$ typeB
[0, 1]	134.12	0.050	5.51e+08	1.32e-06	3.58e-07	6.99e-08	1.15e-07
[1, 2]	195.88	0.044	5.51e+08	7.33e-07	1.37e-07	1.6e-08	5.96e-08
[2, 3]	76.09	0.043	5.51e+08	1.75e-07	4.94e-08	6.27e-09	1.43e-08
[3, 5]	19.04	0.051	5.51e+08	1.17e-08	8.68e-09	1.11e-09	9.49e-10

Table 7.6: Averaged invariant yields in p_T bins for centrality [0,86].

p_T	B dN/dy	$\pm$ stat.	$\pm$ typeA	$\pm$ typeB
[0, 1]	1.65e-06	2.51e-07	4.02e-08	1.43e-07
[1, 2]	7.09e-07	9.41e-08	1.24e-08	6.15e-08
[2, 3]	2.04e-07	3.63e-08	3.87e-09	1.77e-08
[3, 5]	1.65e-08	5.73e-09	9.74e-10	1.43e-09

39 GeV

Invariant yield at 39 GeV were done in a similar way as in the 62.4 GeV data set. There are 2 centrality bins and 3 p_T bins at 39 GeV because of low statistics. The invariant yields in the two centrality bins can be found individually in Tables 7.7 and 7.8 and the average in Table. 7.9. The yields between two arms match within uncertainties.

Table 7.7: South arm J/ψ invariant yields for centrality bins (p_T integrated) at 39 GeV.

Cent.	$N_{J/\psi}$	$A\epsilon$	N_{MB}	B dN/dy	$\pm$ stat.	$\pm$ typeA	$\pm$ typeB
[0, 40]	86.71	0.037	9.29e+07	2.18e-05	7.78e-06	6.37e-07	3.72e-06
[40, 86]	19.20	0385	1.07e+08	3.99e-06	1.39e-06	1.52e-07	6.82e-07

Table 7.8: North arm J/ψ invariant yields for centrality bins (p_T integrated) at 39 GeV.

Cent.	$N_{J/\psi}$	$A\epsilon$	N_{MB}	B dN/dy	$\pm$ stat.	$\pm$ typeA	$\pm$ typeB
[0, 40]	63.8	0.0313	9.29e+07	1.88e-05	7.37e-06	8.61e-07	3.21e-06
[40, 86]	10.1	0.0336	1.07e+08	2.42e-06	1.21e-06	1.05e-08	4.13e-07

Table 7.9: Averaged invariant yields for 39 GeV.

Centrality	B dN/dy	$\pm$ stat.	$\pm$ typeA	$\pm$ typeB
[0, 20]	2.02e-05	5.35e-06	5.44e-07	3.4e-06
[20, 86]	3.09e-06	9.15e-07	6.52e-08	5.2e-07

Figure 7.2 shows the final J/ψ invariant yields in centrality bins integrated over all p_T in $\sqrt{s_{NN}} = 39$ and 62.4 GeV Au+Au collisions. The invariant yields are further scaled by

$1/\langle N_{\mathrm{coll}}\rangle$ and plotted as a function of the average number of participants $\langle N_{\mathrm{part}}\rangle$, as estimated for each of the centrality bins from Glauber simulations. For comparison, the previously published J/ψ invariant yields in the same rapidity range $1.2 < |y| < 2.2$ from $\sqrt{s_{NN}} = 200$ GeV Au+Au collisions are also shown [56]. The vertical error bars are the quadrature sum of the statistical and type A uncertainties, and the rectangular boxes represents the type B uncertainties. 200 GeV points are higher than 62.4 or 39 GeV, as one might expect that the cross section typically scales with energy and J/ψ yield is larger at higher energy. In addition, the yield per binary collision is decreasing with $\langle N_{\mathrm{part}}\rangle$ at all three energies, indicating increasing nuclear suppression for more central collisions. Figure 7.3 shows the invariant yield as a function of p_{T}, plotted at the center of each p_{T} bin, for $\sqrt{s_{NN}} = 39$ and 62.4 GeV Au+Au collisions. 62.4 GeV points were scaled by a factor of 10 for a visual clarity.

7.2 Nuclear Modification, R_{CP}

The nuclear modification of J/ψ yields can be categorized in different ways. Because the PHENIX experiment has not yet measured the $p+p$ reference baselines at $\sqrt{s_{NN}} = 39$ or 62.4 GeV, we first discuss the J/ψ R_{CP}, the nuclear modification of central relative to peripheral classes of events as defined below:

$$R_{\mathrm{CP}} = \frac{\frac{dN_{AuAu}/dy}{\langle N_{\mathrm{coll}}\rangle}(central)}{\frac{dN_{AuAu}/dy}{\langle N_{\mathrm{coll}}\rangle}(peripheral)} \tag{7.12}$$

The R_{CP} values are shown in Figure 7.4 and in Table 7.10 for Au+Au at 62.4 GeV. Note that the peripheral bin selection for Au+Au at 62.4 GeV is 60-86% centrality with a corresponding $\langle N_{\mathrm{coll}}\rangle = 14.3 \pm 1.7$. Many uncertainties in the invariant yields cancel for R_{CP} and the dominant uncertainties are from the normalization with respect to the peripheral bin including the uncertainties in the $\langle N_{\mathrm{coll}}\rangle$ values for each bin. The type C global systematic from the uncertainty in the peripheral $\langle N_{\mathrm{coll}}\rangle$ value is listed in the figure legend; the other systematic uncertainties are included in the boxes on each data point. For comparison, we
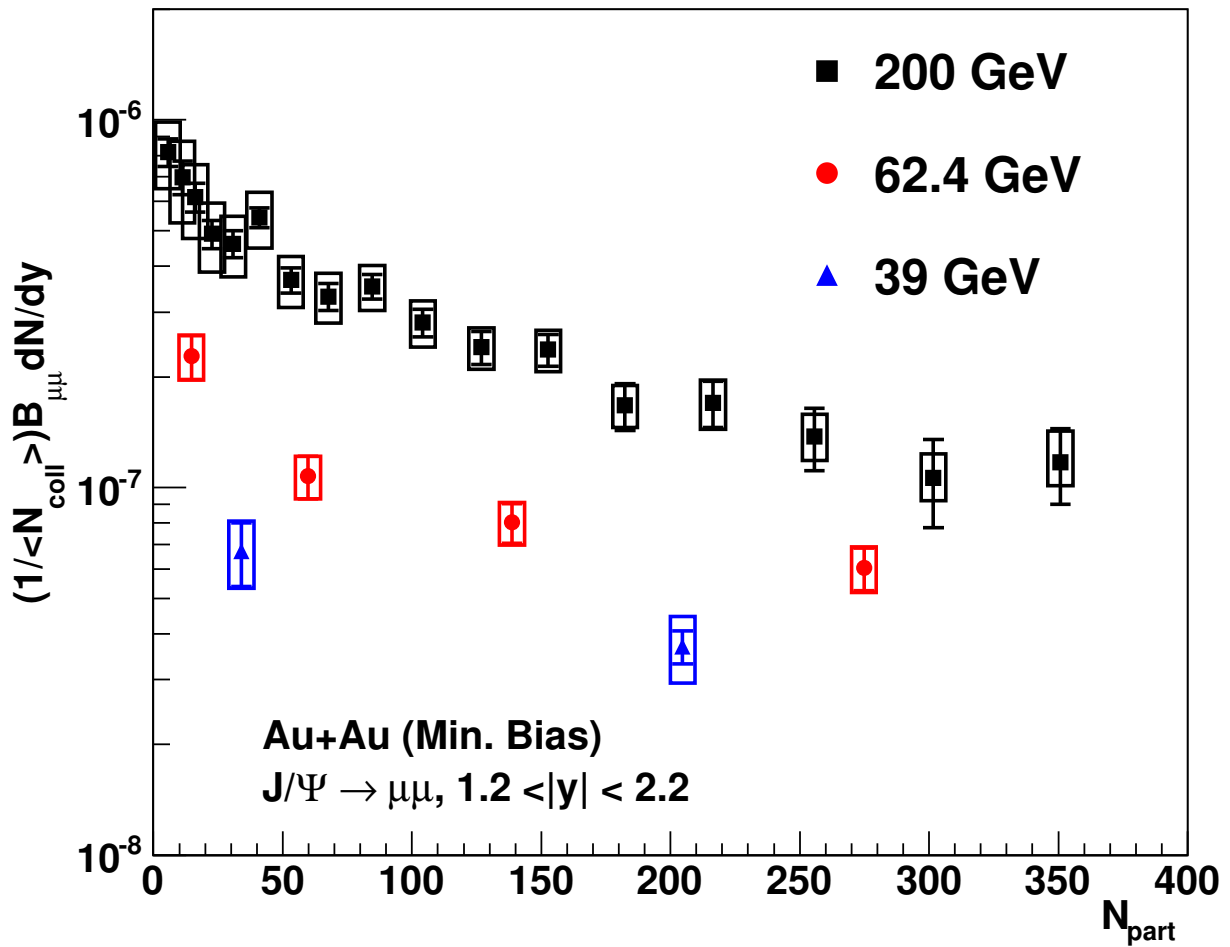
Figure 7.2: (color online) J/ψ invariant yields (scaled by $1/\langle N_{\text{coll}} \rangle$) are shown for Au+Au collisions at 39, 62.4, and 200 GeV as a function of the number of participating nucleons. The solid error bars represent the uncorrelated point-to-point uncertainties, and the boxes represent the correlated (type B) systematic uncertainties.
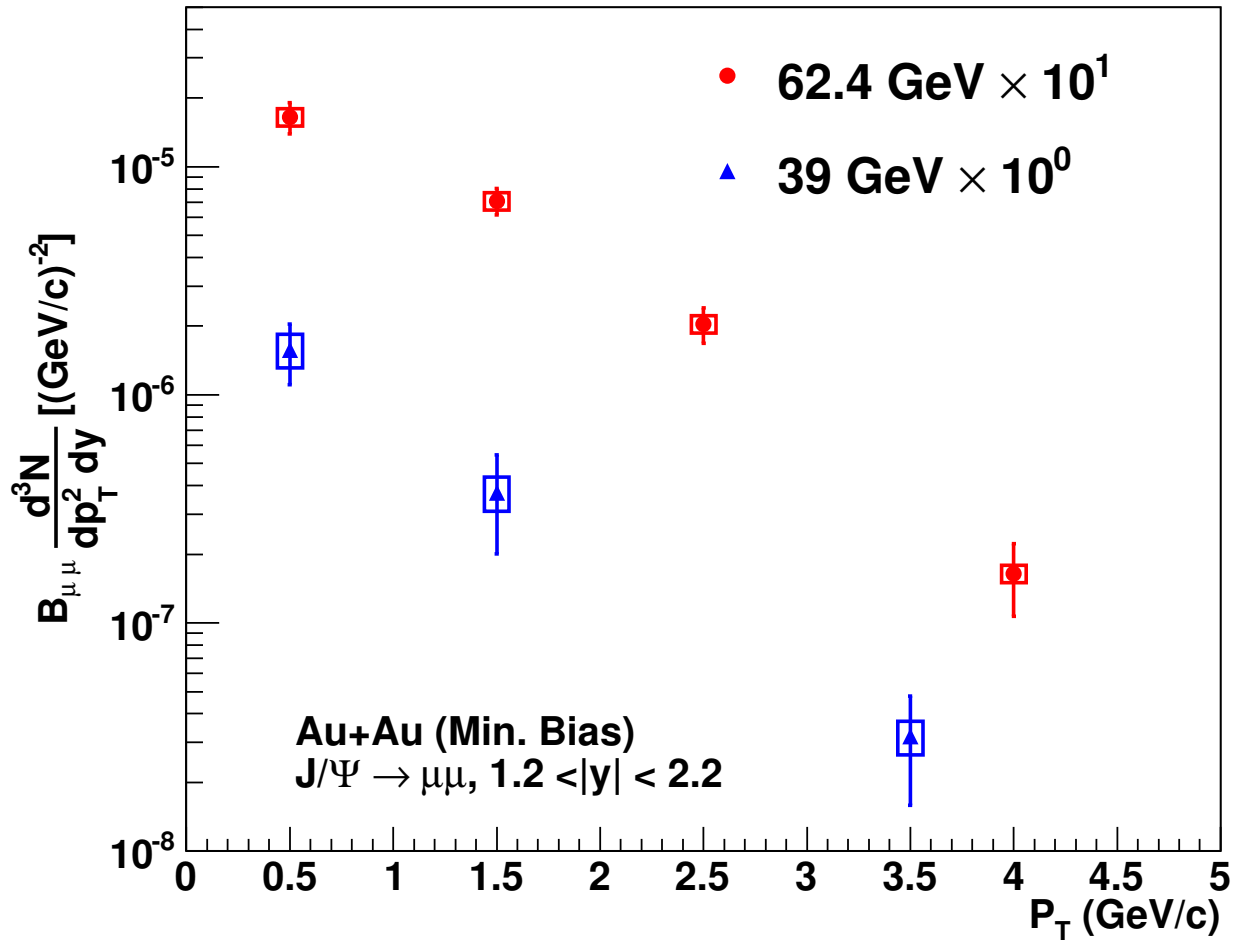
Figure 7.3: (color online) J/ψ invariant yields in minimum bias Au+Au collisions at 39 and 62.4 GeV as a function of transverse momentum. The solid error bars represent the uncorrelated point-to-point uncertainties, and the boxes represent the correlated (type B) systematic uncertainties.

show the published Au+Au results at 200 GeV [56] where the peripheral selection is 60-93%, with a quite comparable $\langle N_{\mathrm{coll}} \rangle = 14.5 \pm 2.7$. Within uncertainties, the centrality-dependent nuclear modification from peripheral to central collisions at the two energies are the same.

Table 7.10: PHENIX 39 and 62.4 GeV J/ψ R_{CP} vs Centrality with statistical uncertainties and Type A, B, and C systematics. The peripheral bins are 60-86% and 40-86% at 39 and 62.4 GeV respectively.

$\sqrt{s}(GeV)$	Cent(%)	R_{CP}	Stat	Type A	Type B	Type C
39	0-40	0.554	0.112	0.028	0.138	0.047
62.4	0-20	0.266	0.050	0.005	0.036	0.031
	20-40	0.353	0.064	0.008	0.045	0.041
	40-60	0.471	0.089	0.013	0.060	0.055

For the Au+Au results at 39 GeV, the statistics do not allow any centrality dependence of R_{CP} and only a single value is calculated for the ratio between 0-40% to 40-86% centralities, as shown in Figure 7.4 and in Table 7.10. The published Au+Au results at 200 GeV are rebined to have a peripheral centrality selection of 40-93% to approximately match the number of binary collisions for the peripheral denominator. Within uncertainties the results agree; however, the limited statistics in the Au+Au at 39 GeV preclude any strong conclusions.
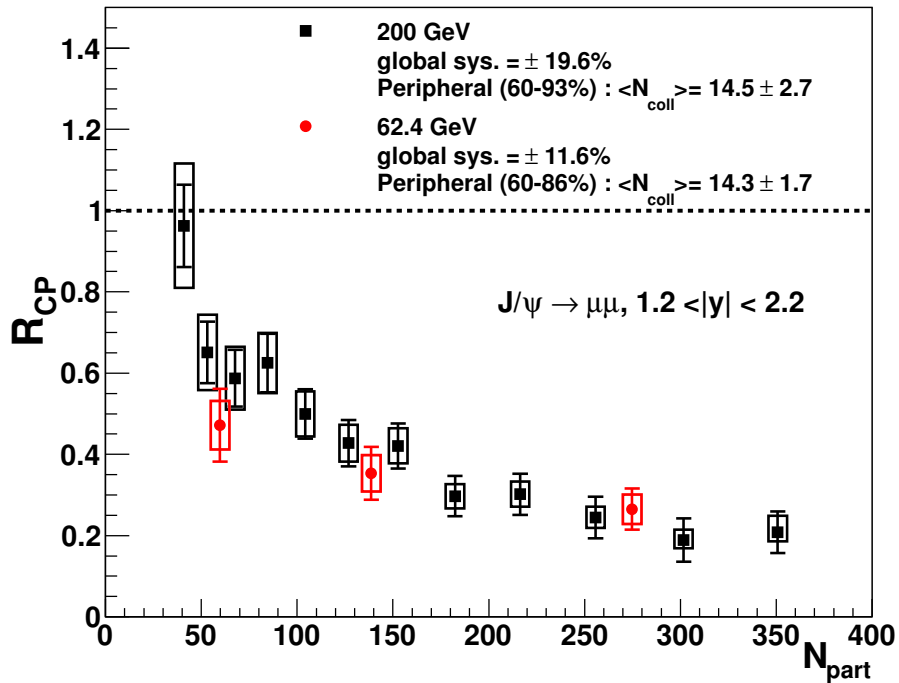
Figure 7.4: J/ψ R_{CP} for 0-20%, 20-40%, and 40-60% (central) relative to 60-86% (peripheral) Au+Au collisions at 62.4 GeV. For comparison, R_{CP} results from Au+Au collisions at 200 GeV are shown with a peripheral bin of 60-93%, where the $\langle N_{coll} \rangle$ value is a close match. The solid error bars represent the uncorrelated point-to-point uncertainties, and the boxes represent the correlated systematic uncertainties.
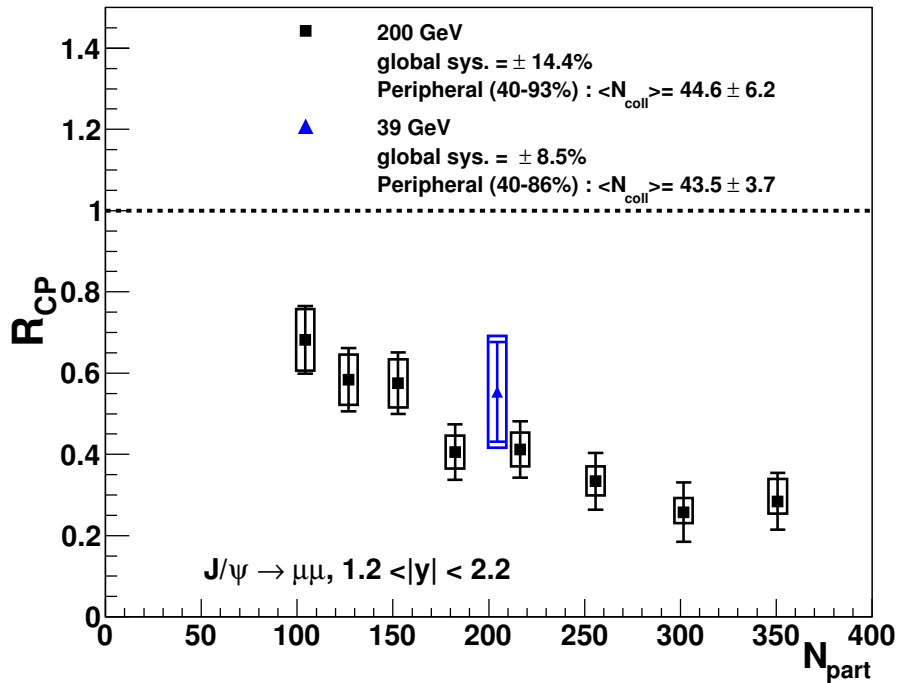
Figure 7.5: J/ψ R_{CP} for 0-40% (central) relative to 40-87% (peripheral) Au+Au collisions at 39 GeV. For comparison, R_{CP} results from Au+Au collisions at 200 GeV are shown with a peripheral bin of 40-93%, where the $\langle N_{coll}\rangle$ value is a close match. The solid error bars represent the uncorrelated point-to-point uncertainties, and the boxes represent the correlated systematic uncertainties.

CHAPTER 8

$J/\psi\ R_{AA}$

The centrality dependence as quantified via $R_{\rm CP}$ is not a replacement for nuclear modification factor $R_{\rm AA}$ (relative to the $p+p$ baseline) since J/ψ yields may change already in peripheral Au+Au collisions, in particular from cold nuclear matter effects. In addition, $R_{\rm CP}$ has significant uncertainties from the more limited statistics and the larger systematic uncertainty on $\langle N_{\rm coll} \rangle$ for the peripheral bin. The PHENIX experiment has no data for $p+p$ collisions at 39 GeV, and only a limited data set was recorded during 2006 for $p+p$ collisions at 62.4 GeV. However, $p+p$ measurements do exist from fixed target $p+A$ experiments near 39 GeV from Fermilab and from CERN's ISR collider experiments at 62.4 GeV. In the next section, we discuss in detail these results and compare them with theoretical calculations within the Color Evaporation Model (CEM) from R. Vogt [73, 74] to determine a $p+p$ reference.

8.1 Proton-Proton Reference

There has been no running of the RHIC accelerator for proton-proton collision at $\sqrt{s} = 39$ GeV. During 2006, there was a p+p running at $\sqrt{s} = 62.4$ GeV but due to low statistics no J/ψ were recorded. Therefore, the PHENIX experiment does not have data from a suitable proton-proton reference at $\sqrt{s} = 39$ or 62.4 GeV, which is needed to calculate $J/\psi\ R_{\rm AA}$. In order to construct the $p+p$ references at 39 and 62.4 GeV, lower-energy data from Fermilab and the ISR is used, in addition with the Color Evaporation Model (CEM) calculations from R. Vogt [73, 74]. After a detailed comparison of the experiential data with the theory calculations, an extrapolated cross section to PHENIX kinematic range was used as $p+p$ baselines.

8.1.1   200 GeV

First, shown in Figure 8.1 is a comparison of the published PHENIX measurements for the J/ψ cross section in $p+p$ collisions at 200 GeV [26] and the CEM calculation. For the CEM calculation, the solid line is the central value and the grey band represents the systematic uncertainty of the results. A very good agreement between the CEM with the PHENIX measurements can be seen. Using the same CEM framework, calculation results for $p+p$ collisions at 39 and 62.4 GeV are shown in Figures 8.2 and 8.3, respectively. It is notable that the predicted CEM cross section at mid-rapidity drops by approximately a factor of 2.5 in going from 200 to 62.4 GeV, and then another factor of 1.9 in going from 62.4 to 39 GeV. The rapidity distribution also narrows as expected.

Figure 8.1: J/ψ cross section as a function of rapidity in $p+p$ collisions at 200 GeV. The CEM calculation is shown as a black solid line with a grey band for its uncertainty. In comparison, PHENIX measurements are shown as red points [26].
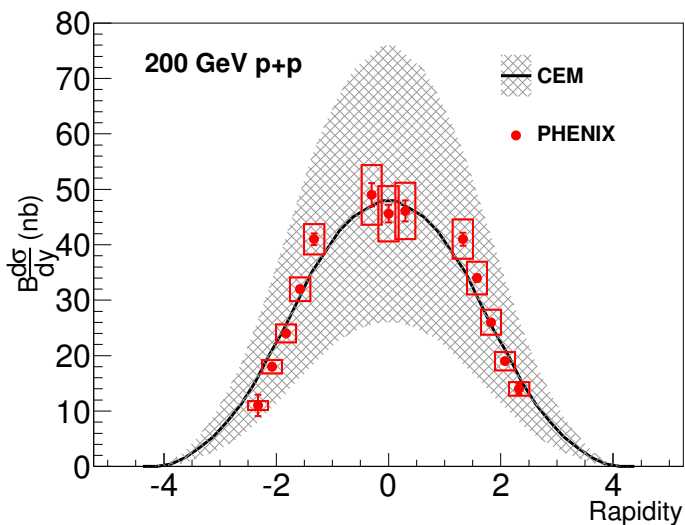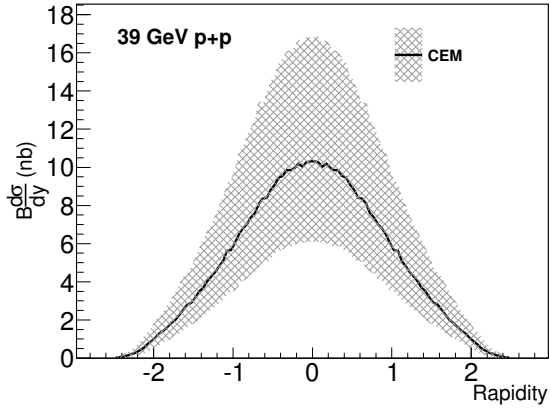
Figure 8.2: Differential cross section for J/ψ production from CEM calculations at 39 GeV [74]
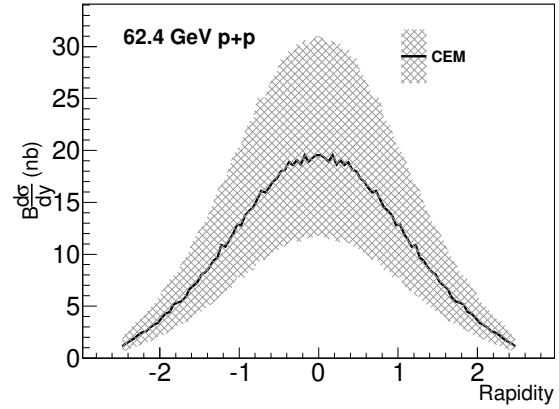
Figure 8.3: Differential cross section for J/ψ production from CEM calculations at 62.4 GeV [74].

8.1.2 39 GeV

The Fermilab fixed target experiment E789 [75, 76] has measured the invariant cross sections of J/ψ in p+Be, p+Cu, and p+Au collisions over a broad rapidity range at $\sqrt{s_{NN}} = 38.8$ GeV. The rapidity coverage for p+Au was $-0.1 < y < +0.7$; and for p+Be and p+Cu was $1.4 < y < 2.4$. The published J/ψ cross section for 39 GeV $p + A$ collisions can be seen in Fig. 8.4, where x_F is the momentum fraction [75]. The rapidity y and x_F are related by:

$$ x_F \quad = \quad \frac{M}{\sqrt{s}}(e^y - e^{-y}) \tag{8.1} $$

The solid curve on Fig. 8.4 shows a fit to the combined data using a functional form $A(1 - |x_F|)^B$ with $A = 158 \pm 32$ μb and $B = 5.09 \pm 0.17$. In addition, the nuclear dependence of the cross sections was measured by E866/NuSea [52] experiment at Fermilab and found to follow the functional form, $\sigma_{p+A} = A^\alpha \sigma_{p+p}$, where α is the nuclear modification in $p + A$ collisions compared to the atomic number scaled p+p cross section and shown in Fig. 8.5.
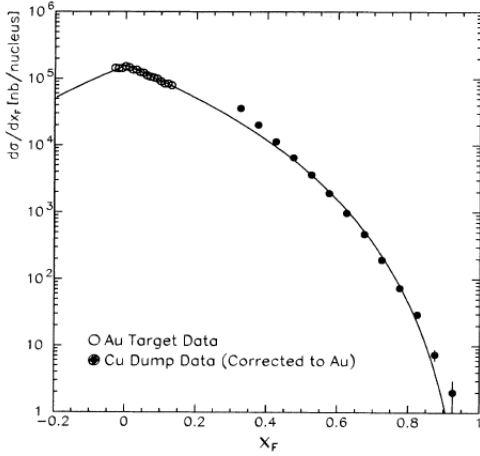
Figure 8.4: Differential cross section for J/ψ production vs x_F. The solid curve is a fit to the data using the functional form $A(1 - |x_F|)^B$ [52].
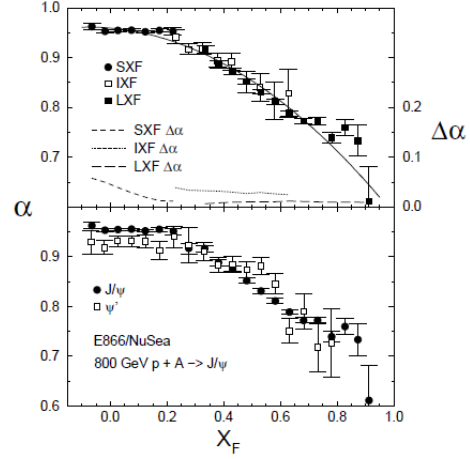
Figure 8.5: Nuclear modification (α) for the J/ψ and ψ' vs x_F. $\Delta\alpha$ is the correction for the p_{T} acceptance. Solid curve represents the parametrization discussed in the text [76].

The fitted solid curve on Fig. 8.5 can be written as:

$$\alpha(x_F) = 0.960(1 - 0.0519x_F - 0.338x_F^2) \tag{8.2}$$

Using this parametrization for the nuclear dependence, one can extrapolate versus A from the $p+A$ J/ψ cross sections to those for $p+p$ ($A = 1$) and obtain the $p+p$ cross sections as a function of x_F. The extrapolated $p+p$ cross section ($d\sigma/dx_F$) can further converted to ($d\sigma/dy$) as follows:

$$\frac{d\sigma}{dy} = \frac{d\sigma}{dx_F} \times \frac{dx_F}{dy} \tag{8.3}$$

$$\frac{dx_F}{dy} = \frac{M}{\sqrt{s}}(e^y + e^{-y}) \tag{8.4}$$

Fig. 8.6 shows the extrapolated $p+p$ cross section at 39 GeV from Fermilab measurements along with CEM calculations. For the rapidity range $1.2 < y < 2.2$ one obtains
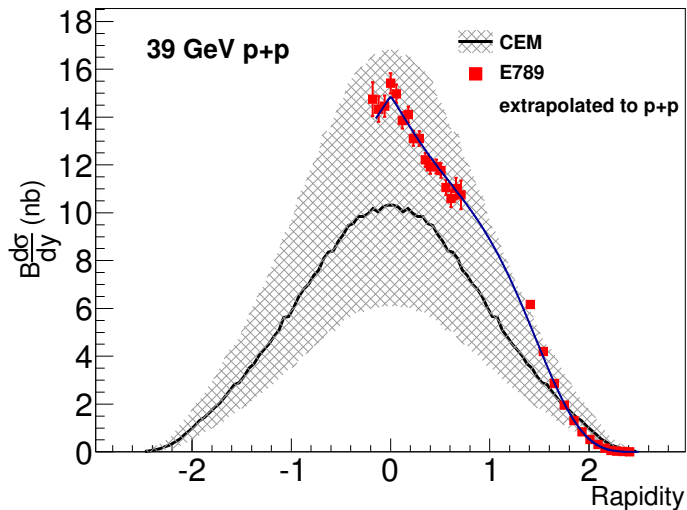
Figure 8.6: 39 GeV p+p reference. Solid black lines are from CEM, data points are Fermilab measurements.

$2.91 \pm 19\%$(sys) nb by integrating the fit function. In comparison, the result from the CEM calculation is $2.45^{+1.78}_{-1.0}$ nb, which agrees well within uncertainties. Thus, we use this extraction from the experimental data for the 39 GeV $p+p$ reference, as shown in Table 8.2. Systematic uncertainties on this reference include 12% from the E789 $p + A$ data and 15% to account for the quality of the fit and for its extrapolation in rapidity into the unmeasured $1.2 < y < 1.4$ region.

8.1.3 62.4 GeV

Experiments at the CERN Intersecting Storage Ring (ISR) measured the J/ψ cross section in $p+p$ collisions at 62.4 GeV [77, 78, 79]. These results are shown in Table 8.1 and in comparison to the CEM calculation in Figure 8.7. Since our measurements lie in the rapidity range $1.2 < |y| < 2.2$, the most important p+p measurement from the ISR for our purposes is that of Antreasyan [77], which covers a rapidity range of $0.89 < y < 1.82$ and agrees quite well with the CEM calculation. Therefore we estimate the p+p reference by integrating over our rapidity coverage using the CEM calculation fitted to the Antreasyan

measurement. For the uncertainties of this reference we take similar CEM guided integrals, but constrained to the upper and to the lower limits of the ISR measurement. This results in a 62.4 GeV $p+p$ reference of $7.66 \pm 29.4\%$ nb. We note that the mid-rapidity ISR points are somewhat low but nearly consistent with the CEM calculation, but since our data lies at large rapidity we rely on the Antreasyan ISR point. A summary of the cross sections extrapolated at 39 and 62.4 GeV is given in Table 8.2.

Table 8.1: ISR Measurements of J/ψ in p+p collisions

Reference	Rapidity Range	$< p_T >$	$B_{ee}\frac{d\sigma}{dy}$(nb)
[77]	$0.89 < y < 1.82$	-	9.21 ± 2.70 nb
[78]	$|y| <$0.5	1.1 ± 0.5 GeV/c	10.2 ± 0.7 nb
[79]	$|y| <$0.65	1.29 ± 0.05 GeV/c	14.8 ± 3.3 nb
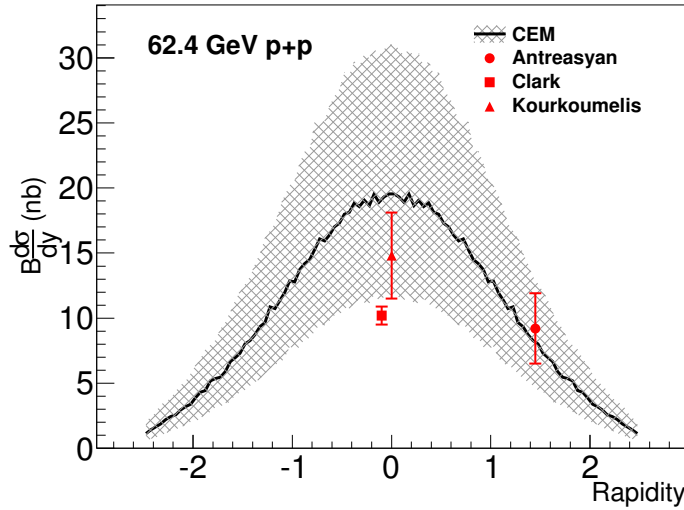
Figure 8.7: 62.4 GeV p+p reference. Solid black lines are from CEM, data points are ISR measurements. The legends represents the references Antreasyan [77], Clark [78] and Kourkoumelis [79].

Table 8.2:   Estimates used for the 39 and 62.4 GeV J/ψ $p+p$ cross sections along with their uncertainties.

$\sqrt{s}(GeV)$	$d\sigma^{pp}/dy$
39	$2.91 \pm 19\%$ nb
62.4	$7.66 \pm 29.4\%$ nb

8.2 R_{AA} Calculations

We quantify the nuclear modification factor R_{AA} with respect to the $p+p$ reference as follows:

$$R_{\mathrm{AA}} = \frac{1}{\langle T_{\mathrm{AA}} \rangle} \frac{dN^{AA}/dy}{d\sigma^{pp}/dy} \tag{8.5}$$

where dN^{AA}/dy is the invariant yield in Au+Au collisions, $d\sigma^{pp}/dy$ is the $p+p$ cross section, and $\langle T_{\mathrm{AA}} \rangle$ is the nuclear overlap function (where $\langle T_{\mathrm{AA}} \rangle = \langle N_{\mathrm{coll}} \rangle / \sigma_{NN}^{inelastic}$). Unlike 200 GeV, the 39 and 62.4 GeV $p+p$ references are determined from other measurements rather than being from our own, and systematic uncertainties will not cancel in the ratio. Our estimates for the J/ψ $p+p$ cross sections in the range $1.2 < |y| < 2.2$ for 39 and 62.4 GeV are shown in Table 8.2, and are detailed in the previous section. At both 39 and 62.4 GeV, there is slightly less J/ψ suppression than observed in Au+Au at 200 GeV. However, particularly for 62.4 GeV, since we have no reliable $p+p$ reference from our own measurements, the R_{AA} result could shift down by the quoted 29% systematic uncertainty, bringing the data into agreement with the 200 GeV result.

Table 8.3: PHENIX 39 and 62.4 GeV J/ψ R_{AA} vs Centrality with statistical uncertainties and Type A, B and C systematics.

$\sqrt{s}(GeV)$	Cent(%)	R_{AA}	Stat	Type A	Type B	Type C
39	0-40	0.439	0.043	0.020	0.077	0.083
	40-86	0.793	0.157	0.011	0.139	0.151
62.4	0-20	0.292	0.039	0.004	0.042	0.085
	20-40	0.388	0.047	0.008	0.056	0.115
	40-60	0.519	0.067	0.014	0.073	0.153
	60-86	1.100	0.150	0.010	0.155	0.323
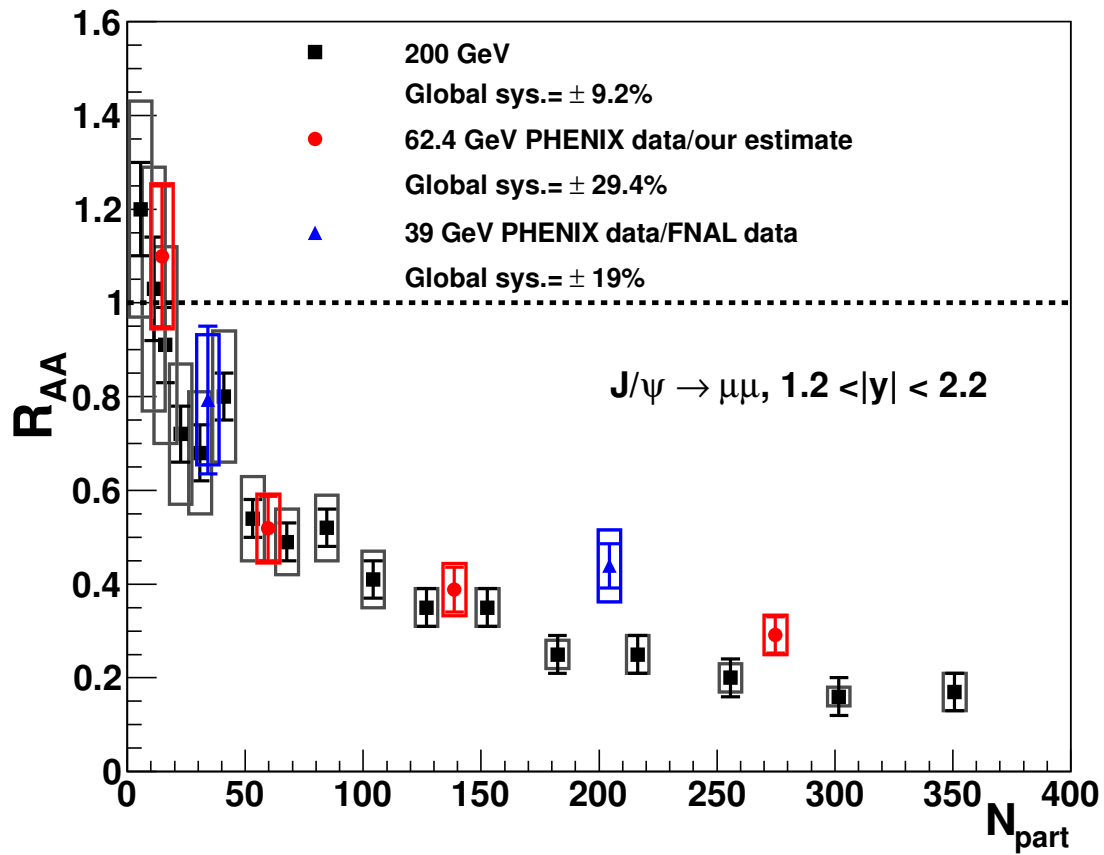
Figure 8.8: J/Ψ R_{AA} at 39, 62.4 and 200 GeV

CHAPTER 9

DISCUSSION

The collision energy dependence of the various competing effects influencing the final J/ψ yields are all quite different. Thus, the similarity of the J/ψ nuclear modifications R_{CP} and R_{AA} from 39 to 200 GeV is a challenge for models incorporating the many effects. There was a prediction that the maximum J/ψ suppression would occur near $\sqrt{s_{NN}} = 50$ GeV, as shown in Figure 9.1 [80]. As the collision energy increases the QGP temperature increases, and thus the J/ψ color screening (labeled as direct J/ψ suppression) becomes more significant. However, in this calculation, the regeneration contribution increases with collision energy due to the increase in the total number of charm pairs produced and nearly compensates. This result is for J/ψ at mid-rapidity and relative to the total charm pair production (thus removing in this ratio possible changes in the charm pair production caused by initial state effects).

Recently, the same authors have completed new calculations including cold nuclear matter effects, regeneration, and QGP suppression specifically for J/ψ at forward rapidity [81, 82]. These results (in the so-called "strong binding scenario") are shown in Figure 9.2 with the contributions of direct J/ψ and regeneration shown separately (and scaled down by $\times 0.5$ for visual clarity). The inclusion of cold nuclear matter effects and the forward-rapidity kinematics slightly reverse the trend seen in Figure 9.1 and now the total J/ψ R_{AA} follows the ordering $R_{AA}(200 \text{ GeV}) < R_{AA}(62.4 \text{ GeV}) < R_{AA}(39 \text{ GeV})$ (though by a very modest amount). Also shown in Figure 9.2 are the PHENIX experimental measurements that, within the global systematic uncertainties, are consistent with the theoretical calculations.

These results highlight the need for $p+p$ reference data at both 39 and 62.4 GeV from the same experiment. In addition, the cold nuclear matter effects are likely to be different at the different energies (an important input for the calculations in Ref. [81]). The x distribution
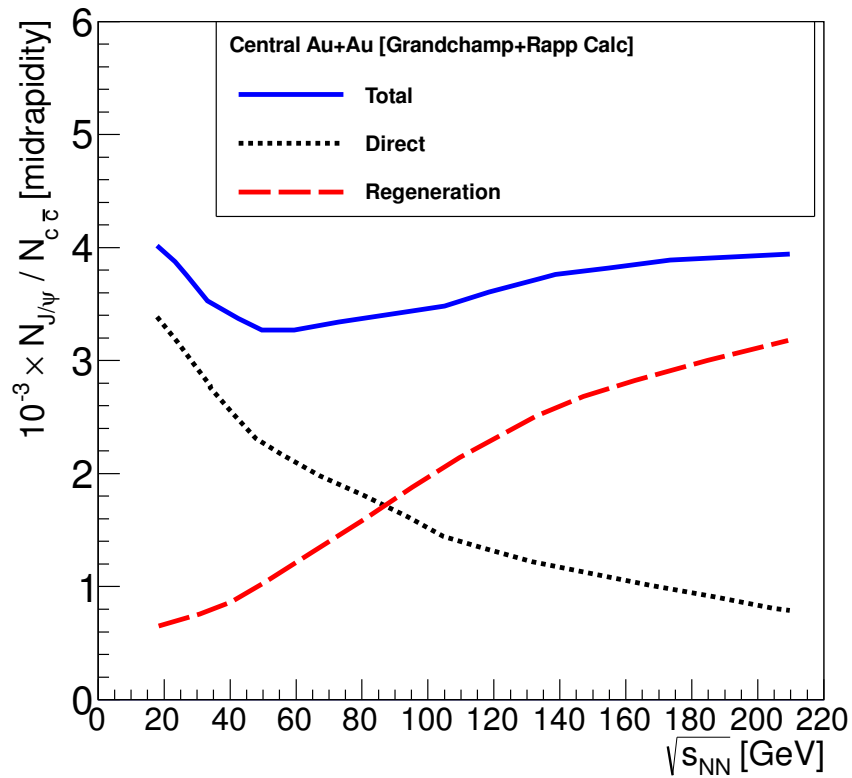
Figure 9.1: (color online) The number of J/ψ per produced charm pair ($\times 10^{-3}$) in Au+Au central collisions ($N_{\mathrm{part}} = 360$) at mid-rapidity. Shown are the direct J/ψ and regeneration contributions. Calculation details and figure from [80].
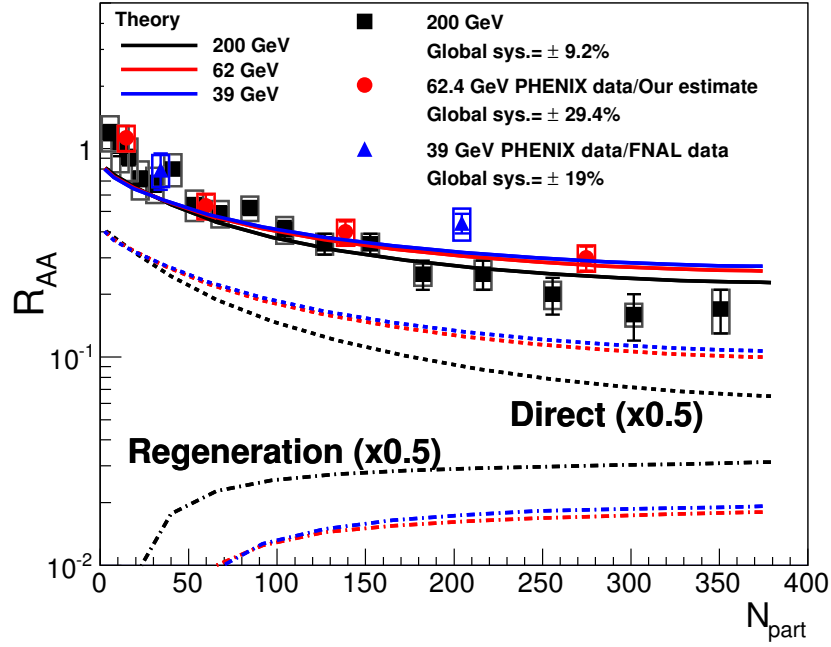
Figure 9.2: (color online) The J/ψ nuclear modification factor R_{AA} as a function of the number of participating nucleons N_{part} for $\sqrt{s_{NN}} = 39$, 62.4, 200 GeV Au+Au collisions. Calculation results are shown from [81] for the total J/ψ R_{AA} and the separate contribution of direct J/ψ suppression and regeneration (scaled down by $\times 0.5$ for visual clarity). The PHENIX experimental data points are shown for comparison.

of gluons for producing J/ψ at $1.2 < |y| < 2.2$ changes as the colliding energy decreases. In a simple PYTHIA study, one finds that the average gluon x_1 and x_2 for producing J/ψ between $1.2 < |y| < 2.2$ is 0.14 and 0.01 for $\sqrt{s_{NN}} = 200$ GeV, 0.32 and 0.03 for $\sqrt{s_{NN}} = 62.4$ GeV, and 0.43 and 0.05 for $\sqrt{s_{NN}} = 39$ GeV. The large uncertainties in the gluon nPDF for the anti-shadowing and EMC regions [30] leads to an additional $\pm 30\%$ uncertainty in the J/ψ initial production for the central Au+Au case. Future measurements in $p(d)+A$ collisons at these energies are clearly required in order to reduce this large uncertainty contribution.

9.1   Summary

The PHENIX experiment has measured the invariant yield of J/ψ at forward rapidity in Au+Au collisions at 39 and 62.4 GeV [83]. The nuclear modification, when formulated as R_{CP} (the ratio between central and peripheral event classes), indicates a similar suppression pattern at the two lower energies to that previously published for Au+Au collisions at 200 GeV. Using a $p+p$ reference from other experiments and from a Color Evaporation Model calculation, results in an R_{AA} with slightly less suppression at these lower energies. These results are consistent with theoretical calculations dominated by the balancing effects of more QGP suppression as well as more J/ψ regeneration for high-energy collisions. However, any firm conclusion regarding the overall level of suppression from the QGP requires additional $p+p$ and $p(d)+A$ data at these energies.

Appendix A

KINEMATIC VARIABLES

A.1 Transverse Momentum

Coordinate systems as defined by PHENIX is in Fig. A.1. The beam going direction is the z-axis. The transverse momentum p_{T} and, the transverse mass m_T are defined in terms of energy momentum components of the particle.

$$p_{\mathrm{T}} = \sqrt{p_x^2 + p_y^2}, \tag{A.1}$$

$$m_T = \sqrt{m^2 + p_T^2} = \sqrt{E^2 - P_z^2}, \tag{A.2}$$

where E, p_x, p_y, p_z and m are the energy, x,y,z components of the momentum and mass respectively.
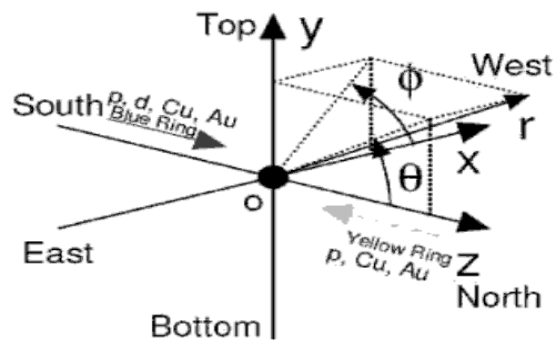
Figure A.1: PHENIX coordinates.
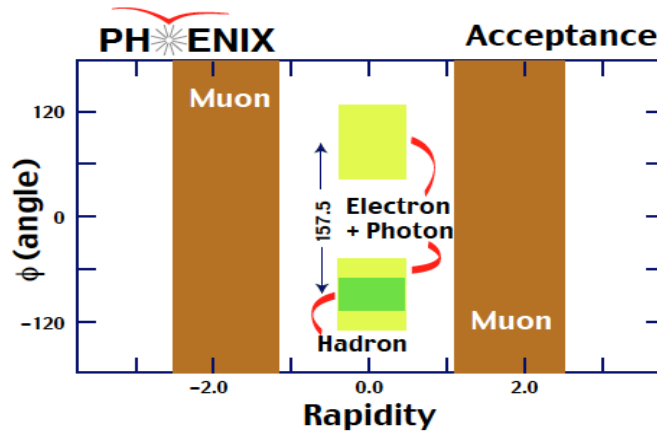
Figure A.2: PHENIX rapidity acceptance.

A.2 Rapidity

The rapidity y of a particle is defined by:

$$y = \frac{1}{2}\ln\left(\frac{E - p_z}{E + p_z}\right) \tag{A.3}$$

Fig. A.2 shows the PHENIX acceptance over rapidity and ϕ angle. The muon arms cover full azimuthal acceptance over $-2.25 < y < -1.15$ for the south arm and $1.15 < y < 2.44$ for the north arm. The particle's energy and the z component of the momentum can be written in terms of the rapidity as follows:

$$E = m_T\cosh y \tag{A.4}$$

$$p_z = m_T\sinh y \tag{A.5}$$

The pseudo rapidity, η can be expressed in terms of angle θ, between the particle momentum, p and z axis.

$$\eta = \frac{1}{2}\ln\left(\frac{|\vec{p}| + p_z}{|\vec{p}| - p_z}\right) = -\ln\left(tan\left(\frac{\theta}{2}\right)\right) \tag{A.6}$$

Appendix B

QUALITY ASSURANCE

B.1   62.4 GeV

The global QA for the Run10 62.4 GeV Au+Au data set was done by Xiaoyang Gong, which is summarized in the PHENIX analysis note 940 [84]. The global QA checks include:

- Number of events in each segment.

- BBC-z distribution.

- flatness of centrality distribution.

Analysis note 940 concludes that runs 311990, 311991, 312371 and 312891 are not good for physics analysis, because

- Run 311990 and 311991 have severely shifted BBC-z distribution.

- Run 312371 has too few events.

- Run 312891 has a non-flat centrality distribution.

The cluster charge distribution was fitted with a Landau function. The Landau peak and sigma are shown in Figs. B.1, B.2 at 62.4 GeV and Figs. B.4, B.5 at 39 GeV for the south arm and the north arm, respectively.

QA conclusions for the 62.4 GeV data set:

- Bad runlist for south: 311990,311991,312891 (global QA) and 312939 (bad HV).

- Bad runlist for north: 311990, 311991,312891 (global QA) and 310723, 312900 (dead planes, same were bad in landau distributions).

- Remark: 312371 was rejected in AN940 because of fewer events but good in muon arm. So we decided to keep this run.
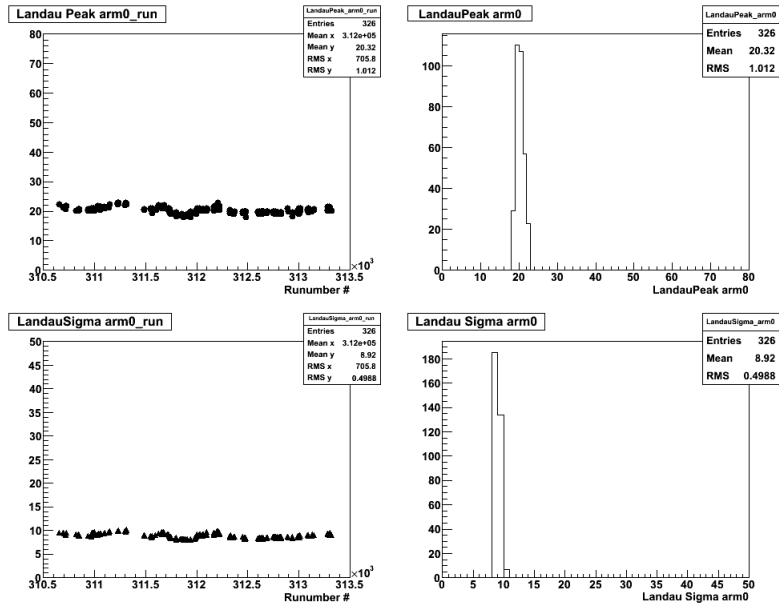
Figure B.1: Landau fit results of the cluster charge distribution from the south arm as a function of run number (62.4 GeV).
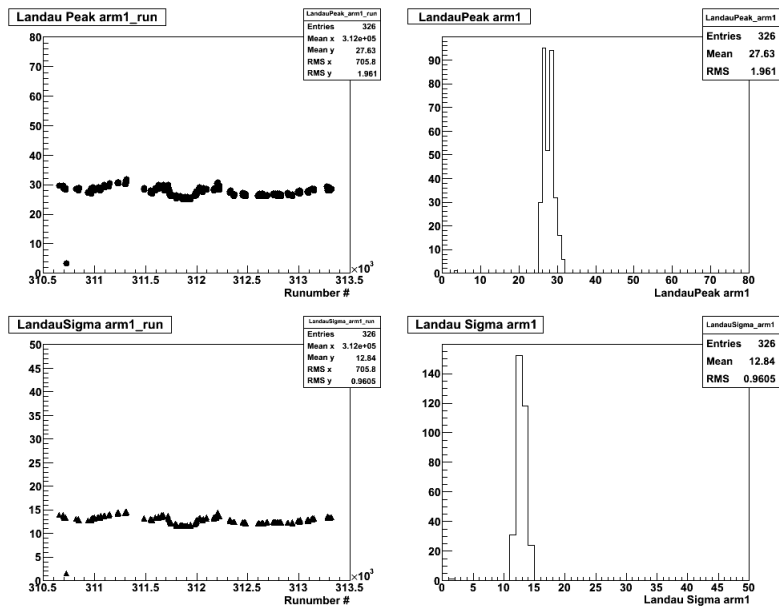
Figure B.2: Landau fit results of the cluster charge distribution from the north arm as a function of run number (62.4 GeV).
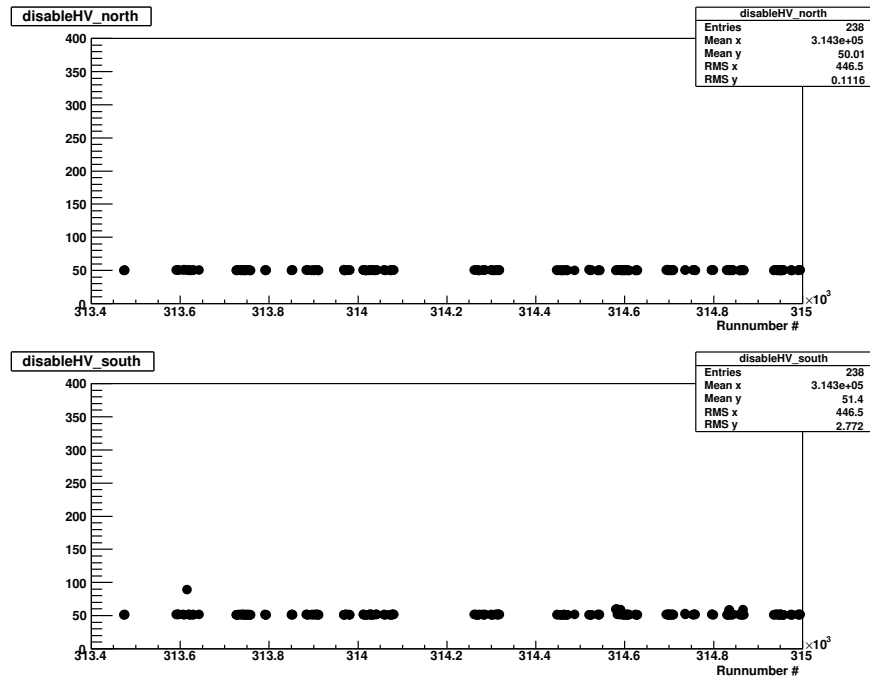
Figure B.3: Number of disabled HV channels both in north (top) and south (bottom) arm (39 GeV).

B.2 39 GeV

PHENIX analysis note 940 concludes that run 314025, 314026, 314033 and 314034 are not good for physics analysis, because their BBC-z distribution widths are too large.

QA conclusions for the 39 GeV data set:

- Bad runlist for south: 314025, 314026, 314033 and 314034 (global QA).

- Bad runlist for north: 314025, 314026, 314033 and 314034 (global QA).

- Remark: We did not find anything unusual in muon QA. So we decided to use the global QA conclusions.
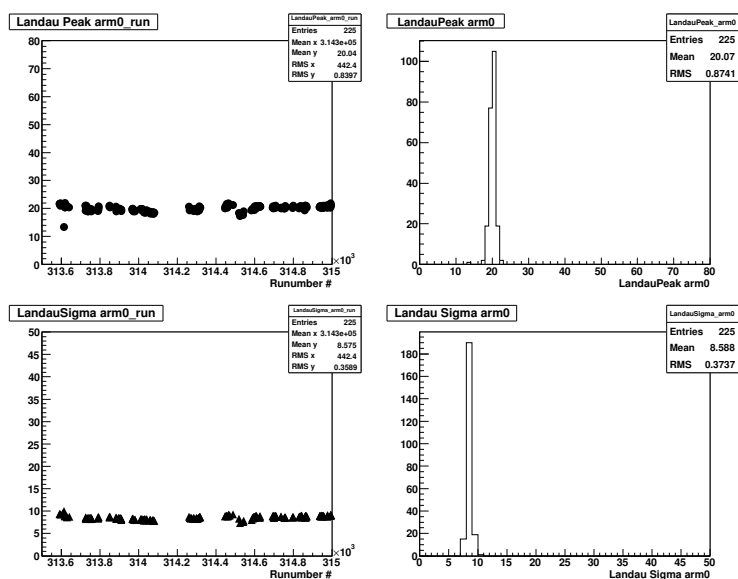
Figure B.4: Landau fit results of the cluster charge distribution from the south arm as a function of run number (39 GeV).
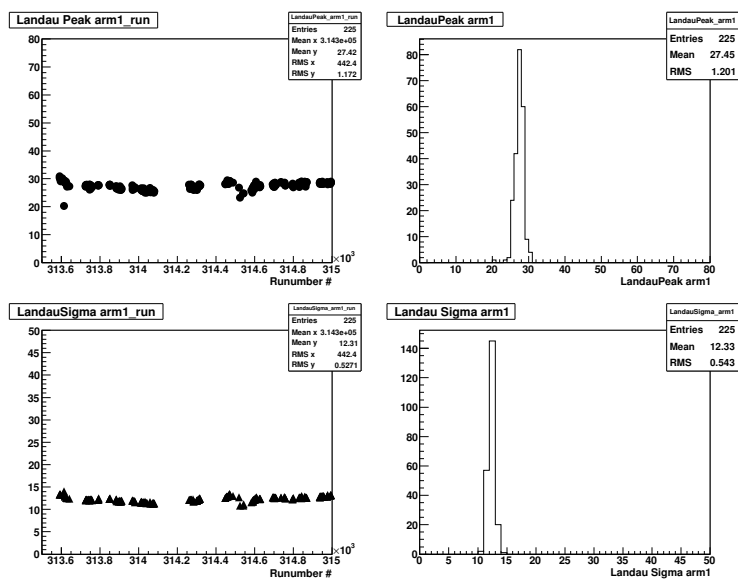
Figure B.5: Landau fit results of the cluster charge distribution from the north arm as a function of run number (39 GeV).

Appendix C

DIMUON MASS FITS
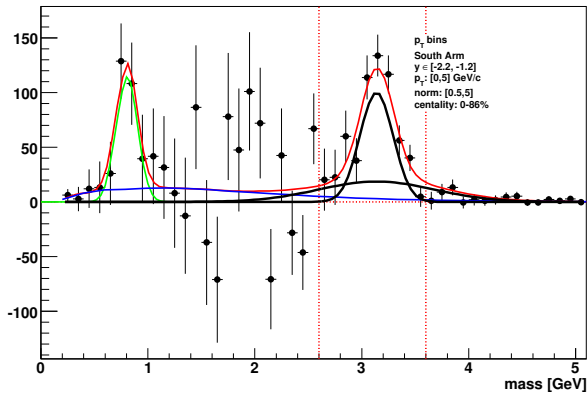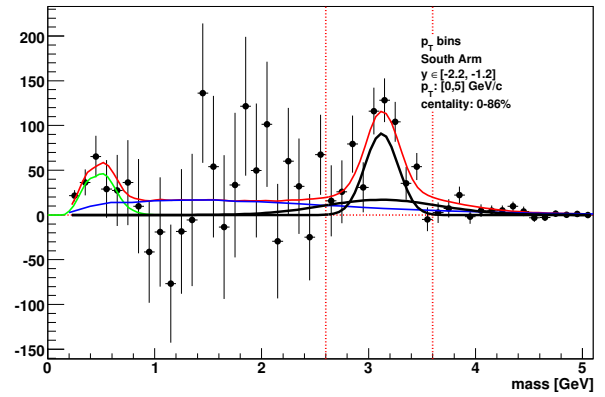
Mixed Subtraction   **LikeSign Subtraction**

Figure C.1: 62.4 GeV dimuon spectrum in south arm for p_T [0-5] GeV/c for all centrality.
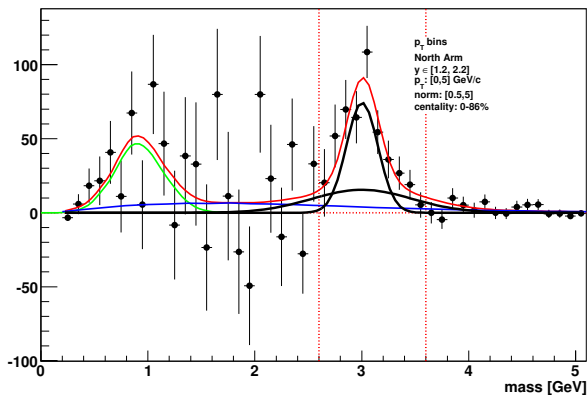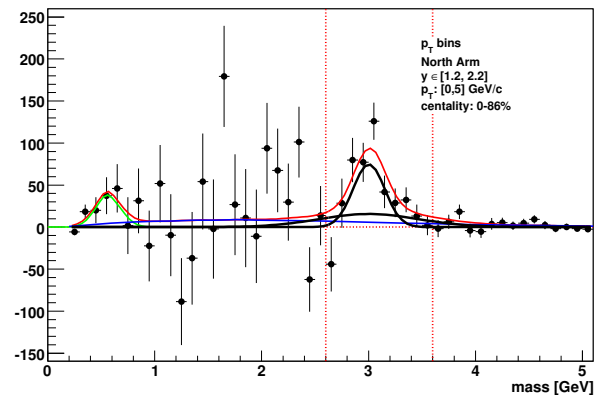
Mixed Subtraction   **LikeSign Subtraction**

Figure C.2: 62.4 GeV dimuon spectrum in north arm for p_T [0-5] GeV/c for all centrality.
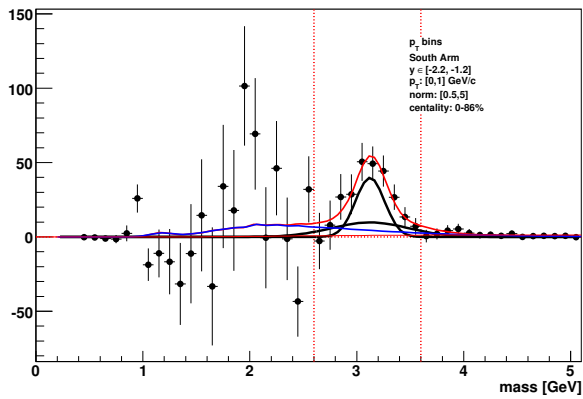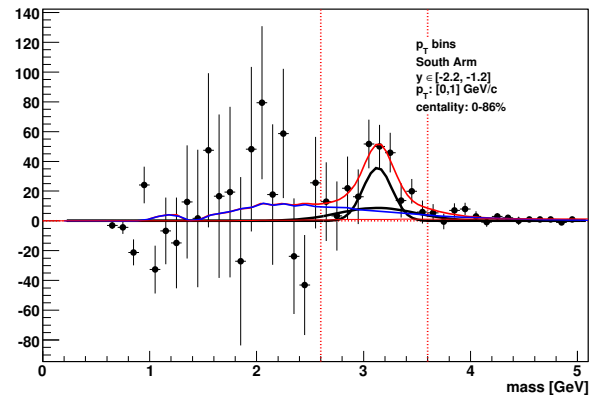
Mixed Subtraction **LikeSign Subtraction**

Figure C.3: 62.4 GeV dimuon spectrum in south arm for p_T [0-1] GeV/c for all centrality.
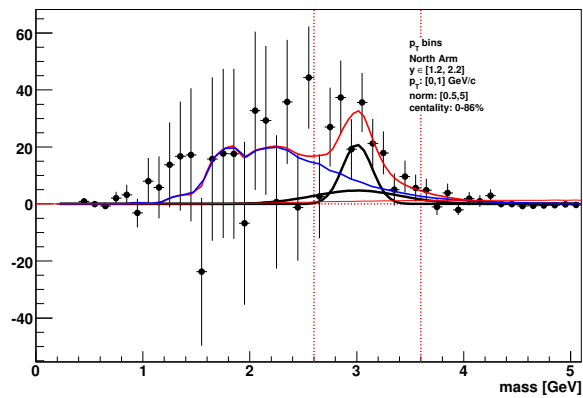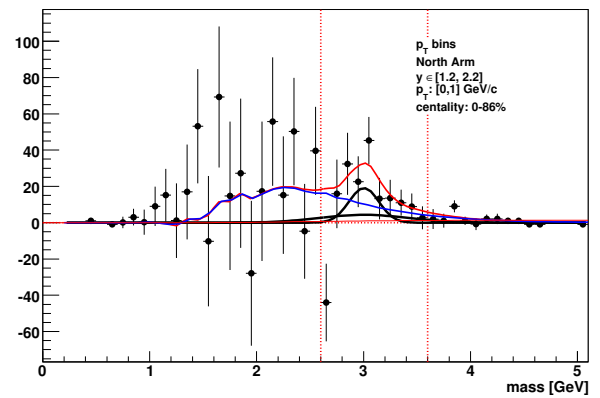
Mixed Subtraction **LikeSign Subtraction**

Figure C.4: 62.4 GeV dimuon spectrum in north arm for p_T [0-1] GeV/c for all centrality.
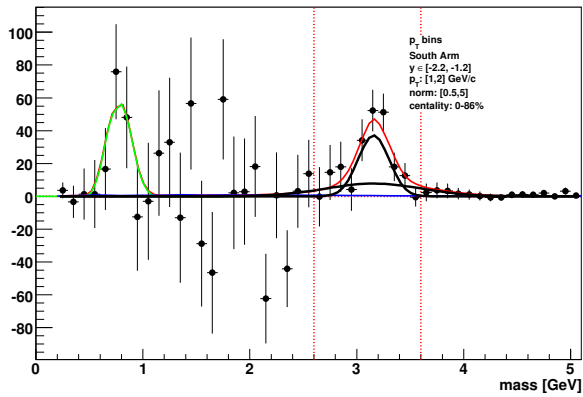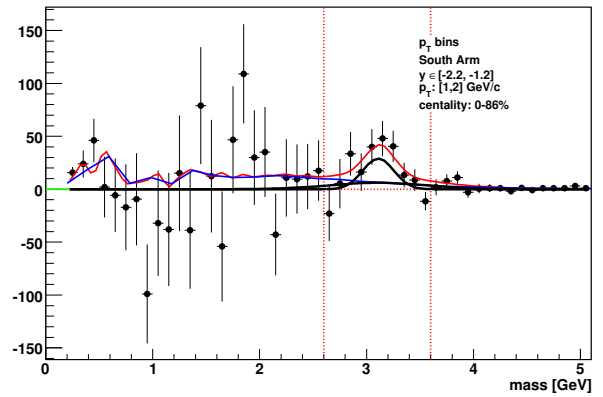
Mixed Subtraction **LikeSign Subtraction**

Figure C.5: 62.4 GeV dimuon spectrum in south arm for $p_T[1\text{-}2]$GeV/c for all centrality.
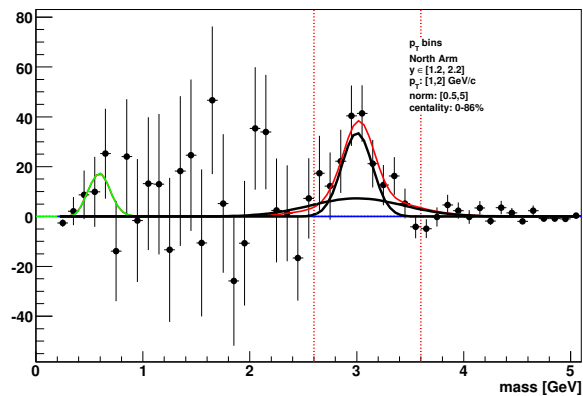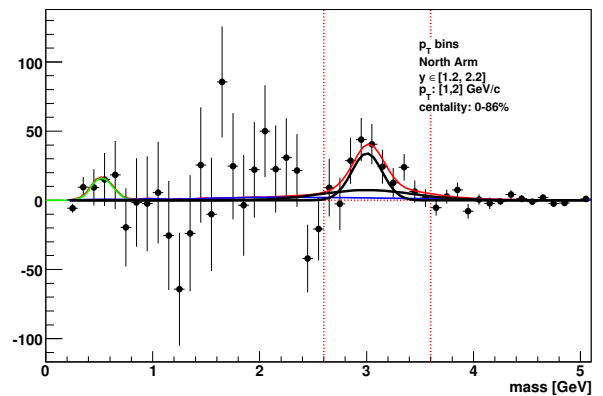
Mixed Subtraction **LikeSign Subtraction**

Figure C.6: 62.4 GeV dimuon spectrum in north arm for p_T [1-2] GeV/c for all centrality.
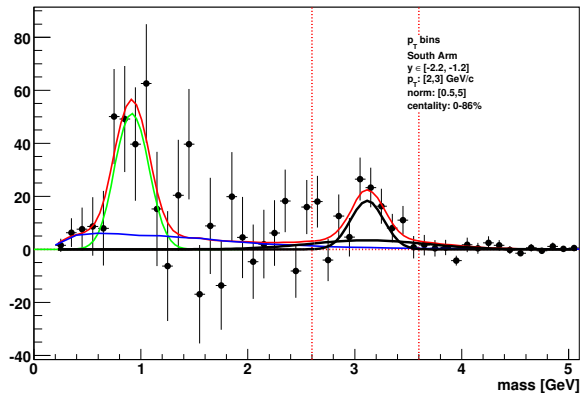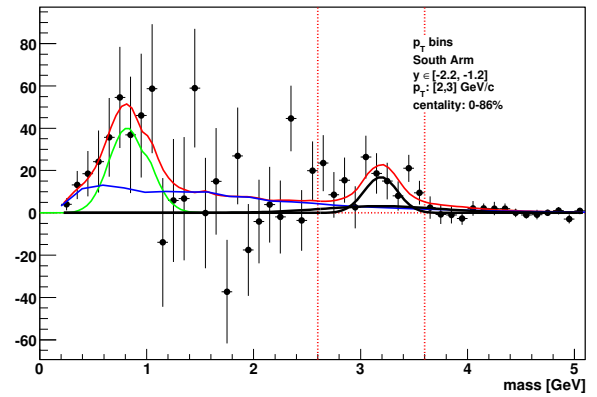
| Mixed Subtraction | LikeSign Subtraction |

Figure C.7: 62.4 GeV dimuon spectrum in south arm for p_T [2-3] GeV/c for all centrality.
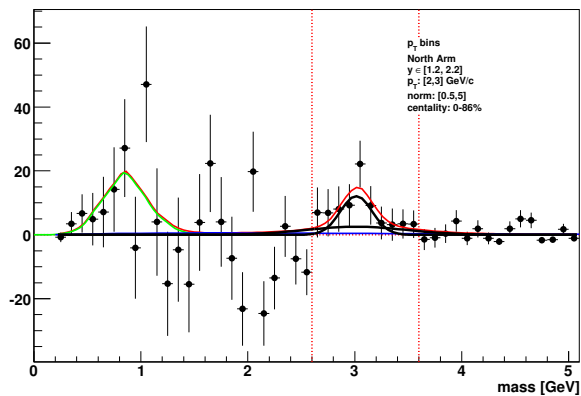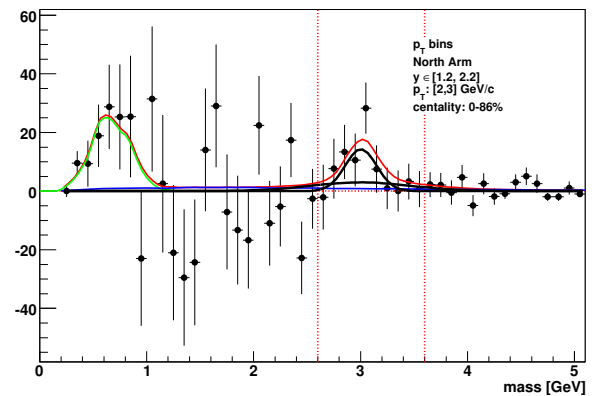
| Mixed Subtraction | LikeSign Subtraction |

Figure C.8: 62.4 GeV dimuon spectrum in north arm for p_T [2-3] GeV/c for all centrality.
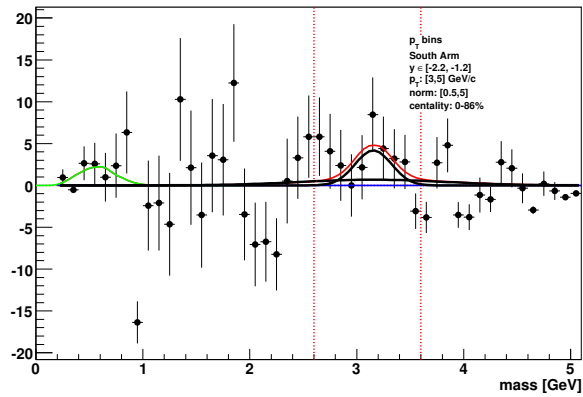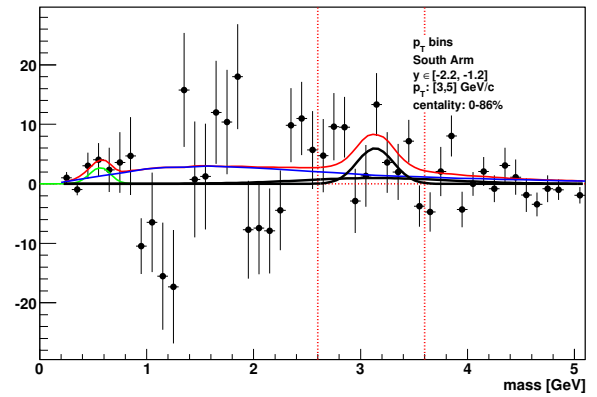
Mixed Subtraction   **LikeSign Subtraction**

Figure C.9: 62.4 GeV dimuon spectrum in south arm for p_T [3-5] GeV/c for all centrality.
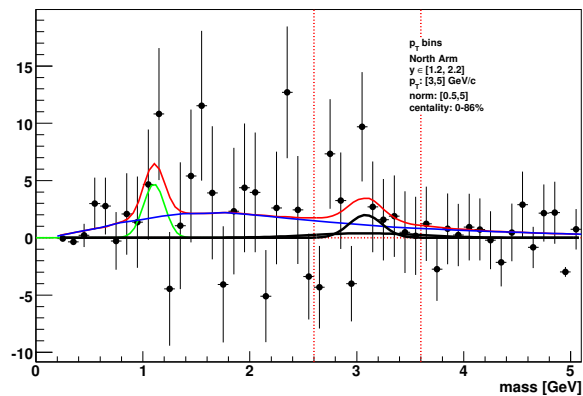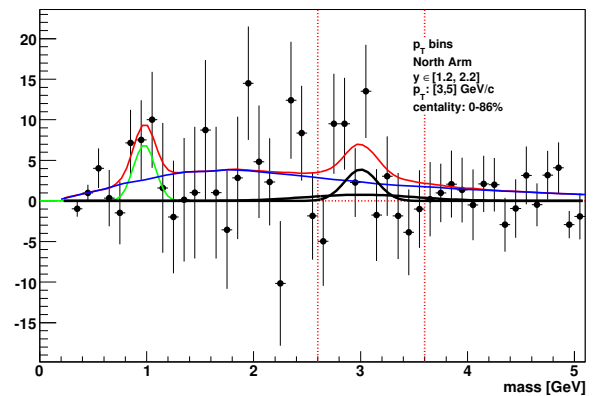
Mixed Subtraction   **LikeSign Subtraction**

Figure C.10: 62.4 GeV dimuon spectrum in north arm for p_T [3-5] GeV/c for all centrality.
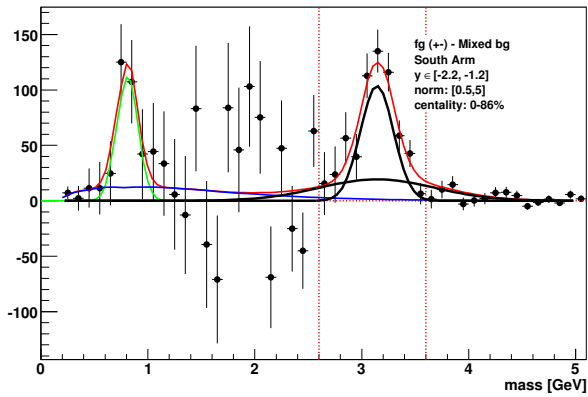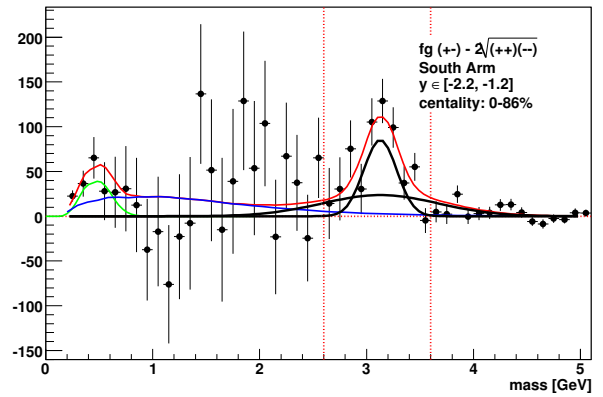
Mixed Subtraction   **LikeSign Subtraction**

Figure C.11: 62.4 GeV dimuon spectrum in south arm for pT integrated centrality [0-100].
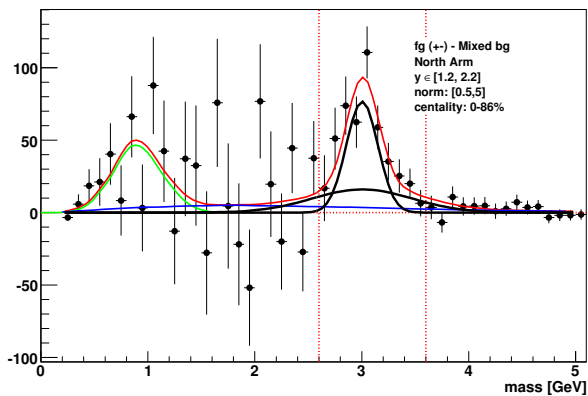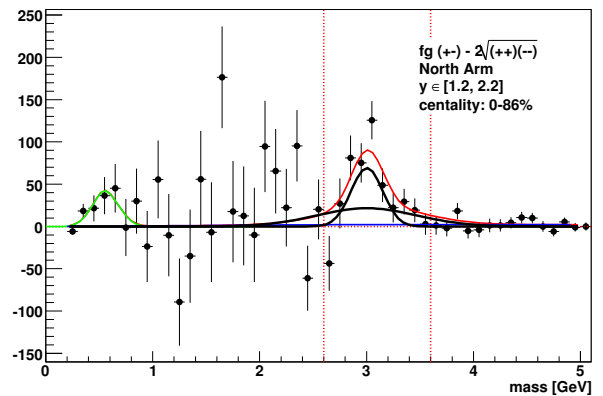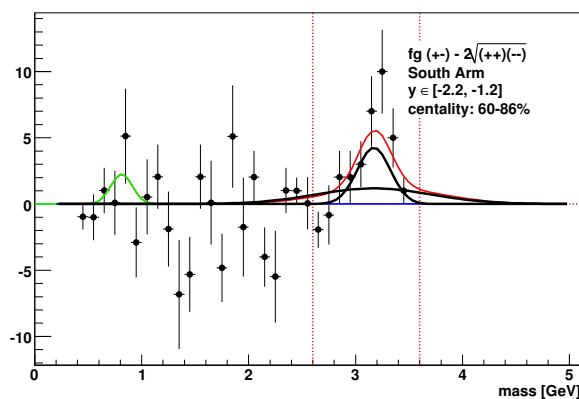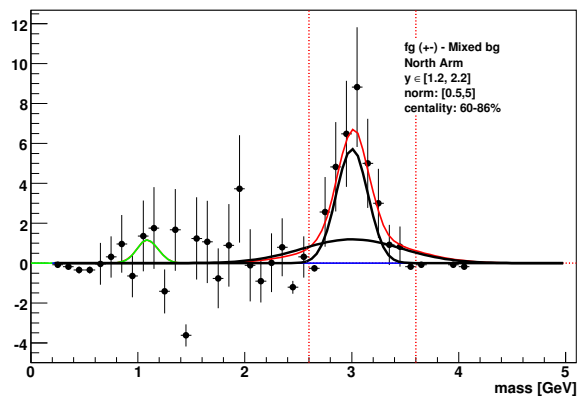

Mixed Subtraction   **LikeSign Subtraction**

Figure C.12: 62.4 GeV dimuon spectrum in north arm for pT integrated centrality [0-100].
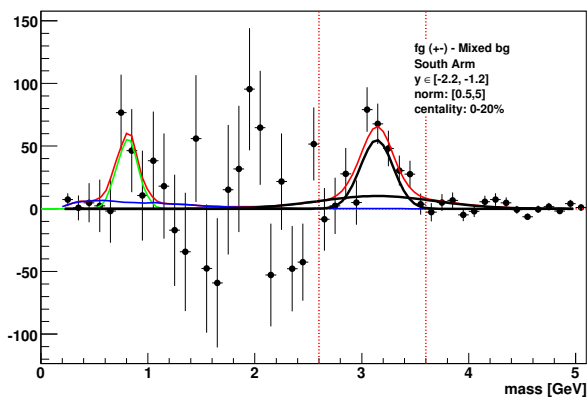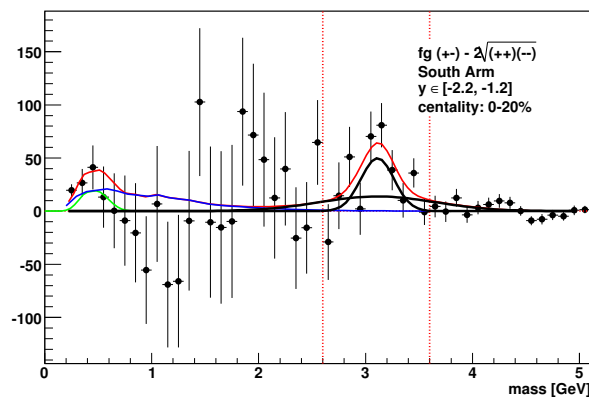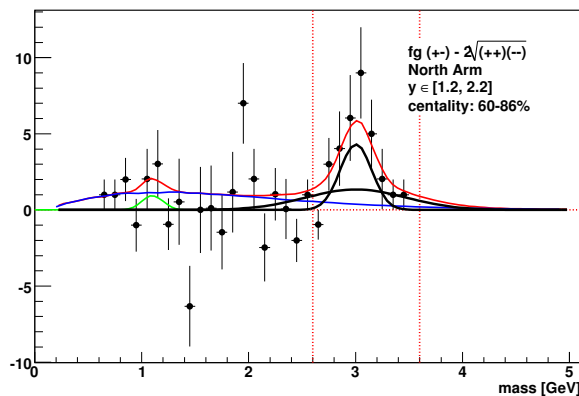
Mixed Subtraction   **LikeSign Subtraction**

Figure C.13: 62.4 GeV dimuon spectrum in south arm for pT integrated centrality [0-20].
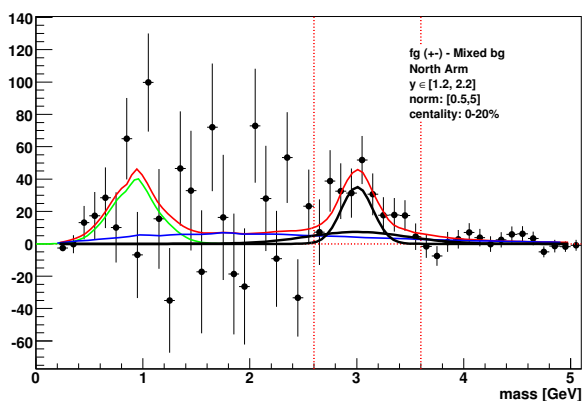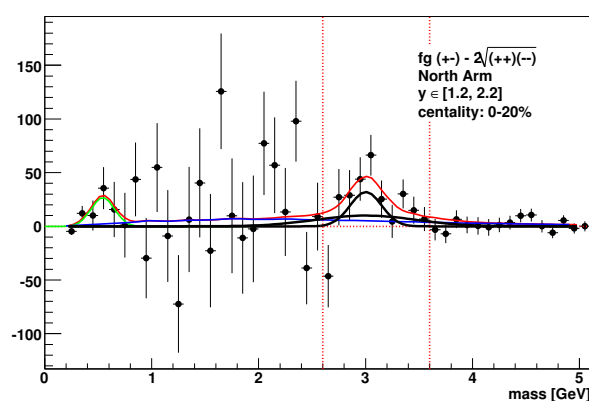
Mixed Subtraction   **LikeSign Subtraction**

Figure C.14: 62.4 GeV dimuon spectrum in north arm for pT integrated centrality [0-20].
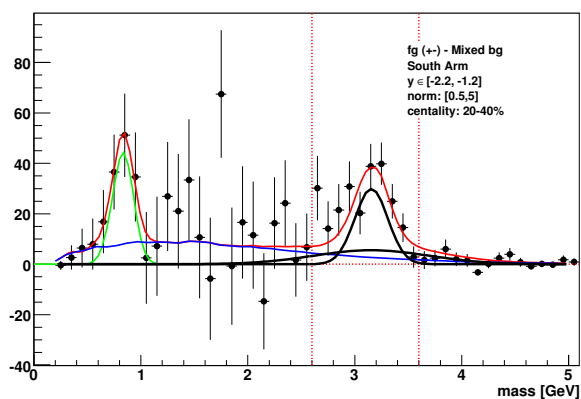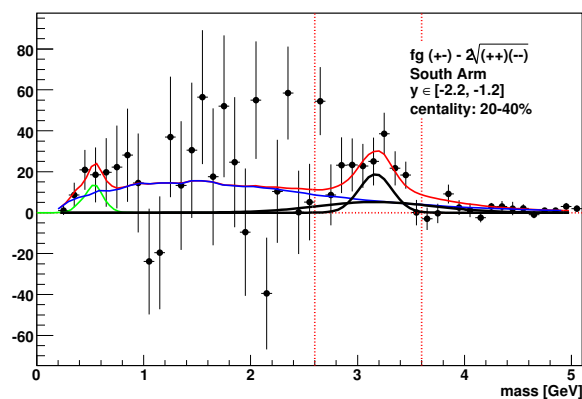
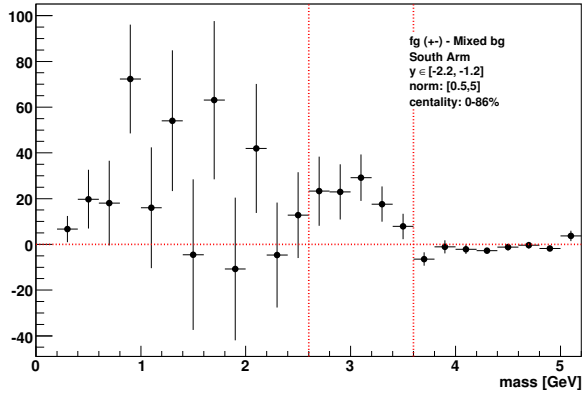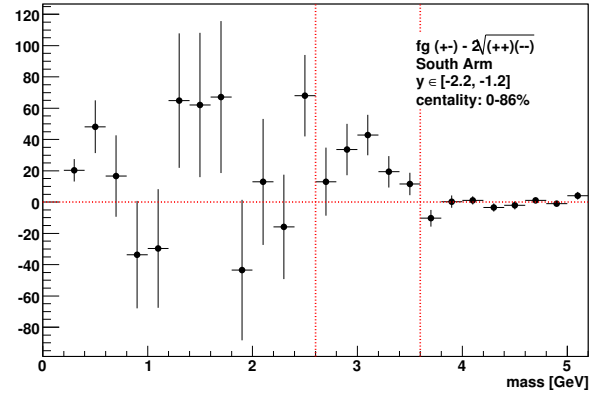**Mixed Subtraction**   **LikeSign Subtraction**

Figure C.15: 62.4 GeV dimuon spectrum in south arm for pT integrated centrality [20-40].
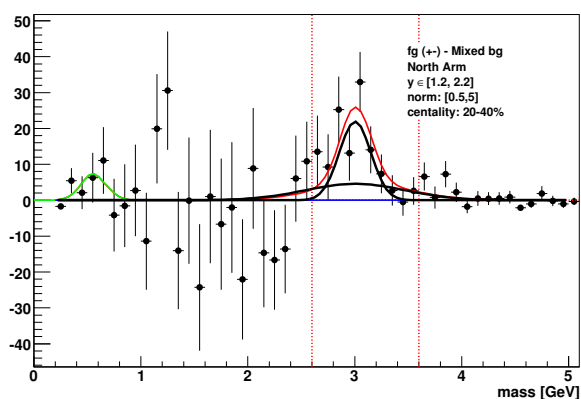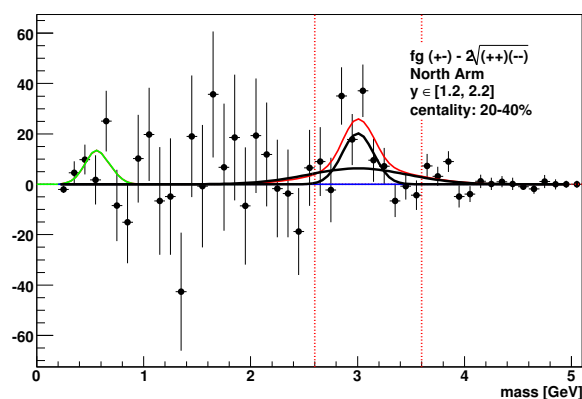
Mixed Subtraction   **LikeSign Subtraction**

Figure C.16: 62.4 GeV dimuon spectrum in north arm for pT integrated centrality [20-40].
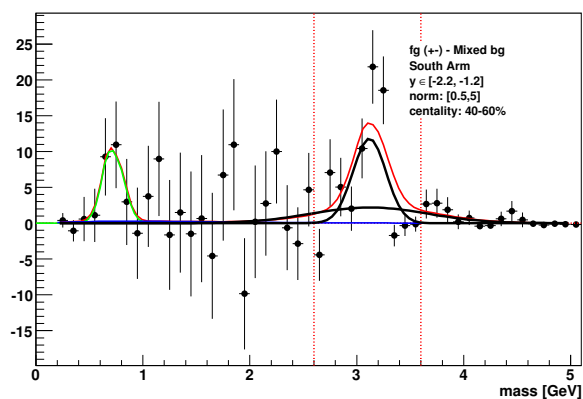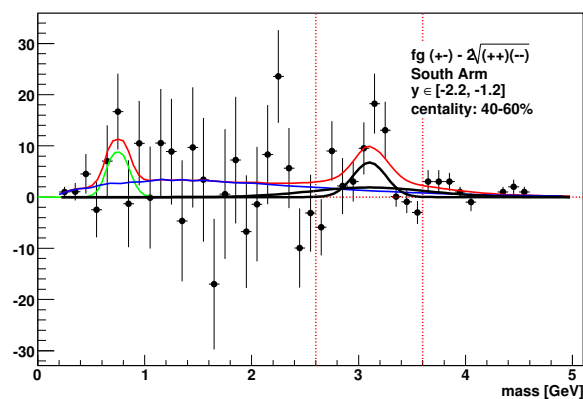
Mixed Subtraction   **LikeSign Subtraction**

Figure C.17: 62.4 GeV dimuon spectrum in south arm for pT integrated centrality [40-60].
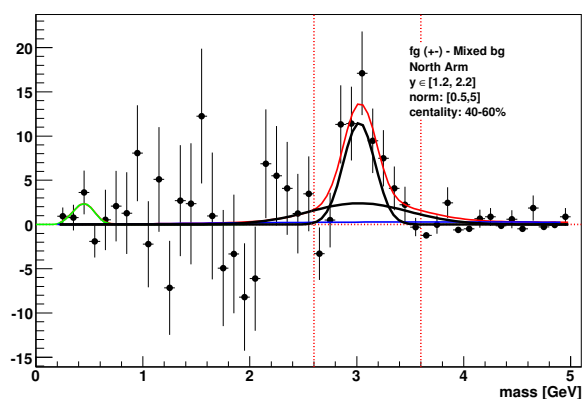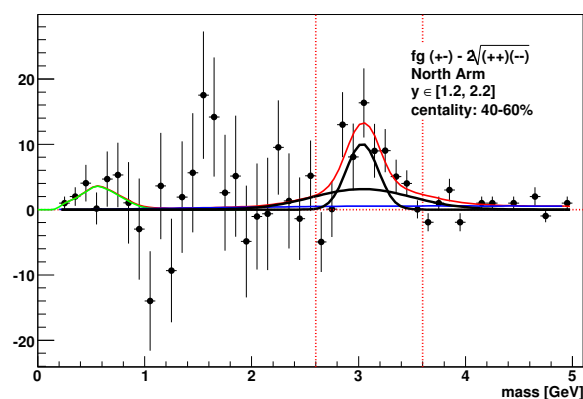
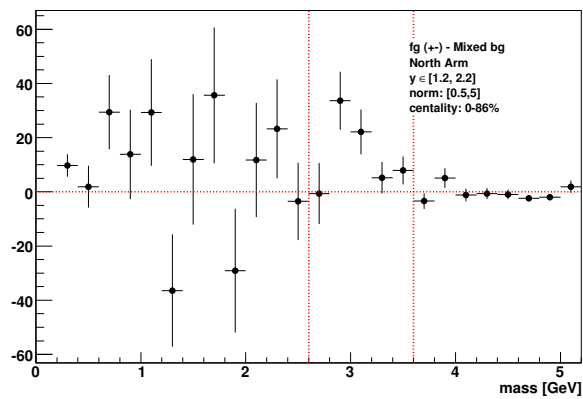**Mixed Subtraction**   **LikeSign Subtraction**

Figure C.18: 62.4 GeV dimuon spectrum in north arm for pT integrated centrality [40-60].
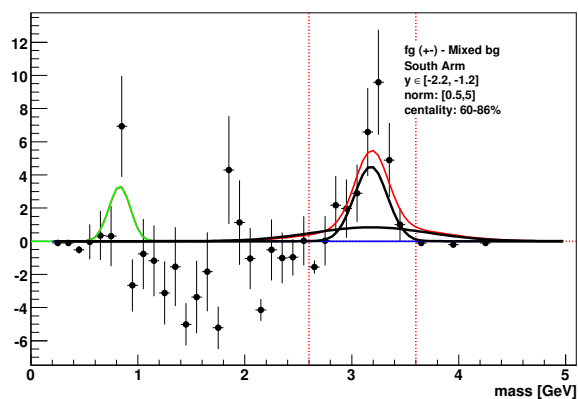
Mixed Subtraction   **LikeSign Subtraction**

Figure C.19: 62.4 GeV dimuon spectrum in south arm for pT integrated centrality [60-100].

Mixed Subtraction   **LikeSign Subtraction**

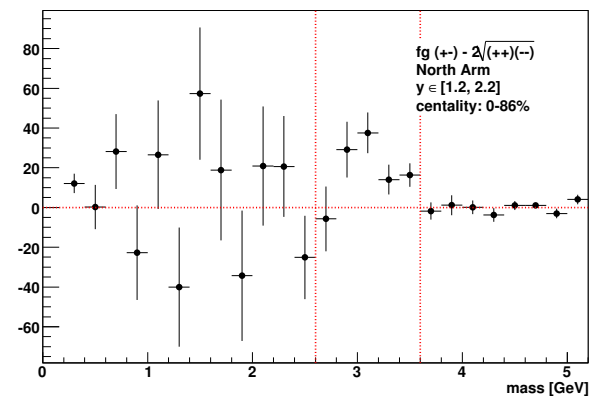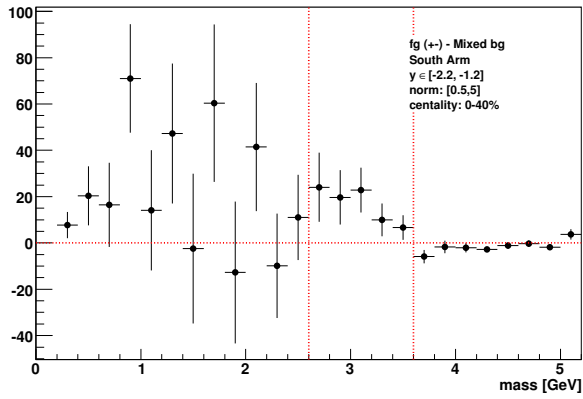Figure C.20: 62.4 GeV dimuon spectrum in north arm for pT integrated centrality [60-100].

Mixed Subtraction

LikeSign Subtraction

Figure C.21: Dimuon spectrum in south arm for p_T integrated centrality $[0, 86]$ (39 GeV).
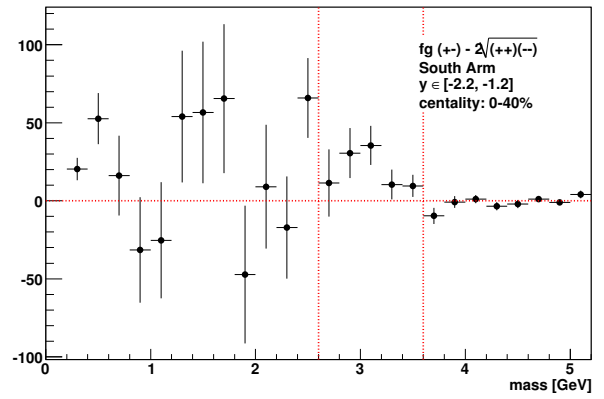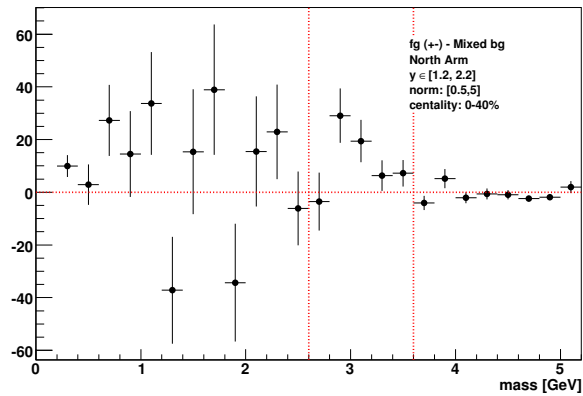

Mixed Subtraction

LikeSign Subtraction

Figure C.22: 39 GeV dimuon spectrum in north arm for p_T integrated centrality $[0, 86]$.
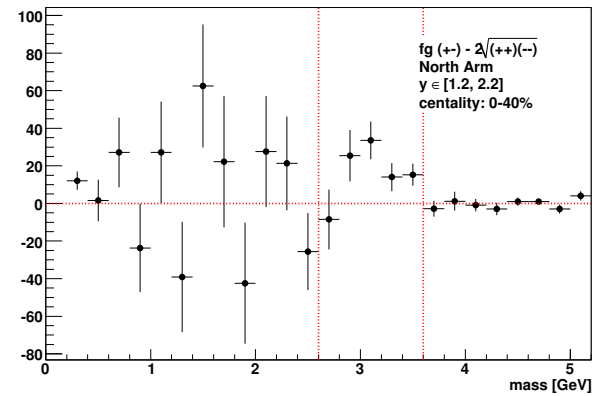
Mixed Subtraction **LikeSign Subtraction**

Figure C.23: 39 GeV dimuon spectrum in south arm for p_T integrated centrality $[0, 40]$.

Mixed Subtraction **LikeSign Subtraction**

Figure C.24: 39 GeV dimuon spectrum in north arm for p_T integrated centrality $[0, 40]$.

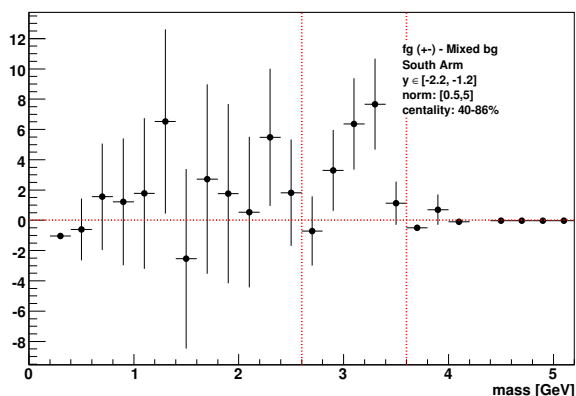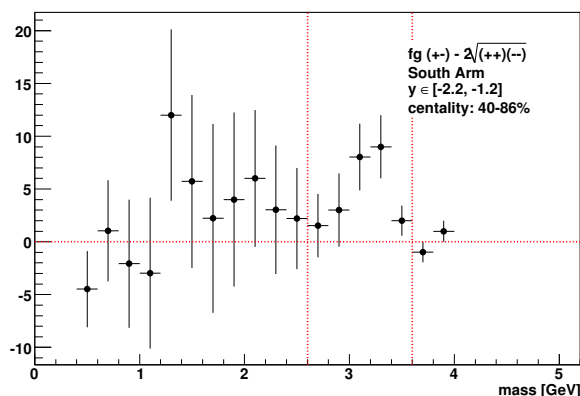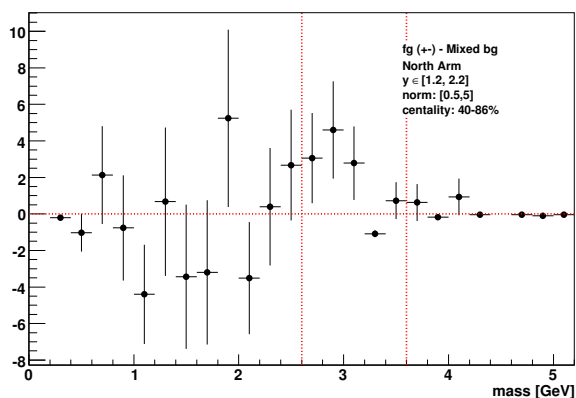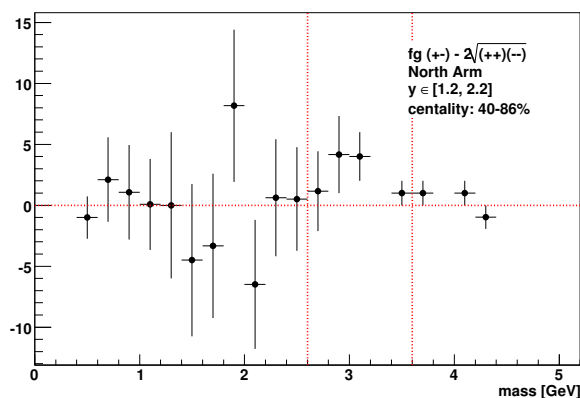**Mixed Subtraction**

LikeSign Subtraction

Figure C.25: 39 GeV dimuon spectrum in south arm for p_T integrated for centrality [40, 86]

.

Mixed Subtraction

LikeSign Subtraction

Figure C.26: 39 GeV dimuon spectrum in north arm for p_T integrated for centrality [40, 86]

.

BIBLIOGRAPHY

[1] BNL, BNL:73847:2005 Formal Report (2005), .

[2] J.-e. Alam, arXiv:1203.3067 (2012), .

[3] K. Nakamura et al. (Particle Data Group), J. Phys. G **37**, 075021 (2010), .

[4] S. Bethke, Prog.Part.Nucl.Phys. **58**, 351 (2007), .

[5] D. J. Gross and F. Wilczek, Phys. Rev. Lett. **30**, 1343 (1973), .

[6] H. D. Politzer, Phys. Rev. Lett. **30**, 1346 (1973).

[7] K. G. Wilson, Phys.Rev. **D10**, 2445 (1974).

[8] H. Satz, Nucl.Phys. **A418**, 447C (1984).

[9] F. Karsch, Lect. Notes Phys. **583**, 209 (2002), .

[10] J. Khoury et al., Phys.Rev. **D64**, 123522 (2001), .

[11] D. Fixsen, Astrophys.J. **707**, 916 (2009), .

[12] K. Brazier and S. Johnston, astro-ph/9803176 (1998), .

[13] T. Matsui and H. Satz, Phys. Lett. B **178**, 416 (1986).

[14] J. Paterson, M. Perl, B. Richter, and P. Rapidis, Phys. Rev. Lett. **33**, 1406 (1974).

[15] J. J. Aubert et al., Phys. Rev. Lett. **33**, 1404 (1974).

[16] K. Hagiwara et al. (Particle Data Group), Phys.Rev. **D66**, 010001 (2002).

[17] E. Norrbin and T. Sjostrand, Eur.Phys.J. **C17**, 137 (2000), .

[18] M. Butenschoen and B. A. Kniehl, AIP Conf.Proc. **1343**, 409 (2011), .

[19] F. Abe et al. (CDF Collaboration), Phys. Rev. Lett. **79**, 573 (1997), .

[20] F. Abe et al. (CDF Collaboration), Phys. Rev. Lett. **79**, 578 (1997), .

[21] J. Lansberg, Phys.Lett. **B695**, 149 (2011), .

[22] J. F. Amundson et al., Phys. Lett. B **372**, 127 (1996), , .

[23] F. Halzen, Phys. Lett. B **69**, 105 (1977), .

[24] T. Alexopoulos et al. (E771 Collaboration), Phys.Lett. **B374**, 271 (1996).

[25] P. Faccioli, C. Lourenco, J. Seixas, and H. Woehri, JHEP **0810**, 004 (2008), .

[26] A. Adare et al. (PHENIX Collaboration), Phys. Rev. D **85**, 092004 (2012), .

[27] A. Adare et al. (PHENIX Collaboration), Phys. Rev. Lett. **98**, 232002 (2007), .

[28] D. Kharzeev, C. Lourenco, M. Nardi, and H. Satz, Z.Phys. **C74**, 307 (1997), .

[29] J. Aubert et al. (European Muon Collaboration), Nucl.Phys. **B293**, 740 (1987).

[30] K. J. Eskola, H. Paukkunen, and C. A. Salgado, JHEP **04**, 065 (2009).

[31] K. J. Eskola, arXiv:1209.1546 (2012), .

[32] B. Alessandro et al. (NA50 Collaboration), Eur. Phys. J. C **33**, 31 (2004), .

[33] J. Cronin et al., Phys.Rev. **D11**, 3105 (1975).

[34] M. Wysocki, Journal of Physics G: Nuclear and Particle Physics **31**, S291 (2005), .

[35] Á. Mócsy and P. Petreczky, Phys. Rev. D **77**, 014501 (2008), , .

[36] M. Gazdzicki and M. I. Gorenstein, Phys.Rev.Lett. **83**, 4009 (1999), .

[37] L. Grandchamp, R. Rapp, and G. E. Brown, Phys.Rev.Lett. **92**, 212301 (2004), .

[38] E. Bratkovskaya et al., Phys.Rev. **C69**, 054903 (2004), .

[39] J. Uphoff et al., PoS **BORMIO2011**, 032 (2011), .

[40] A. Adare et al. (PHENIX Collaboration), Phys.Rev.Lett. **97**, 252002 (2006), .

[41] A. Adare et al. (PHENIX Collaboration), Phys.Rev.Lett. **98**, 172301 (2007), .

[42] N. Armesto et al., Nucl.Phys. **A698**, 583 (2002), .

[43] A. Capella and E. G. Ferreiro, The European Physical Journal C **42**, 419 (2005), .

[44] F. O. Duraes et al., Phys.Rev. **C68**, 035208 (2003), .

[45] C.-Y. Wong, E. Swanson, and T. Barnes, Phys.Rev. **C65**, 014903 (2002), .

[46] J. Nagle, A. Frawley, L. L. Levy, and M. Wysocki (2010), .

[47] B. Alessandro, Alexa, et al., The European Physical Journal C - Particles and Fields **48**, 329 (2006), ISSN 1434-6044, 10.1140/epjc/s10052-006-0079-4, .

[48] M. Abreu et al. (NA50 Collaboration), Phys. Lett. B **477**, 28 (2000).

[49] S. Chatrchyan et al. (CMS Collaboration), JHEP **1205**, 063 (2012), .

[50] C. Suire (ALICE collaboration), arXiv:1208.5601 (2012), .

[51] U. Heinz and M. Jacob, nucl-th/0002042 (2000), .

[52] M. J. Leitch et al. ((FNAL E866/NuSea Collaboration)), Phys. Rev. Lett. **84**, 3256 (2000), .

[53] K. Adcox et al., Nucl. Phys. A **757**, 184 (2005), .

[54] Z. Tang (STAR Collaboration), J. Phys. G **38**, 124107 (2011), .

[55] A. Adare et al. (PHENIX Collaboration), Phys. Rev. C **77**, 024912 (2008), , .

[56] A. Adare et al. (PHENIX Collaboration), Phys. Rev. C **84**, 054912 (2011), .

[57] M. L. Miller et al., Annu. Rev. Nucl. Part. Sci. **57**, 205 (2007), , .

[58] B. Abelev et al. (ALICE Collaboration) (2012), .

[59] S. Aronson et al. (PHENIX Collaboration), Nucl. Inst. and Meth. A **499**, 480 (2003).

[60] M. Allen et al. (PHENIX Collaboration), Nucl. Inst. and Meth. A **499**, 549 (2003), .

[61] K. Adcox et al. (PHENIX Collaboration), Nucl. Inst. and Meth. A **499**, 489 (2003), .

[62] M. Aizawa et al. (PHENIX Collaboration), Nucl. Inst. and Meth. A **499**, 508 (2003), .

[63] L. Aphecetche et al. (PHENIX Collaboration), Nucl. Inst. and Meth. A **499**, 521 (2003).

[64] H. Akikawa et al. (PHENIX Collaboration), Nucl. Inst. and Meth. A **499**, 537 (2003), .

[65] K. Adcox et al. (PHENIX Collaboration), Nucl. Inst. and Meth. A **499**, 469 (2003), .

[66] PHENIX, www.phenix.bnl.gov (2000), .

[67] A. Glenn, Ph.D. thesis, University of Tennessee, Knoxville (2004).

[68] S. Adler et al. (PHENIX Collaboration), Nucl. Inst. and Meth. A **499**, 593 (2003), .

[69] MUTOO, www.phenix.bnl.gov/WWW/muon/software/mutoo/html (2000), .

[70] R. Brun, F. Rademakers, and S. Panacek, pp. 11–42 (2000).

[71] M. Wysocki, private communication (2010), .

[72] R. Brun et al., CERN Program Library Long Write-up W5013 (1994), .

[73] A. Frawley, T. Ullrich, and R. Vogt, Phys. Rep. **462**, 125 (2008).

[74] R. Vogt, private communication (2012).

[75] Schub et al., Phys. Rev. D **52**, 1307 (1995), .

[76] M. S. Kowitt et al., Phys. Rev. Lett. **72**, 1318 (1994), .

[77] D. Antreasyan et al., Phys. Rev. Lett. **48**, 302 (1982).

[78] A. G. Clark et al., Nucl. Phys. B **142**, 29 (1978).

[79] C. Kourkoumelis et al., Physics Letters B **91**, 481 (1980), ISSN 0370-2693.

[80] L. Grandchamp and R. Rapp, Nucl. Phys. A **709**, 415 (2002), .

[81] X. Zhao and R. Rapp, Phys. Rev. C **82**, 064905 (2010), .

[82] X. Zhao and R. Rapp, private communication (2012).

[83] A. Adare et al. (PHENIX Collaboration) (2012), .

[84] X. Gong, private communication (2011), .